12-2012

Pulse Sharpening Effects of Thin Film Ferroelectric Transmission Lines

Robert J. Sleezer
University of Arkansas, Fayetteville

PULSE SHARPENING EFFECTS OF THIN FILM FERROELECTRIC TRANSMISSION LINES

PULSE SHARPENING EFFECTS OF THIN FILM FERROELECTRIC TRANSMISSION LINES

A dissertation submitted in partial fulfillment
of the requirements for the degree of
Doctor of Philosophy in Microelectronics-Photonics

By

Robert J. Sleezer
Oklahoma State University
Bachelor of Science in Computer Science, 2004
Oklahoma State University
Bachelor of Science in Electrical Engineering, 2004
Oklahoma State University
Master of Science in Electrical Engineering, 2006

December 2012
University of Arkansas

ABSTRACT

Advances in material science have resulted in the development of electrically nonlinear high dielectric thin film ferroelectrics, which have led to new opportunities for the creation of novel devices. This dissertation investigated one such device: a low voltage nonlinear transmission line (NLTL). A finite element simulation of ferroelectric transmission lines showed that NLTLs are capable of creating shockwaves. Additionally, if the losses are kept sufficiently low, it was shown that voltage gain should be possible. Furthermore, a method of accounting for material dispersion was developed. Results from simulations including material dispersion showed that temporal solitons might be possible from a continuous ferroelectric based nonlinear transmission line.

Fabrication of a thin film ferroelectric NLTL required the growth of a ferroelectric material on a conductive substrate. Barium titanate (BTO), which has been gaining popularity due to its high dielectric constant, strong nonlinearity, and lack of lead, was grown. Molecular beam epitaxy and sol-gel growth were both explored and sol-gel was chosen as the growth method for the final device, in part due to its ability to grow BTO thin films on highly conductive nickel substrates. Samples approximately 330 nm thick were grown by this method. Oxygen vacancies in the as grown BTO films were filled by annealing in low pressure oxygen environments. X-ray diffraction measurements were used to determine an O_2 pressure for oxidation that was slightly less than the pressure at which NiO forms to ensure maximum filling of the vacancies in the BTO. Grown samples were successfully shown to have ferroelectric properties.

A lumped element transmission line was fabricated using discrete capacitors and inductors with a sample as described above. Test capacitors were fabricated and used to determine the dielectric constant of the BTO thin film. This was used to select capacitor pad sizes and inductor values to create a 50 Ohm line. The substrate was mounted to a chip carrier which was subsequently soldered to a printed circuit board with the appropriate inductors. The device was characterized electrically and the results were compared to the simulation results.

This dissertation is approved for recommendation
to the Graduate Council.

Dissertation Director:

_____
Dr. Gregory J. Salamo

Dissertation Committee:

_____
Dr. Laurent Bellaiche

_____
Dr. Jerzy Krasinski

_____
Dr. Jacques Chakhalian

_____
Professor Ken Vickers (*ex officio*)

The following signatories attest that all software used in this thesis was legally licensed for use by Mr. Robert J. Sleezer for research purposes and publication.

_____ _____
Mr. Robert J. Sleezer, Student Dr. Gregory J. Salamo, Dissertation Director

This thesis was submitted to http://www.turnitin.com for plagiarism review by the TurnItIn company's software. The signatories have examined the report on this thesis that was returned by TurnItIn and attest that, in their opinion, the items highlighted by the software are incidental to common usage and are not plagiarized material.

_____ _____
Professor Ken Vickers, Program Director Dr. Gregory J. Salamo, Dissertation Director

DISSERTATION DUPLICATION RELEASE

I hereby authorize the University of Arkansas Libraries to duplicate this dissertation when needed for research and/or scholarship.

Agreed _____
Robert J. Sleezer

Refused _____
Robert J. Sleezer

ACKNOWLEDGEMENTS

From my family and friends to my professors and mentors many people have helped me during my time at the University of Arkansas. Many of them will never know the true magnitude of the impact that they have had on my life. Although each of them deserves far more than a few lines in this document, for now this small tribute will have to suffice.

First and foremost, I would like to thank my wife Sandra Sleezer. She is amazingly supportive of my dreams and has tirelessly helped me pursue my passions. She has stood by me through late nights and frustrating results sometimes putting her wants aside to assure I had every opportunity to succeed in my endeavors.

Next, I would like to thank my parents, Jim and Cathy Sleezer, who put me on a life long journey of learning. As I grew up they made sure that I got what I needed, even when it was difficult, to keep me on a path that would be rewarding my whole life. My brother, Drew Sleezer, has always had a way of quickly evaluating options and selecting an optimal path that I have worked to emulate. Additionally, although they are not technically family Deane and Fred Gradous should be included here as well. They were often there to provide me with the appropriate support at the appropriate time. For example, it was Fred that put me on path to engineering and Deane has always been willing to help me improve my writing and communication. I should also specifically mention Aunt Christine Sloboth who along with father Jim Sleezer spent several hours helping me collect data.

Next, I must thank the all the support staff that have helped me with all the problems I have presented them. Richard Penhallegon in the electronics shop has been tremendously helpful with all the projects I have needed to do as a part of this research. Brandon Rogers in the

machine shop has done an amazing job of producing many of parts I needed to accomplish various tasks. Even though my project did not involve much MBE, David Monk has always been willing to lend a hand to advance my project. Renee Hearon should also be included in this list for staying on top of all the paperwork details and making sure that I, as well as all the other students, got things submitted to the uEP program, the graduate school, and the University of Arkansas on time.

This list would not be complete unless I mentioned the countless teachers, instructors, and professors who saw potential in me and worked to encourage me even when I resisted. Some of the most important have been Mr. Allen, Dr. Bowen, Mr. Hesler, Dr. Katz, Dr. Mayfield, and Dr. Teague. I wish I could dedicate an entire volume to lauding the impact all of the educators in my life have had. I hope they all know how much they have influenced me. Also the other students I have worked with have been equally important. Without each other many of us would never make it through graduate school. Although there are many students I have interacted with three the three that have had the most impact are David Fritz, Tim Morgan, and Ryan Rollings.

There are two professors I would like to single out in addition to those mentioned above. The first is Jerzy Krasinski who saw me through my masters. I have truly enjoyed working with him and have been very pleased that I was able to continue working with him after coming to the University of Arkansas. Last but not least, I must thank Greg Salamo who has inspired, educated and coached me as I pursued my Ph.D. Working with him I have learned much more than physics and engineering. As I move through my future career one of my goals is to conduct myself as a scientist, an engineer, and a person in such a way as to make Dr. Krasinski and Dr. Salamo proud to call me one of their students.

No list of acknowledgements would be complete without thanking the funding agencies that have made the research I have done possible. Therefore, I would also like to thank both the Department of Defense: Army Research Laboratory and the National Science Foundation for the funding they have provided. This program is financially supported by the National Science Foundation under Grant Numbers EEC-0438704, EEC-1138248 and DMR-0520552 and the Department of Defense: Army Research Laboratory W911ND-08-2-0006. Any opinions, findings, and conclusions or recommendations expressed in this material are those of the author and do not necessarily reflect the views of the National Science Foundation or the Department of Defense: Army Research Laboratory.

If I have inadvertently left anybody out please know that your contribution to my success is no less substantial. I hope to honor all those who have helped me by paying forward all the help, support, and kindnesses that I have experienced while working on my degree.

TABLE OF CONTENTS

1. Introduction

Previously, nonlinear transmission lines have been fabricated using several techniques. One type of nonlinear transmission is a linear transmission line loaded with varactors, which are reverse biased diodes [1, 2], or alternatively varactors connected to inductors [3]. Such lines suffer from relatively complicated fabrication and also require discrete components which will ultimately limit the line performance. Another type of line utilizes inductors that vary with magnetic field [4]. Again, such lines exhibit performance limitations and are also relatively large due to the use of discrete components. Another line which uses ferroelectric capacitors [5] suffer the same draw back and also requires tens of kilovolts to operate. Lines which are continuous but use bulk ferroelectric material [6] sharpens pulses but also requires tens of kilovolts to operate. Relying on discrete components or bulk material causes these lines to be larger than is compatible with current electronic technology.

Recent advances in material science have put much focus on the development and exploration thin films. Such films often have interesting properties that can be exploited to create novel devices. This dissertation presents a ferroelectric thin film based nonlinear transmission line. Transmission line theory and modeling, material properties and growth, and device construction and testing each receive a dedicated chapter. The remainder of this introduction serves to briefly outline each chapter.

Chapter two begins by defining what is meant by nonlinearity and exploring how it has impacted several other fields. Then, potential applications of nonlinear transmission lines are discussed. Next, a lumped element model of a transmission line is developed from Maxwell's equations. The lumped element model is shown to be described by the Korteweg-de Vries

equation. Then an algorithm is developed for simulating the lumped element transmission line model. Several results of simulation are presented in order to explore the effect of various parameters on the behavior of the transmission line. The parameters explored include propagation distance, maximum voltage, loss tangent, and dispersion. Based on the theory presented in this chapter it is expected that a ferroelectric thin film transmission line should be capable of sharpening rising edges, creating voltage gain, and potentially producing a soliton.

Chapter three discusses barium titanate (BTO), the ferroelectric material used for the research presented in this dissertation, starting with the crystal structure and electrical properties. Next, the growth of BTO is discussed. After several thin film growth methods are discussed the analytic techniques used to study the grown material are outlined. Finally, the results of growth by molecular beam epitaxy and sol-gel, both of which were used during the research are presented.

The fourth chapter covers the development and testing of a ferroelectric thin film transmission line. It begins by explaining why a lumped element transmission line was fabricated in lieu of the original plan to fabricate a continuous monolithic transmission line. Next, specific design concerns including the printed circuit board layout and component selection are discussed. Once the design has been covered, the actual fabrication details are provided. Finally, the results of testing the transmission line are presented and compared to simulation results. A final chapter provides a conclusion for the dissertation.

2. Nonlinear Transmission Line Theory

2.1 Introduction

This chapter introduces the theory of nonlinear transmission lines (NLTL). Before exploring the implications of nonlinear propagation a definition must be established. Next, a brief overview of three areas of nonlinear propagation: acoustics, hydrodynamics, and optics, provides a broader perspective than just nonlinear electronics. A few potential application of electrical NLTLs precedes an in depth discussion of theory. This discussion begins by developing a finite element circuit model from Maxwell's equations. Once the model has been developed, a second order nonlinear differential equation defining the transmission line behavior is derived. Next, this equation is shown to have a soliton solution by way of the Korteweg-de Vries equation. The discussion then moves on to the finite element simulation and brief tutorial on the algorithm and interpretation of results is presented. Finally, the results of several simulations which explore the behavior of a pulse propagating along lines with various parameters are presented.

2.1.1 Mathematical Definition of Nonlinearity

A TL is defined as nonlinear if summing two signals after propagation is not equivalent to summing two signals and propagating the result. Additionally, a TL is nonlinear if scaling the amplitude of a wave before propagation is not equivalent to scaling a wave after propagation. In other words, the rate of propagation depends on the amplitude of the signal. This is mathematically shown in Equation 1 where a is a scalar, $F(t)$ is a time domain waveform, and the function $\mathcal{T}$ represents the process of transmission along an NLTL [7].

$$\mathcal{T}\big(aF(t)\big) \neq a\mathcal{T}\big(F(t)\big) \tag{1}$$

2.1.2 Implications of NL

Nonlinearity is often viewed as a negative property in electronics. Operational amplifiers and filters are examples of devices where linearity is highly desired. There are some devices, however, where nonlinearity is exploited. Such devices include voltage regulators, digital electronics, and diodes. Nonlinear elements may introduce distortion into a signal because they are not closed under addition or scalar multiplication. On the other hand, three potential benefits from the use of a nonlinear dielectric in a transmission line are shock waves, solitons, and voltage gain which result are examined in later sections.

2.1.3 Historical Discussion

In addition to electrically nonlinear transmission lines examples of fields that include the study of nonlinear propagation include acoustics, hydrodynamics, and optics. This section briefly introduces each area and provides an example or two from each field.

2.1.3.1 Nonlinear Acoustics

The history of nonlinear acoustics started with Euler who was the first to publish a nonlinear differential equation for the propagation of sound. Later Poisson derived a solution for this equation without recognizing the importance of the nonlinearity because he perceived that a pulse of sound would not change in length [8]. It took Stokes to realize that while the duration of the pulse remained the same, because the rising foot and the falling foot both travel with the same small signal velocity, different parts of the pulse could still propagate with different velocities. Stokes went on to describe the deformation of waves based on the nonlinearity based on Poisson's work. Reproductions of Stokes' sketches are shown in Figure 1 [8]. From this

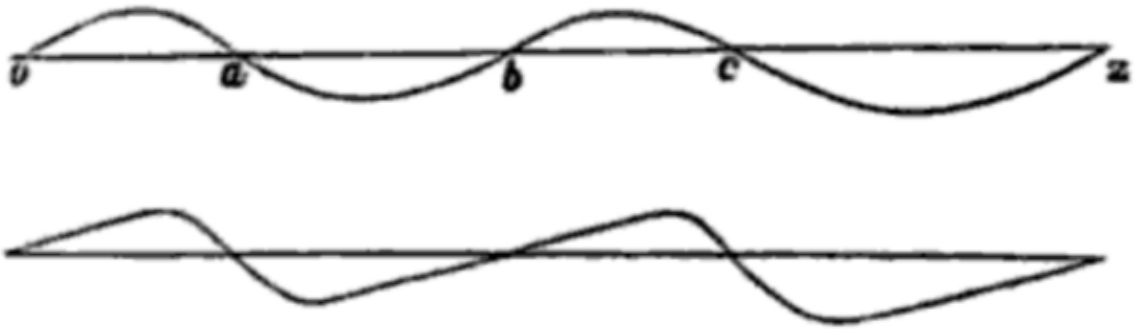

Figure 1: Sketches showing the deformation of a waveform caused by nonlinear propagation [8]

beginning, nonlinear acoustics have found applications in many areas including material characterization [9], microscopy [10], and biomedical imaging [11].

2.1.3.2 Nonlinear Effects in Water Waves

Waves on a beach behave in a nonlinear manner as they move up the shoal and the troughs experience more drag than the peaks. This drag causes an increase in amplitude as the peak consumes the water in front of it. If there is a sufficient change in amplitude the crest will move over empty space and the wave will crash. Despite the long history of crashing waves, a modeling of this nonlinear effect first occurred in the 1940s [12] with interest continuing through at least the first decade of this century [13-15]. If the beach becomes a shallow canal of the proper dimensions an interesting effect occurs: the soliton. The well-known story of Scott Russell's discovery and study of the soliton can be found in many references (as examples see [16-20]). By extending the canal to the ocean, solitons can be found in the form of tsunamis with wavelengths of tens or hundreds of kilometers. Since the ocean is only, at its deepest point 10,938 meters [21], relative to a tsunami wavelegth the ocean is a shallow body of water. For example, the 26 December 2004 Sumatra tsunami had a satellite measured wavelength of 580

kilometers [22]. Theoretical efforts have shown that these powerful waves can be modeled by the Korteweg-de Vries equation which has a hyperbolic secant squared as soliton solution [23].

2.1.3.3 Nonlinear optical pulse propagation

In optics the polarization, $\tilde{P}(t)$, of a material resulting from an applied optical field, $\tilde{E}(t)$, can be written as a power series as shown in Equation 2 where $\chi^{(1)}$ is the linear susceptibility, $\chi^{(2)}$ is the second order nonlinear susceptibility, $\chi^{(3)}$ is the third order nonlinear susceptibility, and so on [24].

$$\tilde{P}(t) = \chi^{(1)}\tilde{E}(t) + \chi^{(2)}\tilde{E}^2(t) + \chi^{(3)}\tilde{E}^3(t) + \cdots \quad (2)$$

The field of nonlinear optics is rather large and a full treatment of the subject is beyond the intended scope of this section. Rather, two examples of nonlinear propagation which are closely related to the rest of the work in this document are presented. The first example is a self-focusing pulse while the second is a temporal soliton. Light induced lensing, which can occur because the refractive index in a material depends on the susceptibility, can under the appropriate conditions trap a beam of light. This happens when a beam propagating through a nonlinear material induces a higher refractive index at its center than at its margins thus effectively creating its own waveguide [25, 26]. The second example the evolution of an optical pulse train into a Jacobi elliptic soliton pulse-train [27]. In this work the dispersion, resulting from different frequency components propagate at different velocities, was balanced by the nonlinearity, where different intensities propagate at different velocities, such that the energy in the pulses are rearranged until they take the stable unchanging analytic form of he Jacobi elliptic function. Much work has been done to exploit the properties of solitons in communication networks (see [28-30] as examples).

2.2 Potential Applications of NLTLs

Potential applications for nonlinear transmission lines include harmonic generation, solitons, voltage amplification, and tunable delay lines. Each of these areas is briefly discussed in this section.

2.2.1 Harmonic Generation

As a pulse or waveform deforms as it propagates along a NLTL, the Fourier components of that electrical signal will change. In many cases this is a negative effect which must be mitigated because they cause problems in power distribution networks, communication systems, and measurement devices and much work has been done to reduce the harmonics or their effects (see as examples [31-35]). In other cases, however, harmonics are used as a way to generate higher frequency or even THz signals [36], quasi-optical power sources [37], and radio frequency communication [38].

2.2.2 Solitons for Communication

Current electrical communications, unlike optical communications, are dispersion limited. The reason is that nonlinear optical fibers capable of propagating solitons exist while no such practical electronic line exists. If electrical lines with the same feature were developed they would not only offer the many of the same benefits as the optical fibers but would also be capable of being incorporated into integrated circuits [39].

2.2.3 Switching Amplifier

A traditional switching power supply uses an inductor with rapid switching to achieve voltage gain [40]. Since ferroelectric NLTLs have the potential for voltage gain [41] it might be possible to replace the inductor in the power supply with an NLTL. This might reduce the size,

increase the efficiency, and improve the reliability of switching power supplies because they could be made monolithically.

2.3 Theory

This section provides the theoretical background for the rest of the document by establishing some important proofs and presenting simulation results. It will begin with the geometry of the device and Maxwell's equations before developing a circuit model. Next, the differential equation that describes the behavior of the circuit model is derived. Finally, Korteweg – de Vries equation is also shown to describe the transmission line behavior under specific circumstances.

2.3.1 NLTL Principles

The following derivations refer to Figure 2 where the metal is yellow and the dielectric is blue. The metal in Figure 2 is presumed to be so highly conductive that any thickness will have negligible losses. The insets show how a pulse might look as a function of time at the beginning,

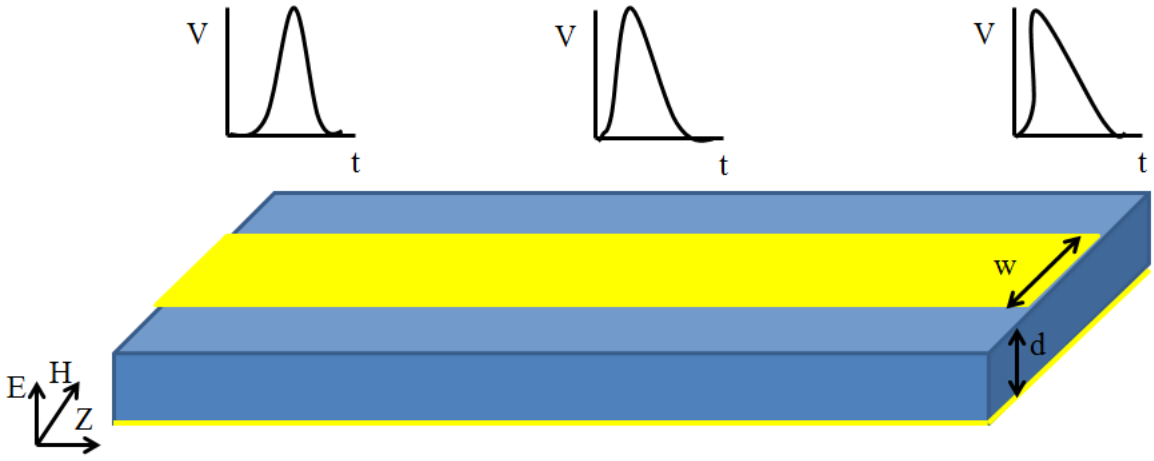

Figure 2: Diagram of NLTL

the middle, and the end of the line.

2.3.1.1 Maxwell's Equations to Circuits

Here a basic lossless model based on inductors and capacitors is developed starting from Maxwell's equations. Simulations based on this model, with losses included, are presented below.

$$\nabla \times \bar{E}(\vec{r},t) = -\frac{\partial \bar{B}}{\partial t} \tag{3}$$

$$\nabla \times \bar{H}(\vec{r},t) = J_f + \frac{\partial \bar{D}}{\partial t} \tag{4}$$

Since there is no free current, with a little substitution the above equations become

$$\nabla \times \bar{E}(\vec{r},t) = -\frac{\partial}{\partial t}\,\mu \bar{H}(\vec{r},t) \tag{5}$$

$$\nabla \times \bar{H}(\vec{r},t) = \frac{\partial}{\partial t}\epsilon(\bar{E})\bar{E}(\vec{r},t). \tag{6}$$

Next, the curls are reduced to partial derivatives by using the fact that magnetic field and electric field are in the x and y directions. If $\bar{H} = g(z,t)\hat{x}$ and $\bar{E} = f(z,t)\hat{y}$ then

$$\frac{\partial f(z,t)}{\partial z}\hat{x} = -\frac{\partial}{\partial t}\mu g(z,t)\hat{x} \tag{7}$$

$$\frac{\partial g(z,t)}{\partial z}\hat{y} = \frac{\partial}{\partial t}\epsilon f(z,t)\hat{y}. \tag{8}$$

Voltage is introduced by integrating the electric field while current is introduced by integrating the magnetic field, which is Ampere's law in integral form where the closed loop is around a z cut of the top conductor. Using the dimensions from Figure 2

$$V(z,t) = \int_0^d \bar{E}(\vec{r},t)\, dy = df(z,t) \tag{9}$$

$$I(z,t) = \iint_S \bar{J}_f \cdot d\bar{S} = \oint_C \bar{H}(\hat{r},t) \cdot d\bar{l} = -wg(z,t). \tag{10}$$

Therefore, Equations 7 and 8 become

$$\frac{\partial V(z,t)}{\partial z}\hat{x} = -\frac{\partial}{\partial t}\frac{\mu d}{w} I(z,t)\hat{x} \tag{11}$$

$$\frac{\partial I(z,t)}{\partial z}\hat{y} = \frac{\partial}{\partial t}\frac{\epsilon w}{d} V(z,t)\hat{y}. \tag{12}$$

If fringing is neglected the inductance and capacitance per unit length are given by $L = \frac{\mu d}{w}$ and $C = \frac{\epsilon w}{d}$ respectively. So,

$$\frac{\partial V(z,t)}{\partial z} = -\frac{\partial}{\partial t} LI(z,t) \tag{13}$$

$$\frac{\partial I(z,t)}{\partial z} = \frac{\partial}{\partial t} CV(z,t). \tag{14}$$

Thus, the transmission line can be modeled by a distributed inductance and capacitance with a voltage across the dielectric and a current along the line. When the distributed circuit elements are cut up into finite elements the circuit model in Figure 3 is achieved. Two elements not previously discussed have been included in the model to account for losses. The first, labeled R, represents the resistance of the traces while the second, labeled G, results from the leakage current through the dielectric [42].

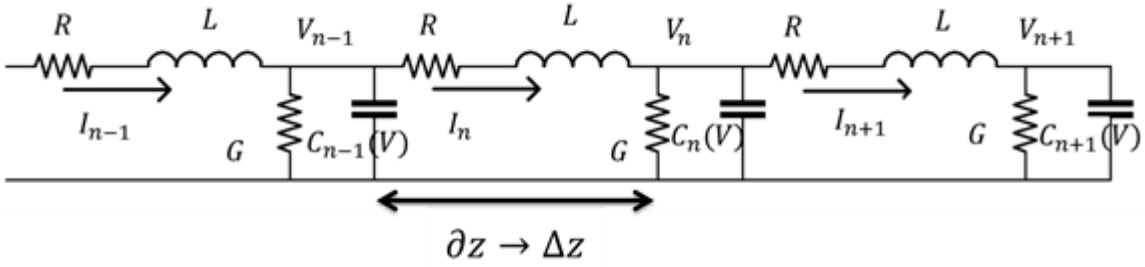

Figure 3: Circuit Model

2.3.1.2 Equations Derived From Circuit Theory

This section derives a second order differential equation from the circuit model derived above. These equations are numerically integrated to get the results shown in the simulation section. The derivation begins with identifying the currents through the voltage dependent capacitor, $C_n(V_n)$, and shunt conductance, L, at node n.

$$I_{C_n} = C_n(V_n)\dot{V}_n \tag{15}$$

$$I_{G_n} = V_n G_n \tag{16}$$

The current through the n^{th} capacitor plus the current through the n^{th} shunt conductance is the difference between the current flowing in the n^{th} inductor and the $n^{th} + 1$ inductor.

$$I_n - I_{n+1} = C_n(V_n)\dot{V}_n + V_n G \tag{17}$$

The first derivative of equation 17 with respect to time, which will be needed later, is arrived at through application of the chain rule.

$$\dot{I}_n - \dot{I}_{n+1} = \left(\frac{d}{dV_n} C_n(V_n)\right)\dot{V}_n^2 + C_n(V_n)\ddot{V}_n + \dot{V}_n G \tag{18}$$

Next, the voltage drop across the inductor and series resistor for both the node n and the node $n + 1$ yield the following.

$$V_{n-1} - V_n - L\dot{I}_n - RI_n = 0 \tag{19}$$

$$V_n - V_{n+1} - L\dot{I}_{n+1} - RI_{n+1} = 0 \tag{20}$$

Equations 19 and 20 are combined to result in

$$V_{n-1} = 2V_n + L\left[\dot{I}_n - \dot{I}_{n+1}\right] + R[I_n - I_{n+1}] - V_{n+1}. \tag{21}$$

Substituting equations 17 and 18 into 21 reduces the number of variables by representing the currents in terms of voltages.

$$V_{n-1} = 2V_n + L\left[\frac{d}{dV_n}\left(C_n(V_n)\right)\dot{V}_n^2 + C_n(V_n)\ddot{V}_n + \dot{V}_n G\right] + R\left[C_n(V_n)\dot{V}_n + V_n G\right] - V_{n+1} \tag{22}$$

Finally, algebra yields the second order differential equation which is numerically integrated in the simulation section below.

$$\ddot{V}_n = \frac{1}{LC_n(V_n)}(V_{n+1} - 2V_n + V_{n-1}) - \frac{RGV_n}{LC_n(V_n)} - \frac{1}{C_n(V_n)}\frac{d}{dV_n}\left(C_n(V_n)\right)\dot{V}_n^2 - \frac{R}{L}\dot{V}_n - \frac{\dot{V}_n G}{C_n(V_n)} \tag{23}$$

In equation 23 the first term is the nonlinear term, the second term is standard linear term for transmission lines, and the last two terms represent the losses. This result is in good agreement with work done on discrete NLTLs [43-45] when resistances are set to zero or infinity where appropriate.

2.3.1.3 Circuit Theory to Korteweg–de Vries

Here, the Korteweg-de Vries (KdV) equation, first used to model water waves in a canal [46], is derived from the nonlinear circuit model which was established above. This derivation, based on the one by Dauxois and Peyrard [18], enables the leveraging of the large body of work developed for the KdV equation (see as examples [18, 47-50]). The overall process of this derivation is shown as a block diagram in Figure XYZ. For this derivation a lossless line, which is achieved by setting $R = 0\Omega$ (short circuit) and $G = 0\text{S}$ (open circuit), will be assumed. Also the dependence of C_n on voltage will be assumed to have the form

$$C_n(V_n) = C_0 - a_1 V_n - a_2 V_n^2 - a_3 V_n^3 - \cdots \tag{24}$$

where $|a_1 V_n| \gg |a_2 V_n^2| \gg |a_2 V_n^3| \gg \cdots$. The charge on the capacitor is obtained by integrating with respect to voltage yielding

$$Q_n = \int_0^{V_n} C_n(V) dV = C(0)\left[V_n - \tfrac{a_1}{2} V_n^2\right]. \tag{25}$$

Since one unknown constant is as good as another a will be used in place of $a_1/2$. Substitution of $\dot{Q} = I$ and $\dot{Q}_n = I_n - I_{n+1}$ into equation 21 results in

$$\ddot{Q}_n = C(0)\left[\ddot{V}_n - a\ddot{V}_n^2\right] = \tfrac{1}{L}[V_{n+1} - 2V_n + V_{n-1}]. \tag{26}$$

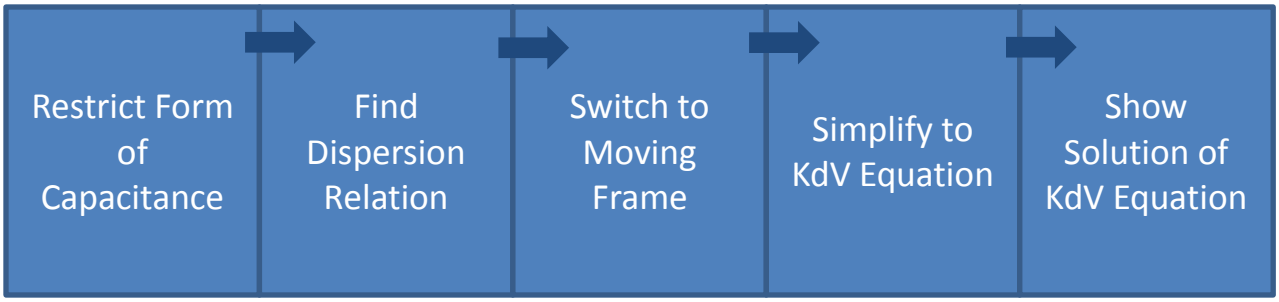

Figure 4: Block Diagram of KdV Derivation

Note that the linear version of equation 26 has plane wave solutions with the dispersion relation

$$\omega = \pm \frac{2}{\sqrt{LC}} \sin \frac{q}{2}, \tag{27}$$

where ω is the angular frequency and q is the wave number. Next the voltages of the continuous transmission line $V(z = n \pm 1) = V_{n\pm1}$ are expressed as the Taylor series centered around n.

$$V_{n\pm1} = V_n \pm \frac{\partial}{\partial z} V_n + \frac{1}{2}\frac{\partial^2}{\partial z^2} V_n \pm \frac{1}{6}\frac{\partial^3}{\partial z^3} V_n + \frac{1}{24}\frac{\partial^4}{\partial z^4} V_n \pm \cdots \tag{28}$$

Equation 26, with the substitution of the Taylor series to 4th order, now becomes

$$\ddot{V}_n - a\ddot{V}_n^2 = \frac{1}{LC(0)}\left[\frac{\partial^2}{\partial z^2} V_n + \frac{1}{12}\frac{\partial^4}{\partial z^4} V_n\right]. \tag{29}$$

The Taylor series was truncated at 4th order because at this order the dispersion relation

$$\omega = \frac{1}{\sqrt{LC}}\left(q - \frac{q^3}{24}\right) \tag{30}$$

is equivalent to equation 27 for long wavelengths. In other words, as long as our x dimension has sufficient resolution equation 29 is a good model for the transmission line. Next, a substitution is made to introduce a small parameter ε such that $V_n = \varepsilon U$. Although this introduces some complexity now, it will provide later provide a parameter that will be used to balance the nonlinearity with the dispersion. Thus, equation 29, with some rearrangement, becomes

$$0 = \frac{\partial^2}{\partial t^2}(\varepsilon U - a\varepsilon^2 U^2) - \frac{\varepsilon}{LC(0)}\frac{\partial^2}{\partial z^2} U - \frac{\varepsilon}{12LC(0)}\frac{\partial^4}{\partial z^4} U\,. \tag{31}$$

Now, an effort must be made to simplify this equation. This simplification will be achieved by changing the previously static frame of reference into a frame moving at the velocity

of propagation. First, however, ω from the dispersion relation is substituted into the argument of the plane wave solution resulting in

$$\omega t - qx = \frac{1}{\sqrt{LC(0)}}\left(q - \frac{q^3}{24}\right)t - qx. \tag{32}$$

Next, a new relationship $q \equiv K\varepsilon^{\alpha}$ is defined where α will be used later to balance the nonlinearity and the dispersion. Equation 32 then turns into

$$\omega t - qx = K\varepsilon^{\alpha}\left(\frac{1}{LC(0)}t - x\right) - \frac{K^3\varepsilon^{3\alpha}t}{24}. \tag{33}$$

In order to massage the right hand side into a form similar to the left hand side three new variables ξ, τ, and Ω are defined. The moving reference from is introduced through ξ while τ and Ω will simply clean up the form of the equation.

$$\xi = \varepsilon^{\alpha}\left(x - \frac{t}{\sqrt{LC(0)}}\right) \tag{34}$$

$$\tau = \varepsilon^{3\alpha}t \tag{35}$$

$$\Omega = \frac{K^3}{24} \tag{36}$$

Plugging these into equation 33 results in

$$\omega t - qx = \Omega\tau - K\xi. \tag{37}$$

To write equation 31 in terms of the new variables U, which is a function of x and t is set equal to W which is a function of ξ and τ; appropriate derivatives are found using the chain rule; and substitutions are made. The initial definition of W and the derivatives are shown in equations 38 through 44.

$$U(x,t) \equiv W(\xi,\tau) = W\left(\varepsilon^{\alpha}\left(x - \frac{t}{\sqrt{LC(0)}}\right), \varepsilon^{3\alpha}t\right) \tag{38}$$

$$\frac{\partial U}{\partial x} = \frac{\partial W}{\partial \xi}\varepsilon^{\alpha} \tag{39}$$

$$\frac{\partial^2 U}{\partial x^2} = \frac{\partial^2 W}{\partial \xi^2}\varepsilon^{2\alpha} \tag{40}$$

$$\frac{\partial^3 U}{dx^3} = \frac{\partial^3 W}{\partial \xi^3}\varepsilon^{3\alpha} \tag{41}$$

$$\frac{\partial^4 U}{\partial x^4} = \frac{\partial^4 W}{\partial \xi^4}\varepsilon^{4\alpha} \tag{42}$$

$$\frac{\partial U}{\partial t} = -\frac{\partial W}{\partial \xi}\frac{1}{\sqrt{LC(0)}}\varepsilon^{\alpha} + \frac{\partial W}{\partial \tau}\varepsilon^{3\alpha} \tag{43}$$

$$\frac{\partial^2 U}{\partial t^2} = \frac{\partial^2 W}{\partial \xi^2}\frac{1}{LC(0)}\ \varepsilon^{2\alpha} - \frac{\partial^2 W}{\partial \xi \partial \tau}\frac{2}{\sqrt{LC(0)}}\varepsilon^{4\alpha} + \frac{\partial^2 W}{\partial \tau^2}\varepsilon^{6\alpha} \tag{44}$$

When these derivatives are substituted in equation 31, with some algebra equation 45 is achieved.

$$0 = \left(\frac{\varepsilon^{2\alpha}}{LC(0)}\frac{\partial^2}{\partial \xi^2} - \frac{2\varepsilon^{4\alpha}}{\sqrt{LC(0)}}\frac{\partial^2}{\partial \xi \partial \tau} + \varepsilon^{6\alpha}\frac{\partial^2}{\partial \tau^2}\right)(W - \varepsilon a W^2) - \frac{\varepsilon^{2\alpha}}{LC(0)}\frac{\partial^2 W}{\partial \xi^2} - \frac{\varepsilon^{4\alpha}}{12LC(0)}\frac{\partial^4 W}{\partial \xi^4} \tag{45}$$

Now, recalling that $U \equiv W$ we arrive at equation 46.

$$0 = \left(\frac{\varepsilon^{2\alpha}}{LC(0)}\frac{\partial^2}{\partial \xi^2} - \frac{2\varepsilon^{4\alpha}}{\sqrt{LC(0)}}\frac{\partial^2}{\partial \xi \partial \tau} + \varepsilon^{6\alpha}\frac{\partial^2}{\partial \tau^2}\right)(U - \varepsilon a U^2) - \frac{\varepsilon^{2\alpha}}{LC(0)}\frac{\partial^2 U}{\partial \xi^2} - \frac{\varepsilon^{4\alpha}}{12LC(0)}\frac{\partial^4 U}{\partial \xi^4} \tag{46}$$

At this point, the first term is expanded and the equation is rearranged in terms of the powers of α.

$$0 = -\frac{a\varepsilon^{2\alpha+1}}{LC(0)}\frac{\partial^2 U^2}{\partial \xi^2} - \varepsilon^{4\alpha}\left(\frac{2}{\sqrt{LC(0)}}\frac{\partial^2 U}{\partial \xi \partial \tau} - \frac{1}{12LC(0)}\frac{\partial^4 U}{\partial \xi^4}\right) - \frac{2a\varepsilon^{4\alpha+1}}{\sqrt{LC(0)}}\frac{\partial^2 U^2}{\partial \xi \partial \tau} + \varepsilon^{6\alpha}\frac{\partial^2 U}{\partial \tau^2} + \tag{47}$$

$$a\varepsilon^{6\alpha+1}\frac{\partial^2 U^2}{\partial\tau^2}$$

Since ε was defined to be small we will disregard the higher order terms.

$$0 = -\frac{a\varepsilon^{2\alpha+1}}{LC(0)}\frac{\partial^2 U^2}{\partial\xi^2} - \varepsilon^{4\alpha}\left(\frac{2}{\sqrt{LC(0)}}\frac{\partial^2 U}{\partial\xi\partial\tau} - \frac{1}{12LC(0)}\frac{\partial^4 U}{\partial\xi^4}\right) \tag{48}$$

If α in equation 48 is set to $\frac{1}{2}$, in order to balance the dispersion an the nonlinear terms then

$$0 = \varepsilon^2\left(\frac{a}{LC(0)}\frac{\partial^2 U^2}{\partial\xi^2} + \frac{2}{\sqrt{LC(0)}}\frac{\partial^2 U}{\partial\xi\partial\tau} + \frac{1}{12LC(0)}\frac{\partial^4 U}{\partial\xi^4}\right). \tag{49}$$

With some rearrangement this simplifies to

$$0 = \frac{\varepsilon^2}{\sqrt{LC(0)}}\left(\frac{\partial^2 U}{\partial\xi\partial\tau} + \frac{a}{2\sqrt{LC(0)}}\frac{\partial^2 U^2}{\partial\xi^2} + \frac{1}{12\sqrt{LC(0)}}\frac{\partial^4 U}{\partial\xi^4}\right). \tag{50}$$

Since $\frac{\varepsilon^2}{\sqrt{LC(0)}}$ is nonzero, the term in parenthesis must be zero so we arrive at

$$0 = \frac{\partial^2 U}{\partial\xi\partial\tau} + \frac{a}{2\sqrt{LC(0)}}\frac{\partial^2 U^2}{\partial\xi^2} + \frac{1}{12\sqrt{LC(0)}}\frac{\partial^4 U}{\partial\xi^4}. \tag{51}$$

Next, integrating with respect to ξ results in

$$0 = \frac{\partial U}{\partial\tau} + \frac{aU}{\sqrt{LC(0)}}\frac{\partial U}{\partial\xi} + \frac{1}{24\sqrt{LC(0)}}\frac{\partial^3 U}{\partial\xi^3}. \tag{52}$$

Which, with a little algebra, becomes

$$0 = 24\sqrt{LC(0)}\frac{\partial U}{\partial\tau} + 24aU\frac{\partial U}{\partial\xi} + \frac{\partial^3 U}{\partial\xi^3}. \tag{53}$$

Another change of variable, where $\tau = 24\sqrt{LC(0)}T$ and $\partial\tau = 24\sqrt{LC(0)}\partial T$, gives

$$0 = \frac{\partial U}{\partial T} + 24aU\frac{\partial U}{\partial \xi} + \frac{\partial^3 U}{\partial \xi^3}. \tag{54}$$

Finally, if $\phi \equiv 4aU$, reduces to the KdV equation:

$$0 = \frac{\partial \phi}{\partial T} + 6\phi\frac{\partial \phi}{\partial \xi} + \frac{\partial^3 \phi}{\partial \xi^3}. \tag{55}$$

Equation 55 can be linearized by removing the middle term. This linearized equation has a solution

$$\phi = Ae^{i(q\xi - \omega\tau)} = Ae^{iq\varepsilon^{\frac{1}{2}}\left(x - \frac{t}{\sqrt{LC(0)}}\right) - \omega\varepsilon^{\frac{3}{2}}t} \tag{56}$$

where the dispersion relation is $\omega = q^3$. In order to form a soliton, this dispersion must be balanced by the nonlinearity. When considering only the first two terms, plane waves are not a solution. The solution shown in equation 56 would have the dispersion relation

$$\omega = \frac{q^2 c_0 - 6Aqc_0 t}{\left(\frac{36A^2 q}{\sqrt{LC(0)}}\right)^{\frac{1}{3}} t} \tag{57}$$

which depends not only on the wave vector but also on the amplitude, as expected, and on time. Because plane waves are not a solution to the KdV equation with the linear portion removed, a different direction will be taken. This approach is used by both Taniuti and Nishihara [51] and Dauxois and Peyrard [18]. Begin by considering the simpler linear equation which depends on a parameter v shown below.

$$0 = \frac{\partial \phi}{\partial T} + v\frac{\partial \phi}{\partial \xi} \tag{58}$$

This equation has a solution $\phi = Ae^{i(q\xi - v\omega T)}$ where there is no dispersion. In other words, a solution to equation 58 is a plane wave moving, with phase velocity v in the ξ direction. The

important result is that the coefficient v controls the phase velocity so that if v becomes a function of ϕ then the phase velocity also becomes a function of ϕ. Thus, the effect of the middle term in 55 is to propagate frequencies with higher amplitudes faster. One solution that balances this nonlinear propagation with the dispersion is that of a hyperbolic secant squared, which is shown in equation 59.

$$\phi = A\ \mathrm{sech}^2\left(\sqrt{\frac{A}{2}}(\xi - 2A\tau)\right) \tag{59}$$

To show that this is indeed a solution to the KdV equation the appropriate derivatives with respect to ξ and τ are needed. These derivatives are shown in equations 60 through 62 where $R = \sqrt{\frac{A}{2}}(\xi - 2A\tau)$.

$$\frac{\partial \phi}{\partial \xi} = -\sqrt{2}A^{\frac{3}{2}}\,\mathrm{sech}^2(R)\tanh(R) \tag{60}$$

$$\frac{\partial^3 \phi}{\partial \xi^3} = A[4\sqrt{2}A^{\frac{3}{2}}\,\mathrm{sech}^4(R)\tanh(R) - 2\sqrt{2}A^{\frac{3}{2}}\,\mathrm{sech}^2(R)\tanh^3(R)] \tag{61}$$

$$\frac{\partial \phi}{\partial \tau} = 2\sqrt{2}A^{\frac{5}{2}}\,\mathrm{sech}^2(R)\tanh(R) \tag{62}$$

Substituting these in KdV equation results in

$$\begin{aligned} 0 = 2\sqrt{2}A^{\frac{5}{2}}\,\mathrm{sech}^2(R)\tanh(R) + 6A\,\mathrm{sech}^2(R)[-\sqrt{2}A^{\frac{3}{2}}\,\mathrm{sech}^2(R)\tanh(R)] + \\ A[4\sqrt{2}A^{\frac{3}{2}}\,\mathrm{sech}^4(R)\tanh(R) - 2\sqrt{2}A^{\frac{3}{2}}\,\mathrm{sech}^2(R)\tanh^3(R)]. \end{aligned} \tag{63}$$

Performing the multiplications yield

$$0 = 2\sqrt{2}A^{\frac{5}{2}}\operatorname{sech}^2(R)\tanh(R) - 6\sqrt{2}A^{\frac{5}{3}}\operatorname{sech}^4(R)\tanh(R) + 4\sqrt{2}A^{\frac{5}{2}}\operatorname{sech}^4(R)\tanh(R) - 2\sqrt{2}A^{\frac{5}{2}}\operatorname{sech}^2(R)\tanh^3(R). \quad (64)$$

Next, the identity $\tanh^2 x = 1 - \operatorname{sech}^2 x$ is applied.

$$0 = 2\sqrt{2}A^{\frac{5}{2}}\operatorname{sech}^2(R)\tanh(R) - 6\sqrt{2}A^{\frac{5}{3}}\operatorname{sech}^4(R)\tanh(R) + 4\sqrt{2}A^{\frac{5}{2}}\operatorname{sech}^4(R)\tanh(R) + 2\sqrt{2}A^{\frac{5}{2}}\operatorname{sech}^4(R)\tanh(R) - 2\sqrt{2}\,A^{\frac{5}{2}}\operatorname{sech}^2(R)\tanh(R) \quad (65)$$

Now, the first and last term cancel as do the three middle terms. Therefore, equation 59 has been shown to be a solution to equation 55. This result is in some ways unfortunate because it shows that the soliton solution depends on the L and C, which are contained in ξ, of the finite element in the model rather than only on global line parameters. The result is that the smaller the finite element the sharper the soliton. Therefore, this model is not a valid for a continuous line in the soliton or near soliton regime unless an additional frequency dependent loss mechanism is included. Such a loss mechanism will be presented in future sections once simulations based on the basic model are presented and the consequences of varying different parameters are discussed.

2.3.2 Finite Element Simulation of NLTLs

This section presents simulation results based on the model in Figure 3 which corresponds to Equation 23. A high level flowchart for the simulation is given in Figure 5 while the C++ code for this simulation is provided in Appendix G. The parameters used in these simulations were chosen so that the behavior of the line as a function of various parameters could be established. As a result, these simulations do not correspond to a specific geometry and material system.

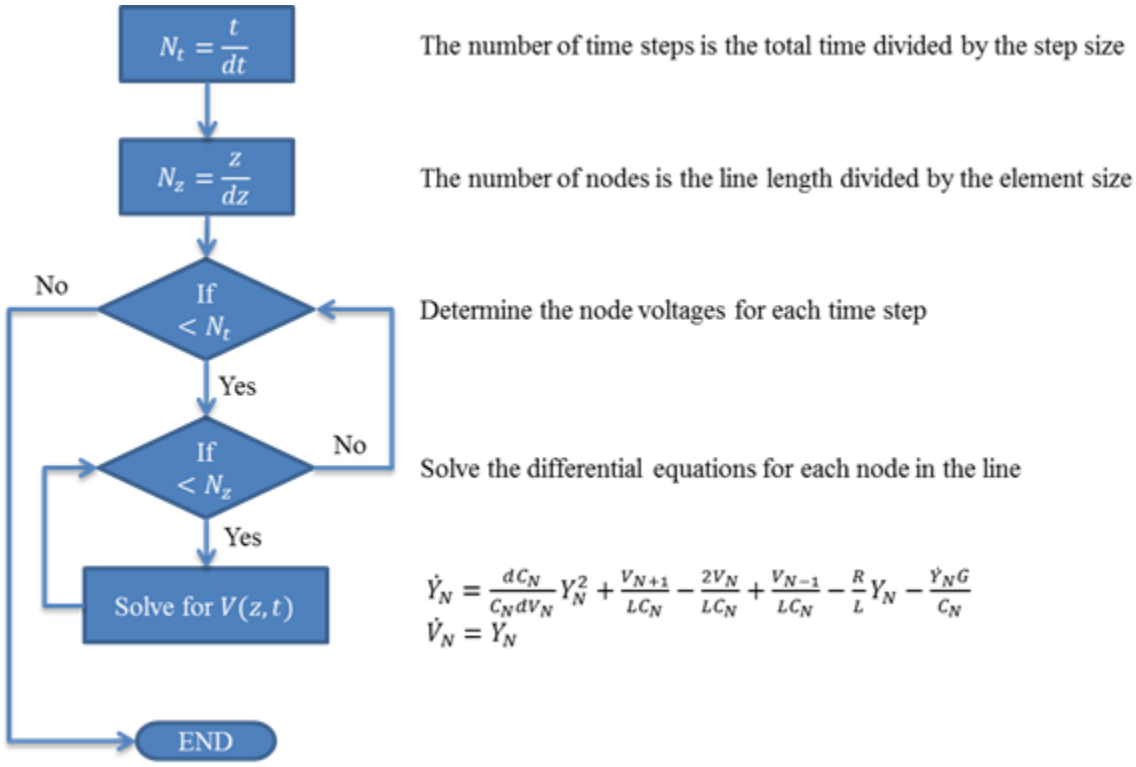

Figure 5: Simulation Flow Chart

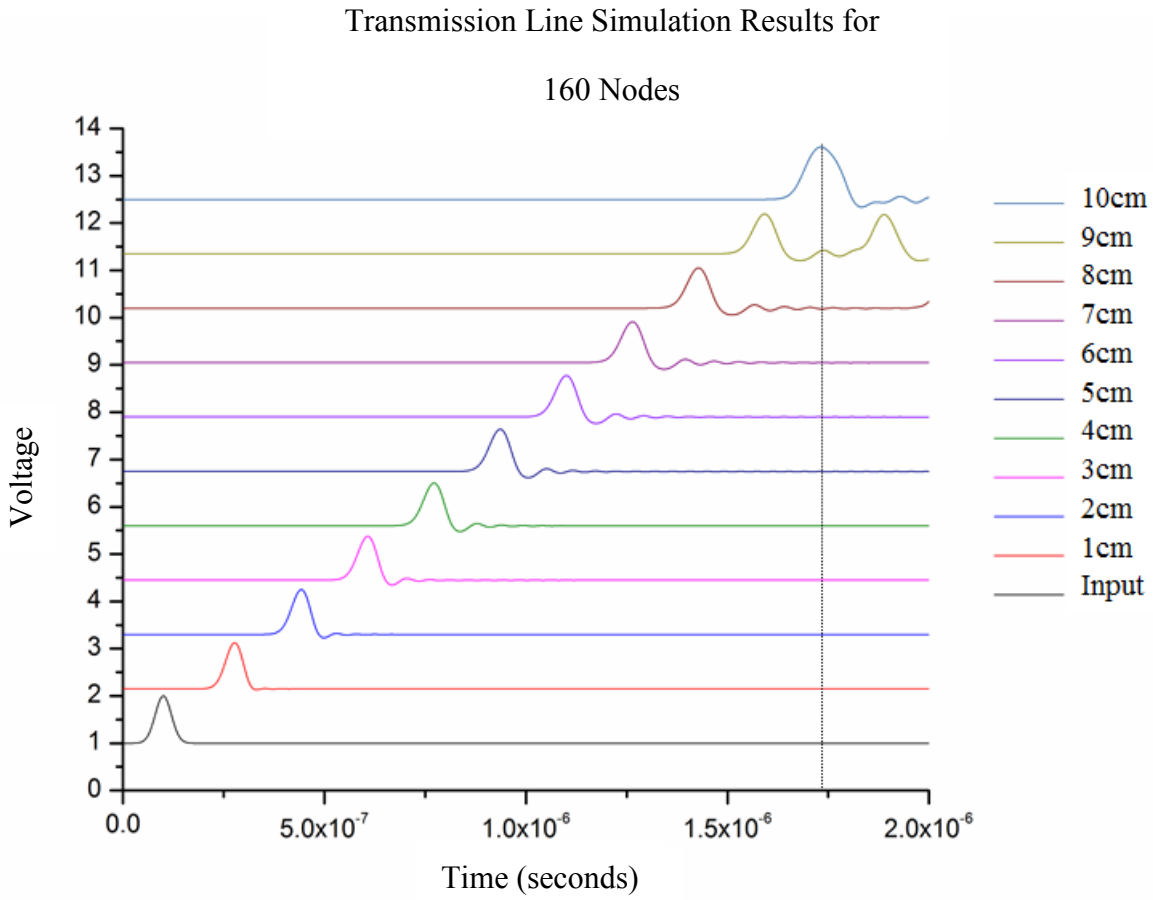

Figure 6: Example Nonlinear Transmission Line Simulation

Interpretation of the simulation output is done in the same way oscilloscope data would be interpreted. In Figure 6 each curve represents the voltage, as a function of time, calculated at a specific location. The bottom curve is the input and the rest are taken at evenly spaced intervals along the line. The dotted vertical line indicates the time the pulse reaches the end of the transmission line. Note the reflection pulse in the top most traces. This reflection is the result of the impedance mismatch at the end of transmission line terminated with an open circuit.

Because these simulations were performed to explore variations in line parameters multiple simulations must be compared. This was done by plotting the feature of interest as a

function of simulation parameter. Features of interest included rise time, pulse width, peak height, pulse energy, and propagation velocity. Simulation parameters were the number of nodes, the time step, the zero field dielectric constant, the capacitance, the nonlinearity, the series resistance, the parallel resistance, the line length, the maximum voltage, the DC offset, the pulse shape, the pulse width, the maximum frequency domain loss, the number of times the frequency domain filter is applied, and a dispersion factor. The number of nodes were the number of finite elements in the simulation. The time step was the Δt between calculations. In general a simulation with a larger number of nodes and a smaller time step was better. The zero field dielectric constant was a material parameter which was used in the calculation of the inductance. The capacitance was given per meter as if the dielectric as a vacuum. In other words the capacitance parameter was only a function of line geometry. The actual capacitance was calculated in the simulation using this parameter, the zero field dielectric constant, and the nonlinearity. The nonlinearity was the equation or look up table used to calculate the voltage dependent capacitance at each node. The series resistance, or metal losses, depended on the device geometry and materials. The parallel resistance represented the losses due to leakage current. It was desired that the series resistance be low and the parallel resistance be high. The line length was given in meters and was the physical distance from one end of the line to the other. The maximum voltage, the DC offset, the pulse shape, and the pulse width were parameters that control the type and size of the excitation. The pulse shape options were half sine, rising edge sigmoid, random square pulses, many sine periods, and Gaussian. The next two parameters, the maximum frequency domain loss and the number of times the frequency domain filter was applied, were related to the loss tangent of the material. These two parameters will be

discussed in more detail later. The higher the last parameter, the dispersion factor, the more dispersion was included in the simulation.

As an example of the procedure consider the process of selecting the time step for a specific simulation. First, all parameters except for the time step were fixed. These parameters were shown in Table 1. Next, the simulation was run with various values for the time step. Finally, the results of the simulation were compared. In this case, if the maximum absolute difference (MAD) between a simulation with a given time step and a simulation with half that given time step was below some threshold the time step is presumed to be sufficient.

Table 1: Parameters of Simulation for dt Discussion

Parameter	**Value**
Number of Nodes	1000
Time Step	Varied from 1×10^{-15} to $2^{15} \times 10^{-15}$ seconds
Zero Field Dielectric Constant	1000
Capacitance per Meter	2×10^{-10} Farads
Nonlinearity	$C(0)$ if $V < 0$ $\frac{0.44019\sqrt{2\pi}e^{1.1651}}{0.44019\sqrt{2\pi}e^{-\frac{V^2}{0.44019^2}+1.1651}} C(0)$ if $V \geq 0$
Series Resistance per Meter	0 Ohms
Parallel Resistance per Meter	1×10^{200} Ohms
Line Length	1×10^{-1} meters
Maximum Voltage	1×10^{-1} Volt
DC Offset	0 Volts
Pulse Shape	Gaussian
Pulse Width	1×10^{-8} seconds
Frequency Domain Filter Maximum Loss	10
Number of Applications of Frequency Domain Filter	0
Dispersion Factor	0

Figure 7 shows a simulation with a time step of 4.1×10^{-12} seconds, top panel solid lines, and a simulation with a time step of 2.0×10^{-12} seconds, top panel dashed line, along with the absolute difference between the two curves, bottom panel. The dotted vertical lines

indicate the times the pulse reaches the end of the line. The dashed vertical lines indicate the times the reflected pulse reaches the beginning of the line again. Both sets of vertical lines are referenced to the simulation with the 2.0×10^{-12} second time step. The MAD of 0.1175 V occurs in the top curves at approximately 1.5×10^{-8} seconds.

Figure 8 presents simulations with time steps of 2.0×10^{-12} seconds and 1.0×10^{-12} seconds in the same way. In this case, the MAD is 0.0641 V. Figure 9 shows the MAD for the set of simulations with the parameters defined in Table 1. Two points obviously did not fit the pattern of the rest. This resulted from simulations with large time steps being so bad they were nearly flat lines. If those two data points were eliminated, the rest fit a curve, $MAD = 2 \times 10^{10} dt^{0.9741}$, with an $R^2 = 0.9997$. Such a fit allowed for an extension to arbitrary precision. Well informed decisions about the time step necessary could now be made once the simulation precision was chosen.

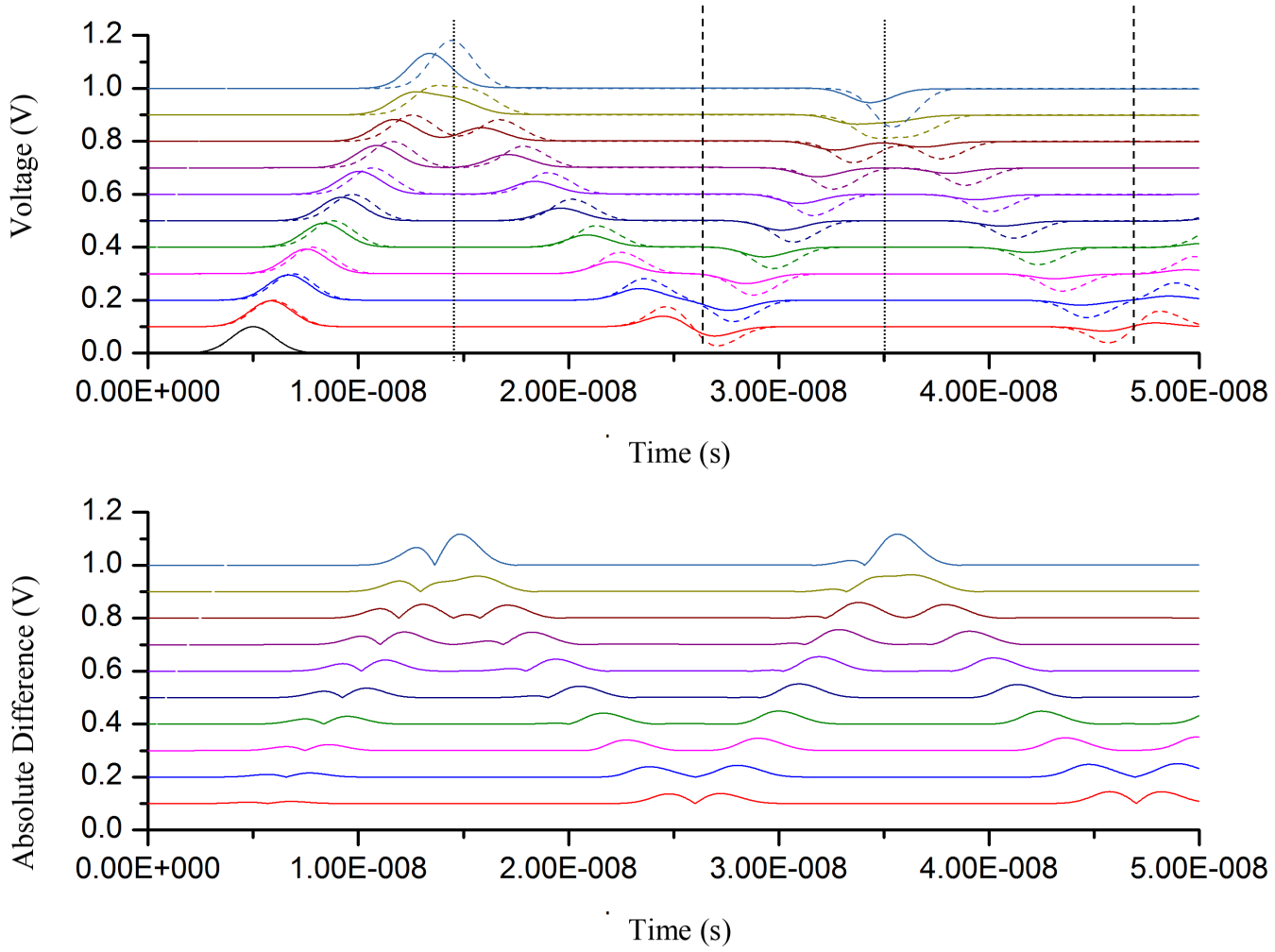

Figure 7: Simulations with $dt = 4.1 \times 10^{-12}$ seconds (top solid) and $dt = 2.0 \times 10^{-12}$ seconds (top dashed) along with the absolute difference (bottom) between the two simulations

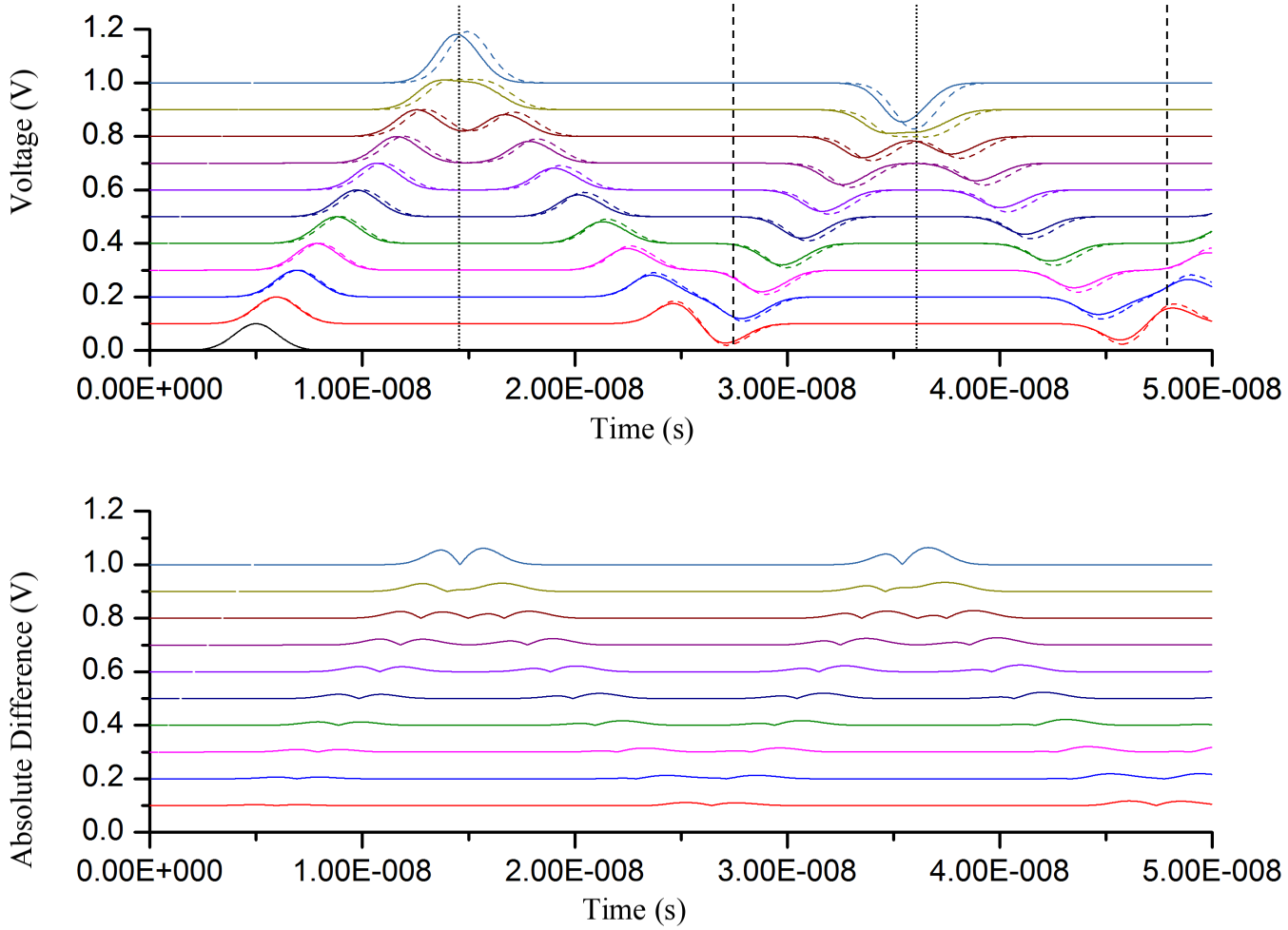

Figure 8: Simulations with $dt = 2.0 \times 10^{-12}$ seconds (top solid) and $dt = 1.0 \times 10^{-12}$ seconds (top dashed) along with the absolute difference (bottom) between the two simulations

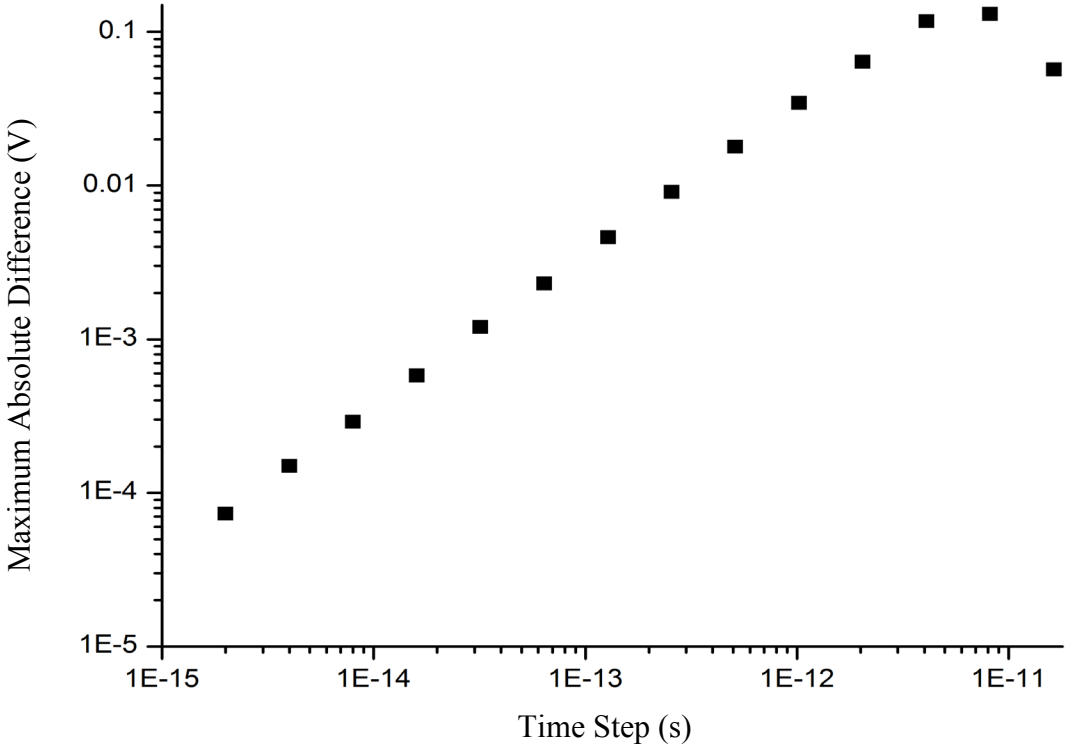

Figure 9: MAD versus dt

Note that if instead of looking at the difference at a single point this discussion could have equally considered the root mean square difference. Such an analysis, which looks at the integrated difference, shows a similar trend. MAD was chosen over RMSD since two simulations might have a low RMSD because they match for most of the results yet still differ at some point of interest, such as the peak or the rising edge.

Just as the number of time steps affect the quality of a simulation, so do the number of nodes. When there are insufficient nodes a simulation may try to develop frequencies beyond what the finite element is capable of supporting which results in ringing or other artifacts. This is evident from the magnitude component of the Bode plot, shown in Figure 10, of an unloaded finite element, given the parameters in Table 1 when there are 100, 200, and 300 nodes. Note that through about 10^{10} Hz each of the curves was approximately 0dB meaning the element has

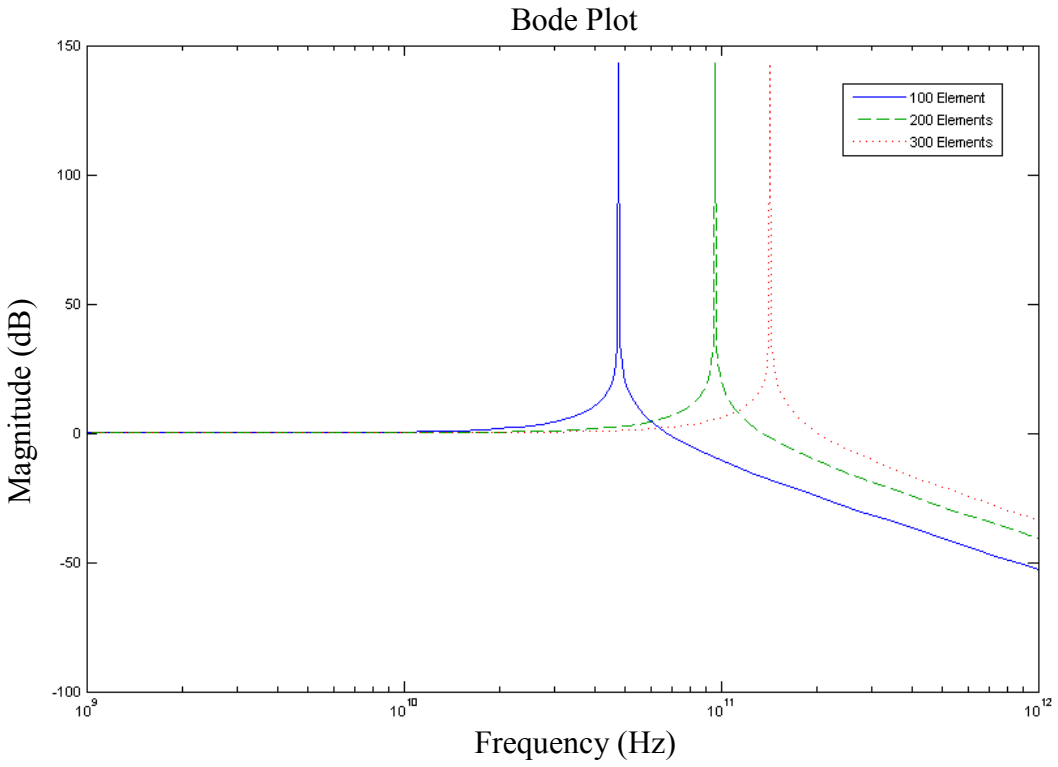

Figure 10: Bode Plot for Simulation with 100, 200, and 300 Nodes

unity gain. As the frequencies approached the resonant frequency of the finite element the circuit began to ring. This resonance occurred at 4.77×10^{10} Hz for 100 nodes, 9.55×10^{10} Hz for 200 nodes, and 1.43×10^{11} Hz for 300 nodes. At frequencies higher than resonant frequency, the circuit attenuated the signal. To ensure that the limited frequency response of the finite element had negligible effect on the simulation results the same process that was used for establishing an appropriate time step was undertaken for the number of nodes in a simulation. For the parameters in this simulation, with the time step fixed at 1.6×10^{-14} seconds, the MAD between 1000 nodes and 2000 nodes was 1.2×10^{-3} V. Therefore, the total error was quantified for these parameters to be no greater than 1.8×10^{-3} V, which was the sum of the MADs. The simulations in Sections 2.3.2.1 and 2.3.2.2, which explore the effects of various parameters, have undergone this process in order to quantify the error and ensure the sum of the MADs between a

given simulation and one with twice the resolution time and one with twice the resolution in space is less than five percent of the peak input voltage unless otherwise specified.

2.3.2.1 Effect of Propagation Distance

Pulses propagating along a nonlinear transmission line change in shape as a function of distance. This change in shape is a result of redistribution of energy due to the nonlinear dielectric material. This section serves to provide some background information concerning generally expected behavior of a pulse as it propagates along a nonlinear transmission line. Before examining a specific simulation, a general discussion will provide a background and explore the expected behavior.

Since the nonlinear elements in the transmission line are modeled with nonlinear capacitors this analysis will start from that point. The time constant of a resistive, inductive, and capacitive circuit decreases if the capacitance is decreased. In other words, the smaller the capacitor the faster it charges or discharges. Therefore, a pulse will travel slower along a transmission line with a higher capacitance and more quickly along a transmission line with a lower capacitance. More specifically, the phase velocity of a transmission line is [42]

$$v_p = \frac{1}{\sqrt{LC}\sqrt{1-j\left(\frac{R}{\omega L}+\frac{G}{\omega C}\right)}}. \tag{66}$$

If the losses are negligible then $v_p = \frac{1}{\sqrt{LC}}$. In this case, the inductance is a result of the transmission line geometry and is therefore constant. Finally, since the capacitance of the dielectric changes with voltage, the phase velocity becomes

$$v_p = \frac{1}{\sqrt{LC(V)}}. \tag{67}$$

The change in capacitance as a function of voltage for the simulation defined by Table 2 and the resulting change in phase velocity are shown in Figure 11. The rise time, fall time, energy, and root mean square difference for a Gaussian fit for a pulse passing 1cm increments are shown in Figure 12. The rise time is defined as the Δt between the time a pulse passes ten percent of its maximum potential and the time it passes ninety percent of its maximum potential. The fall time of a pulse is defined as the Δt it takes for the pulse to go from 90% of its maximum to 10% of its maximum.

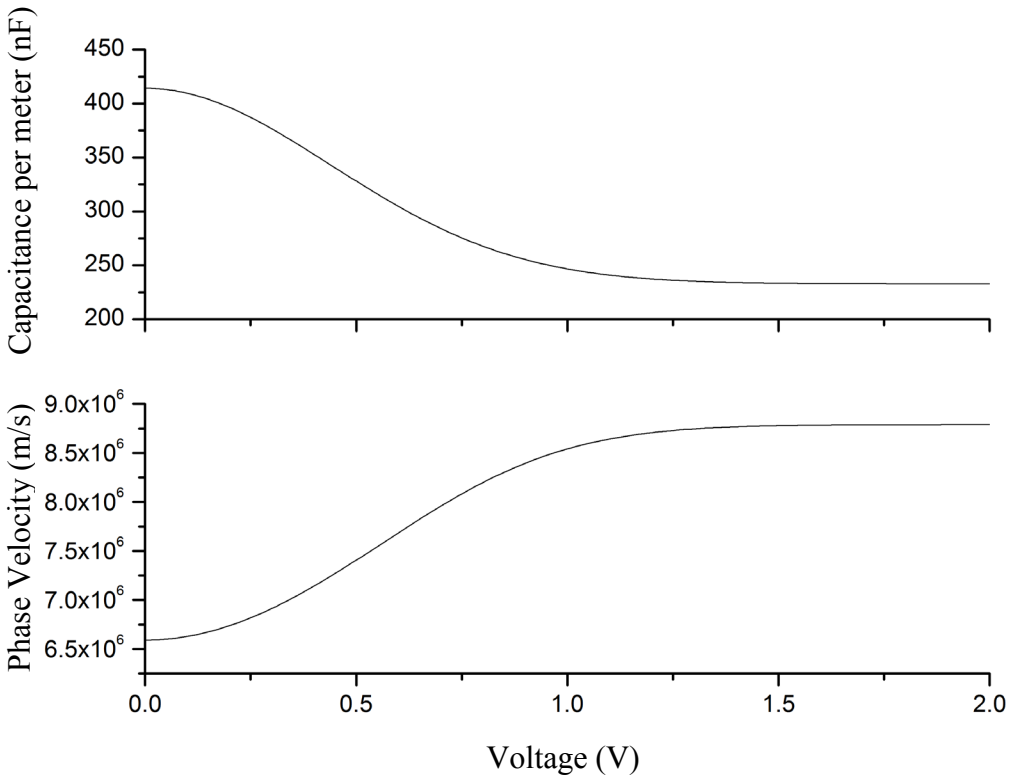

Figure 11: Capacitance and Phase Velocity for Transmission Line Defined by Table 2

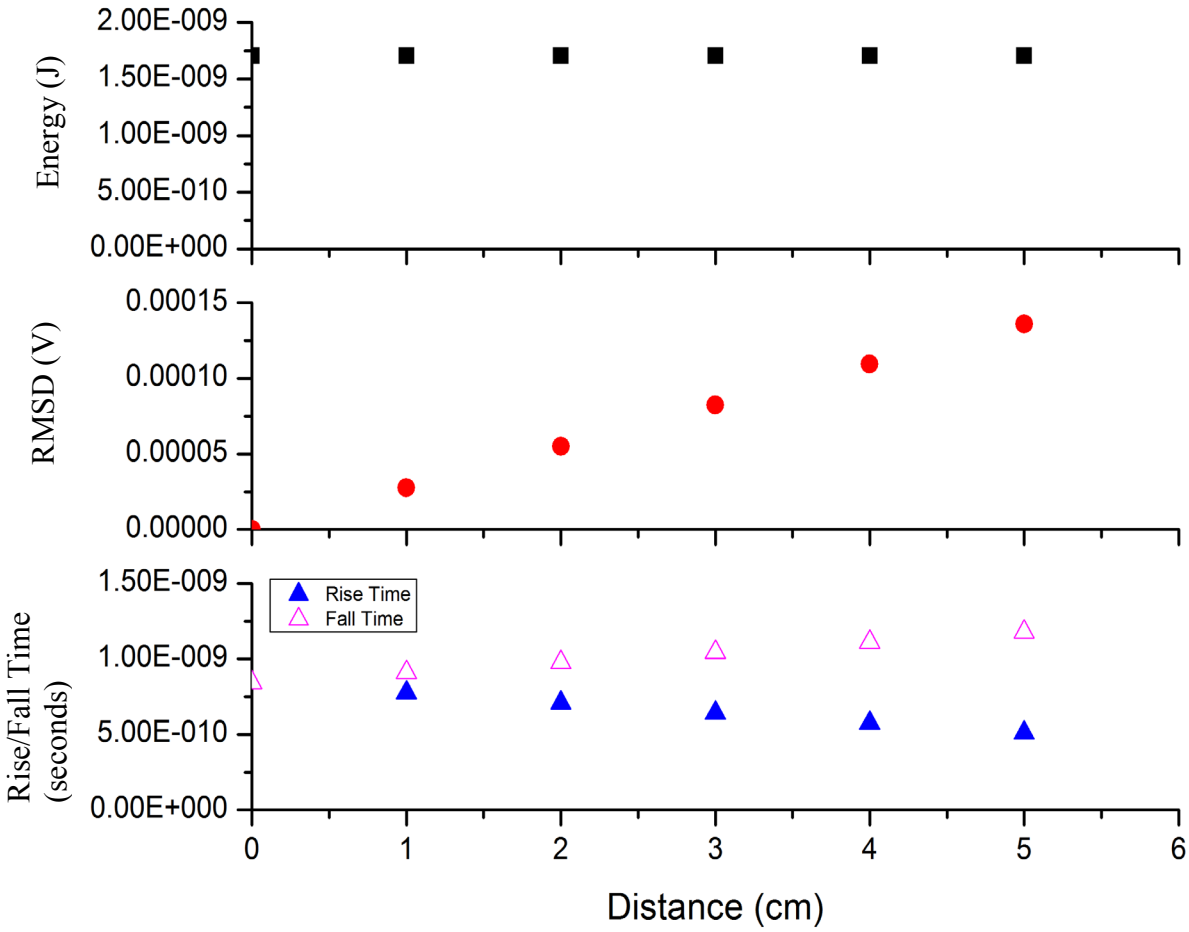

Figure 12: Energy, Root Mean Square Difference Versus Gaussian Fit, and Rise and Fall Time of Pulse Passing 1cm increments

Table 2: Parameters of Simulation for Propagation Distance Discussion

Parameter	**Value**
Number of Nodes	24000
Time Step	4×10^{-15} seconds
Zero Field Dielectric Constant	1000
Capacitance per Meter	2×10^{-10} Farads
Nonlinearity	$C(0)$ if $V < 0$ $\frac{0.44019\sqrt{2\pi}e^{1.1651}}{0.44019\sqrt{2\pi}e^{-\frac{V^2}{0.44019^2}+1.1651}} C(0)$ if $V \geq 0$
Series Resistance per Meter	0 Ohms
Parallel Resistance per Meter	1×10^{200} Ohms
Line Length	1×10^{-1} meters
Maximum Voltage	4×10^{-1} Volt
DC Offset	0 Volts
Pulse Shape	Gaussian
Pulse Width	5×10^{-9} seconds
Frequency Domain Filter Maximum Loss	10
Number of Applications of Frequency Domain Filter	0
Dispersion Factor	0

2.3.2.2 Effect of Peak Voltage

Because the effects of a nonlinear transmission line are voltage dependent it was important to examine what happens as the peak voltage in the pulse was increased. Propagation velocity, maximum voltage, and rise time are all affected by a change in the maximum voltage of the input pulse. The parameters for the voltage dependent simulations in this section are shown in Table 3.

Table 3: Parameters of Simulation for Peak Voltage Discussion

Parameter	**Value**
Number of Nodes	24000
Time Step	4×10^{-15} seconds
Zero Field Dielectric Constant	1000
Capacitance per Meter	2×10^{-10} Farads
Nonlinearity	$C(0)$ if $V < 0$ $\frac{0.44019\sqrt{2\pi}e^{1.1651}}{0.44019\sqrt{2\pi}e^{-\frac{V^2}{0.44019^2}+1.1651}} C(0)$ if $V \geq 0$
Series Resistance per Meter	0 Ohms
Parallel Resistance per Meter	1×10^{200} Ohms
Line Length	1×10^{-1} meters
Maximum Voltage	1×10^{-2} to 4.1×10^{-1} Volts
DC Offset	0 Volts
Pulse Shape	Gaussian
Pulse Width	5×10^{-9} seconds
Frequency Domain Filter Maximum Loss	10
Number of Applications of Frequency Domain Filter	0
Dispersion Factor	0

2.3.2.2.1 Propagation Velocity

Since higher voltages induce a lower capacitance, it was expected that the peak of a pulse with a larger maximum potential would travel along the line faster than the peak of a pulse with a smaller maximum potential. Figure 13 shows the time when the peak of a pulse with a given maximum input voltage passed the 5 cm mark in the simulation as a function of the peak voltage.

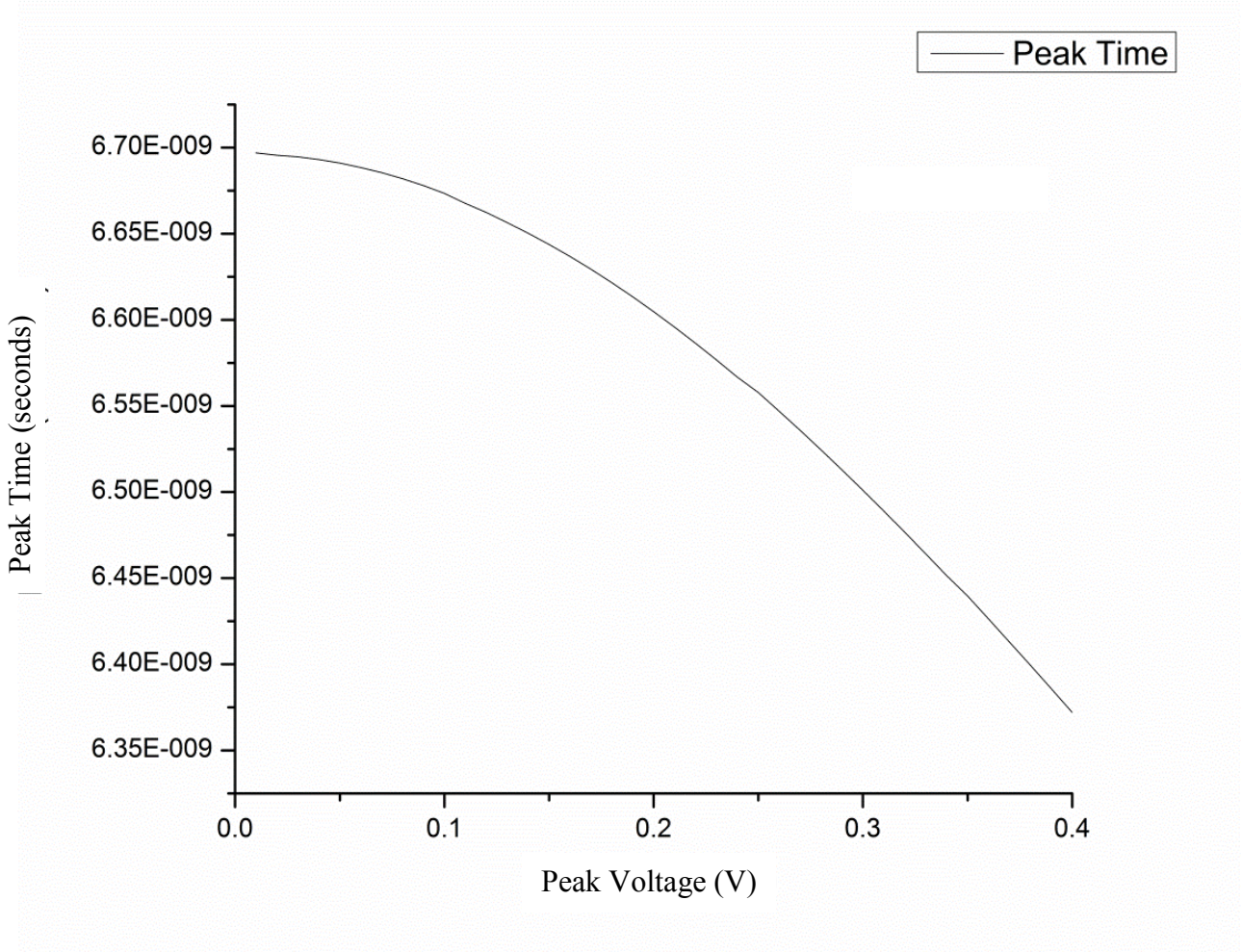

Figure 13: Time a Peak Passes 5cm Mark versus Peak Voltage

2.3.2.2.2 Rise Time and Fall Time

Although the rise time as a function of distance has already been discussed, the rise time as a function of peak voltage was equally important. This section examines the rise time as a function of peak voltage by fixing the propagation distance at 5 cm. Figure 14 shows the rise and fall times of a series of pulses, as they pass the 5 cm mark, as a function of the input peak voltage. As expected, the rise time decreased and the fall time increased with increasing peak voltage.

2.3.2.2.3 Pulse Shape

If an input pulse has too little amplitude the dielectric constant of the transmission line will remain nearly constant and the pulse should propagate as if it were on a linear line. For

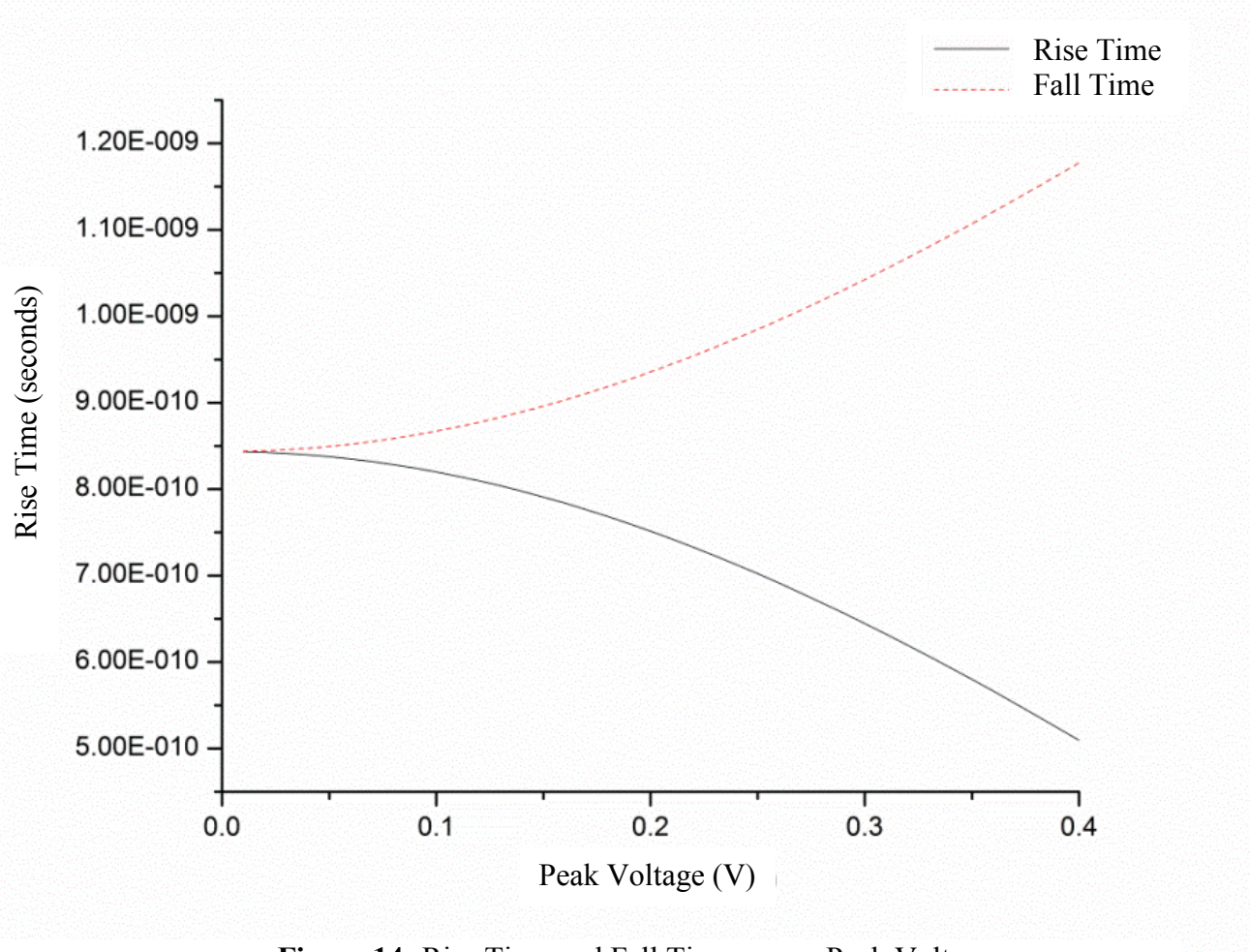

Figure 14: Rise Time and Fall Time versus Peak Voltage

pulses with higher amplitudes, the nonlinearity will dominate and the pulse should sharpen into a shockwave.

Figure 15 shows the root mean square difference, normalized by peak voltage, between a pulse measured at a given point along the line and a Gaussian fit of that curve. As expected, the lower the voltage the more Gaussian like the pulse stayed. Additionally, the pulses evolved away from Gaussian as they propagated. In other words, increasing the amount of the nonlinearity by increasing either the pulse amplitude or the distance of interaction increased the deformation of the pulse.

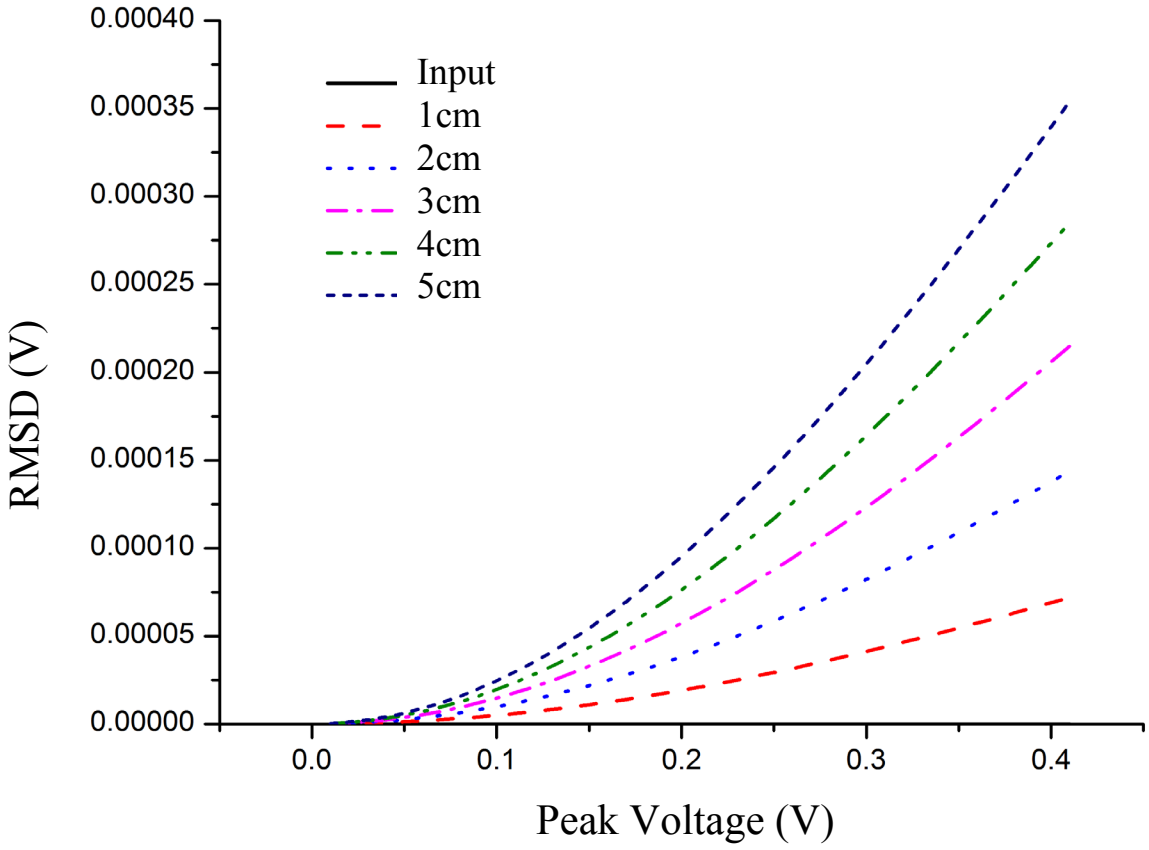

Figure 15: Normalized RMSD between Gaussian and pulse measured at 1 cm intervals for a series of peak voltages

The soliton solution of the KdV equation presented in Equation 57 was not fit for these simulations for two reasons. First, the assumption that the linear term of the expansion of the capacitance dominates the behavior was violated. The Taylor series expansion of $C(V)$, which is defined in Table 3, about $0V$, with the derivatives calculated numerically, is

$$C(V) = 1 - 3.7007 \times 10^{-8} \cdot V - 1.0485 \cdot V^2 \cdots. \tag{68}$$

Therefore, the first order term remained at least ten times larger than the second order term only until about $5 \times 10^{-9} V$. With such a small potential, as shown above, the simulated line behaved in a linear way over the distances examined. However, higher order terms in the nonlinearity should have still resulted in soliton propagation [52] meaning even a pulse with a

larger voltage should have formed a soliton. A second, bigger problem lay in the size of the finite element itself. Since this finite element model was intended to simulate a continuous line, the smaller the element the better. In fact, the dispersion relations in Equation 27 and Equation 30 have a dependence on the finite element circuit elements L and C. When at or near the limit where solitons form, the simulation results depend on the element itself. Therefore, because the soliton solution to the KdV equation depends on the inductance and capacitance of the finite element rather than the dielectric dispersion and loss all the solitons observed using this simulation have a bandwidth limited only by the finite element resonance meaning a higher resolution simulation results in a higher bandwidth soliton.

2.3.2.3 Effect of Loss Tangent

The simulation program was written in such a way as to include a frequency dependent in order to account for the loss tangent. This section is dedicated to this loss, the inclusion of this loss in the simulation, and the results of including this loss. The first attempt at including loss attempted to exploit Equation 69 by simply performing a fast Fourier transform (FFT) on the state of the line, applying the loss function, and performing an inverse fast Fourier transform (IFFT). Mathematically, the result of these operations is shown in Equation 70.

$$2\pi f = \omega = v_p q \tag{69}$$

$$V[0:N] = \mathcal{F}^{-1}\{h[\omega] \cdot \mathcal{F}\{V[0:N]\}\} \tag{70}$$

Unfortunately, since the phase velocity in Equation 69 is a function of voltage this approach was not valid. A different approach which used arrays to buffer the signals in time is displayed in a modified version of the simulation flow chart already shown (Figure 5), and is shown in Figure 16. The new flow chart includes the application of a loss function. This loss function was applied in a three step process. First, the voltage at each node was buffered so that $V_N(t_{current}: t_{current-n}) \equiv V_N(t_{c:c-n})$ was an array that held the currently calculated voltage at node N along with the previous n calculations. Next, the FFT of $V(t_{c:c-n})$ was taken resulting in $H(j\omega)$ where j is the imaginary number and ω is related to the frequency f by the simulation time step Δt by Equation 71.

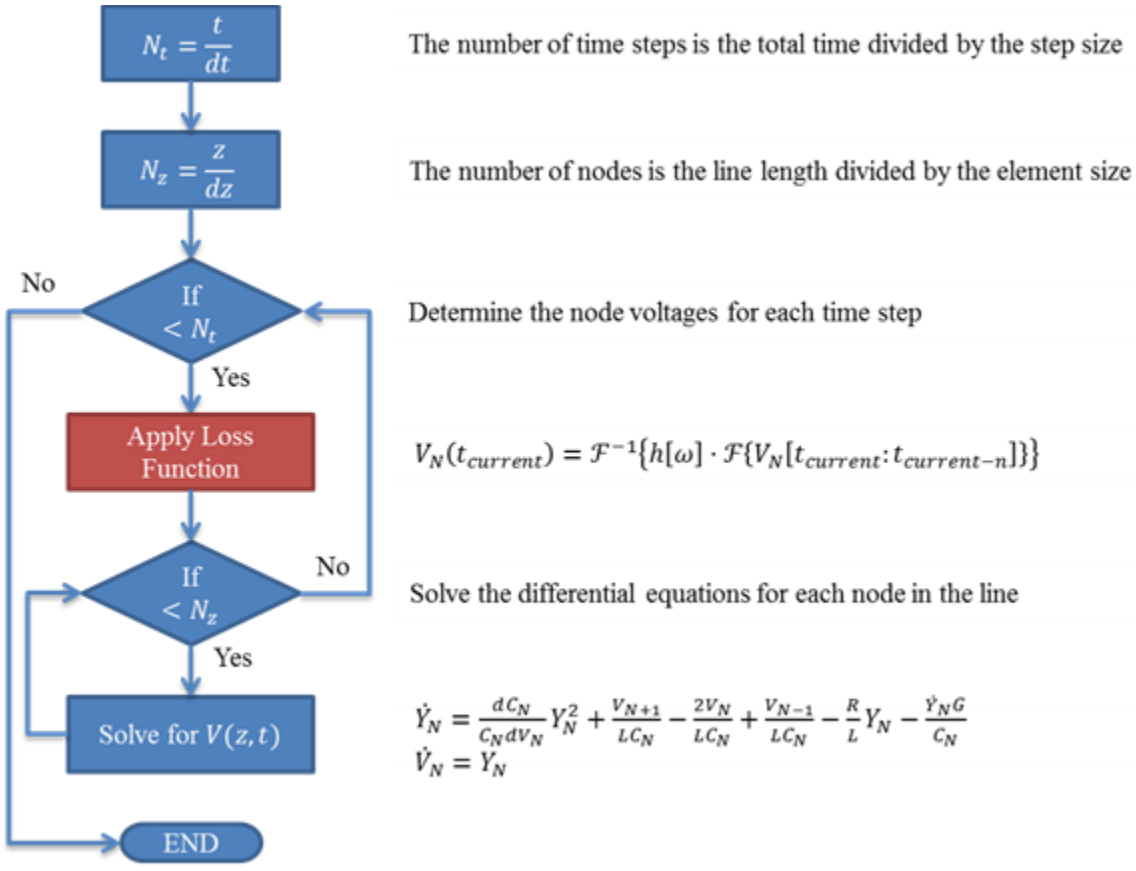

Figure 16: Flow Chart of Transmission Line Simulation Including Dielectric Loss

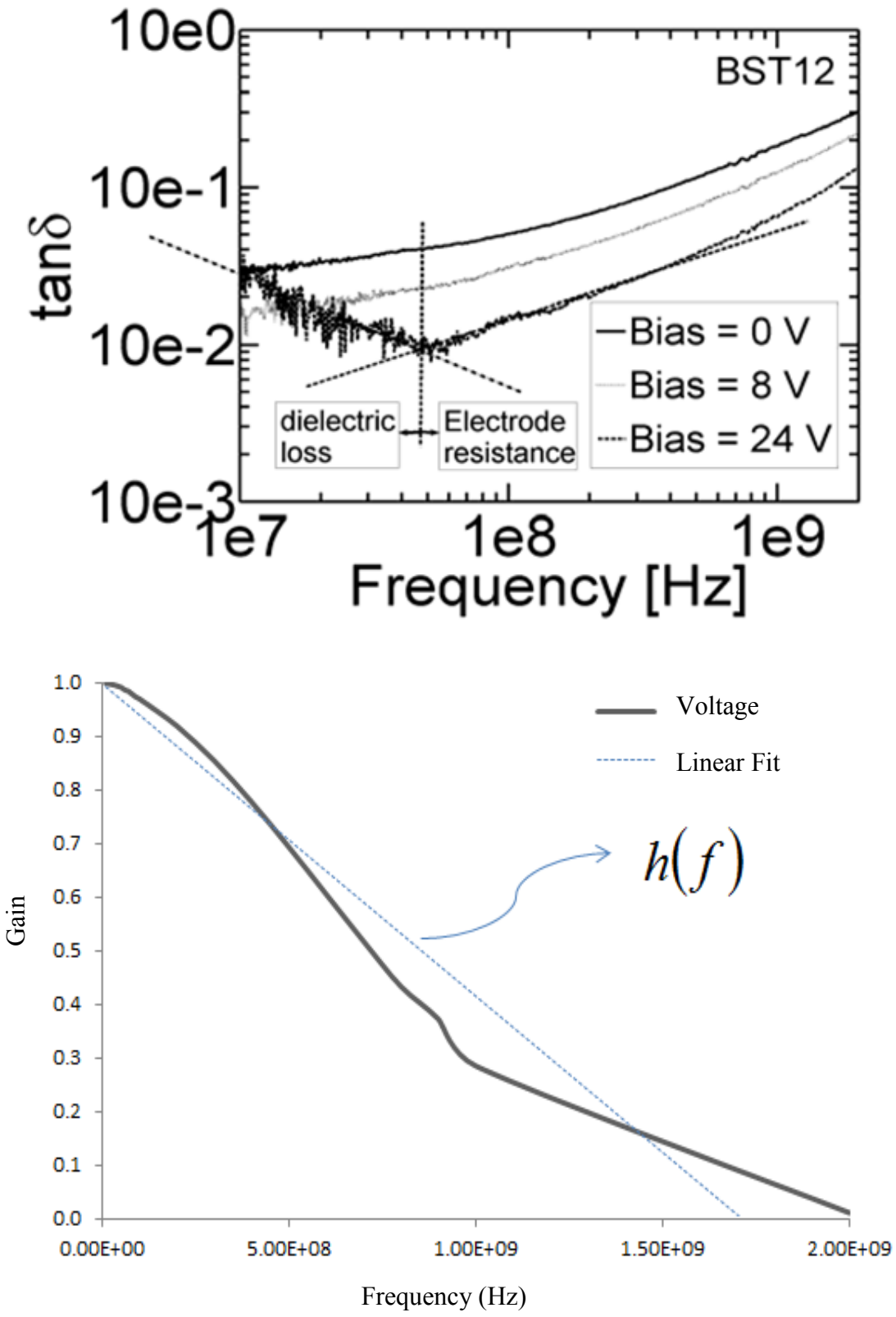

Figure 17: Loss Tangent (top) [44] and Corresponding Loss Function (bottom)

$$f = \frac{\omega}{2\pi\Delta t} \tag{71}$$

Once the frequency spectrum of each node was established, they were each multiplied $h[\omega]$ which is a filter that represented the loss tangent. Finally, the inverse fast Fourier transform (IFFT) was calculated and $V_N(t_{current})$ was replaced with the first element in buffer array.

The function $h[\omega]$ was chosen to be linear in order to fit the reported loss tangent of barium strontium titanate [53]. Figure 17 shows the loss tangent of BST [53] as well as the same data converted to a function of attenuation. Since applying the loss function was computationally heavy it was not necessarily applied after every time step calculation. Instead, the simulation was written such that one of the input parameters adjusted the frequency with which the loss function was applied.

Because of the way the loss tangent was included in the simulation several difficulties arose. The primary issue was that of comparability. Specifically, changing the time step changed the slope of the loss function while changing the number of finite elements changes the number of times the loss function was applied. Resolution of these issues is left for future work. Here only two simulations, the parameters of which are in Table 4, are presented and discussed. The results of these simulations are shown in Figure 18. Because the frequency dependent loss function, which represents the loss tangent of the material, attenuated higher frequencies it became possible to simulate a continuous line with the finite element model when the resonant frequency of the finite element was higher than the maximum frequencies allowed to propagate on the line.

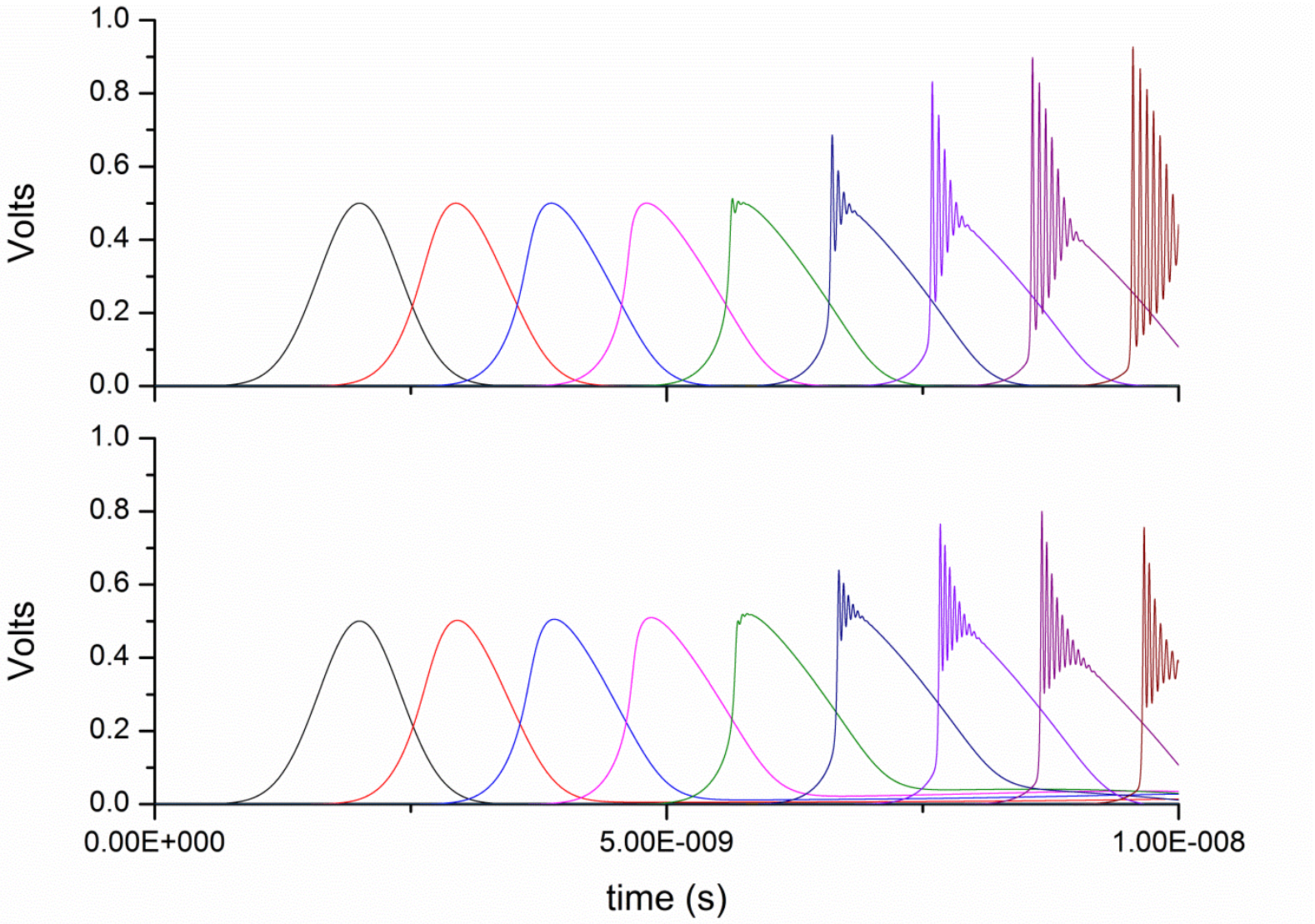

Figure 18: Pulse at 10mm increments on transmission line without (top) and with (bottom) frequency dependent loss function

Table 4: Simulation Parameters for Loss Tangent Analysis

Parameter	**Value**
Number of Nodes	1000
Time Step	1.28×10^{-13} seconds
Zero Field Dielectric Constant	1000
Capacitance per Meter	2×10^{-10} Farads
Nonlinearity	$C(0)$ if $V < 0$ $\frac{0.44019\sqrt{2\pi}e^{1.1651}}{0.44019\sqrt{2\pi}e^{-\frac{V^2}{0.44019^2}+1.1651}} C(0)$ if $V \geq 0$
Series Resistance per Meter	0 Ohms
Parallel Resistance per Meter	1×10^{200} Ohms
Line Length	1×10^{-1} meters
Maximum Voltage	0.5 Volts
DC Offset	0 Volts
Pulse Shape	Gaussian
Pulse Width	4×10^{-9} seconds
Frequency Domain Filter Maximum Loss	0.000 (lossless) and 0.001 (lossy)
Number of Applications of Frequency Domain Filter	156250
Dispersion Factor	0

An analysis of the energy in the pulse as it passed probes at 10mm increments, Table 5, verified that the algorithm was indeed lossy. Additionally, the power spectral density taken at 60mm, Figure 19, shows that the simulation which included losses had reduced high frequency components. In this case, the peak nearest the DC peak of the simulation including the loss function was 46% of the magnitude of the same peak for the lossless simulation. Note that the peaks were not at the same frequency because the losses effectively increased the resistance and thus the resonant frequency of the finite element.

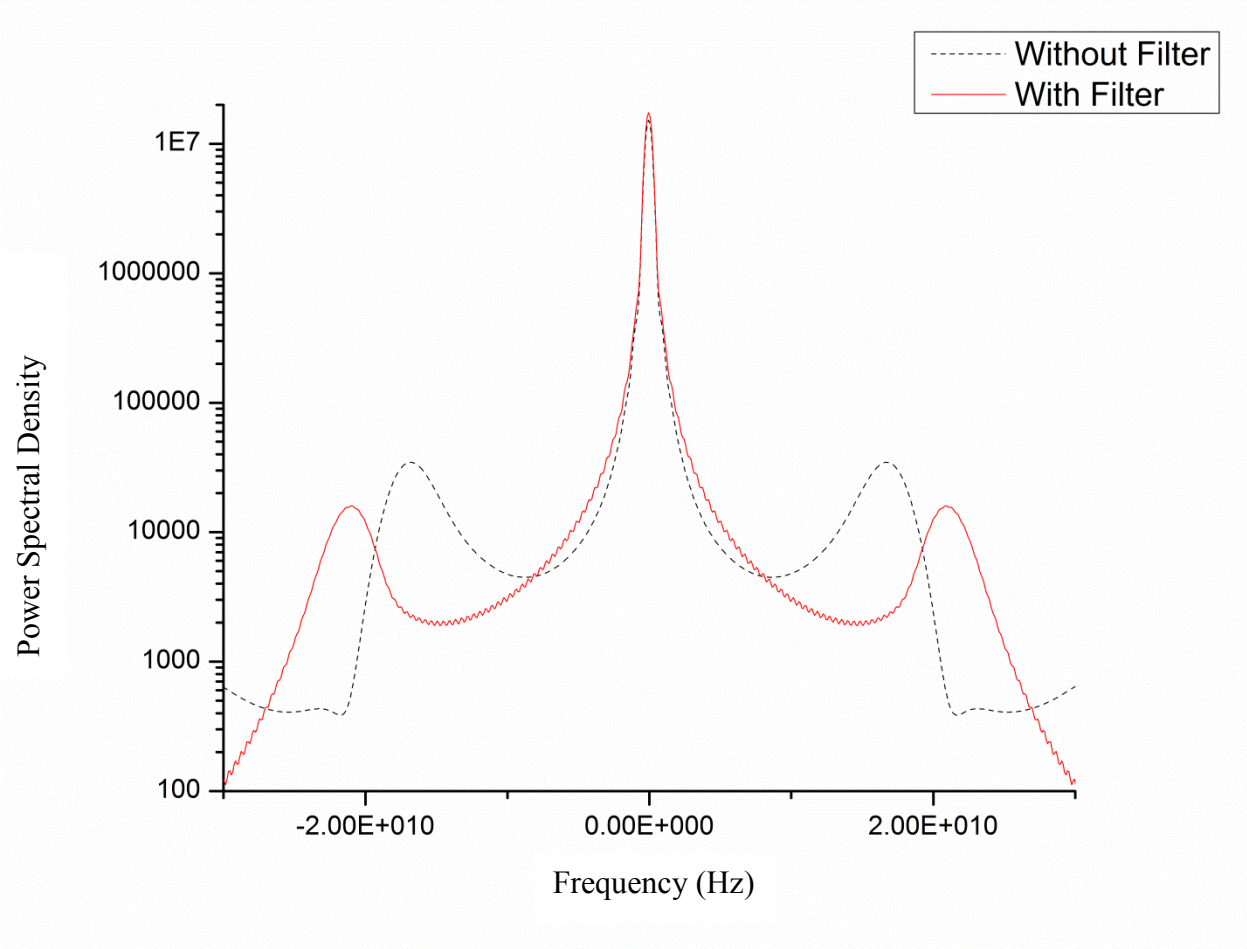

Figure 19: Power Spectral Density of Simulation With (Solid Red) and Without (Dashed Black) Frequency Dependent Loss

Table 5: Energy Analysis of Lossy TL Simulation

Distance (mm)	Pulse Energy (J)	Percent Energy Compared to Input Pulse (%)	Difference in Energy Compared to 10mm Earlier (J)
0	1.009235×10^{-9}	100.00	
10	1.009210×10^{-9}	100.00	2.44×10^{-14}
20	1.009169×10^{-9}	99.99	4.10×10^{-14}
30	1.009079×10^{-9}	99.97	9.00×10^{-14}
40	1.008734×10^{-9}	99.85	3.45×10^{-13}
50	1.007254×10^{-9}	99.80	1.48×10^{-12}
60	1.003124×10^{-9}	99.59	4.13×10^{-12}

2.3.2.4 Dielectric Dispersion

Since the dielectric constant of BTO is a function of frequency, as shown in Figure 20 [54], different frequency components experience different capacitances and thus propagate at different rates. To account for this in the simulation a five step process was used. First, an expanded line state, written as $V[0{:}\,N_{expanded}]$, was created by repeating node voltages to account for variable finite element time constants due to capacitance changes resulting from the nonlinearity. Graphically, the process of creating an expanded line state is shown in Figure 21. Next, the frequency domain signal of the expanded line state was obtained by taking the FFT. At this point, the Fourier components were advanced to account for the dielectric dispersion with higher frequencies being advanced more than lower frequencies. Fourth, an IFFT resulted in a

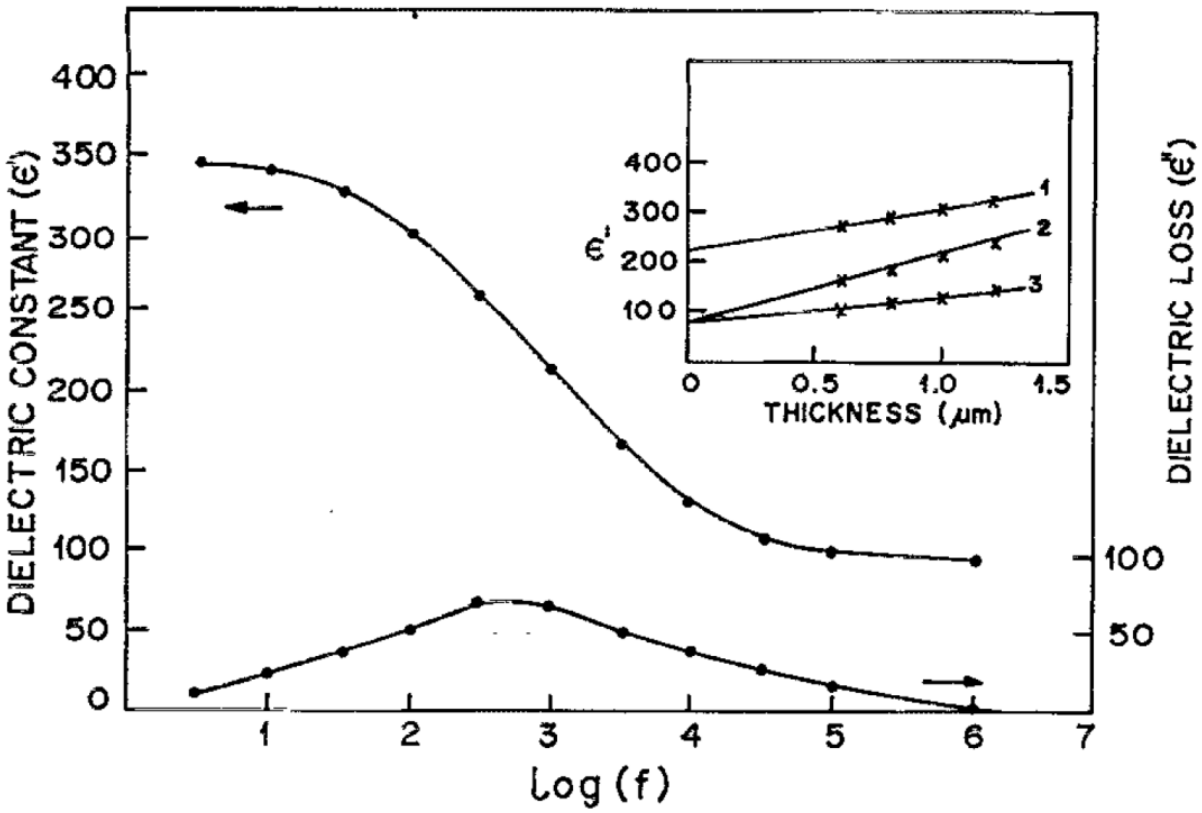

Figure 20: Dielectric constant versus frequency [45]

new expanded line state. Finally, the expanded line state was reduced to a normal line state by selecting a representative value and the next time step calculations were performed. Comparison of dispersive simulations was problematic for the same reasons as comparisons of the lossy simulations discussed in Section 2.3.2.3 are problematic. Therefore, the results presented in this section were examined for sever artifacts such as ringing or power gain but were not directly compared to simulations with twice the number of nodes and time steps.

Results for simulations, with the nonlinearity deactivated, that account for the dispersion using the strategy outlined above show an opposite behavior to the lines with nonlinearity but no dispersion. Additionally, these simulations show that, as expected, dispersion lengthens a pulse. Rise times, fall times, and total pulse duration for simulations, the parameters of which are in Table 6, of a dispersive linear transmission line are shown in Figure 22. The change in dispersion factor between data sets is a factor of two. It is hopeful that one effect of dispersion is to sharpen the falling edge while lengthening the rising edge which might compensate for the sharpening rising edge and lengthening falling seen in the nonlinear simulations. If these effects are properly balanced then a soliton should indeed be achievable. Unfortunately, a simulation that balances these effects without showing artifacts has yet to be found.

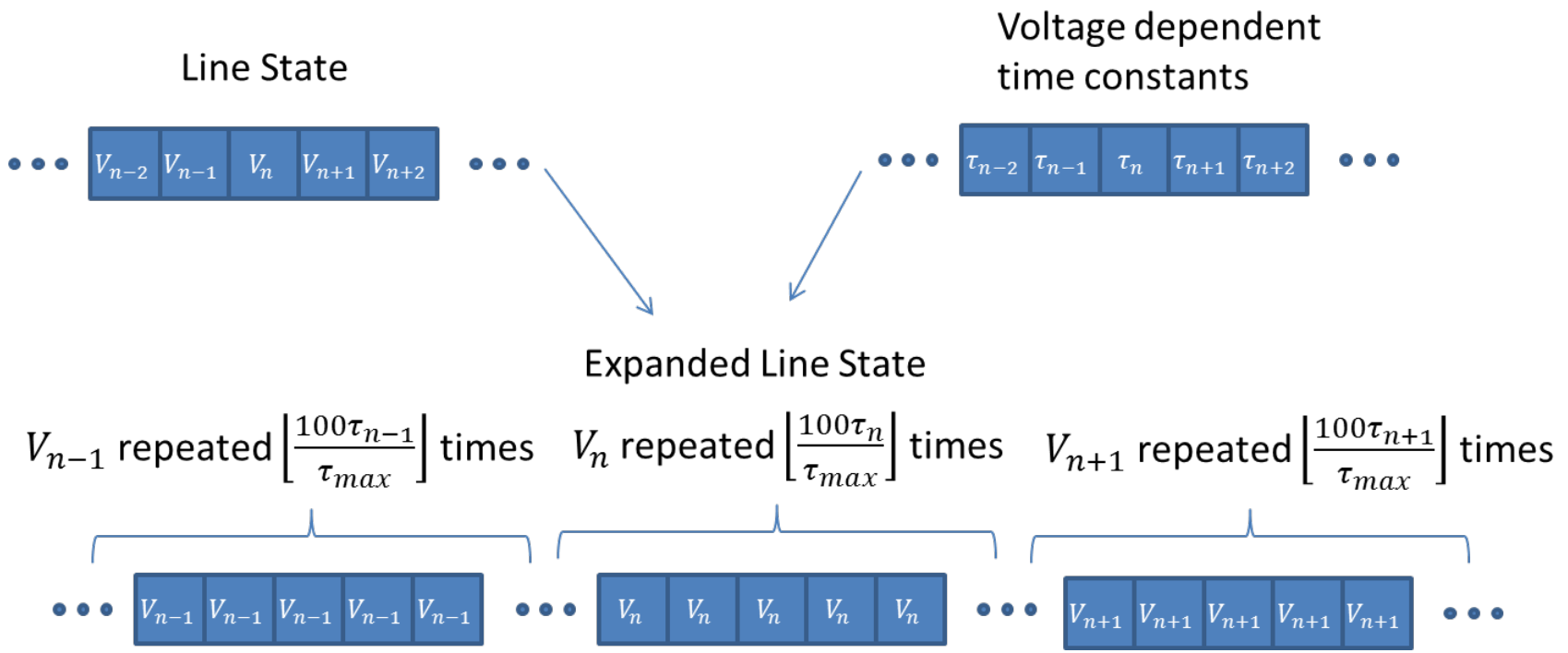

Figure 21: Creation of expanded line state

Table 6: Parameters for Simulations for Dispersion Discussion

Parameter	Value
Number of Nodes	24000
Time Step	6.4×10^{-14} seconds
Zero Field Dielectric Constant	1000
Capacitance per Meter	2×10^{-10} Farads
Nonlinearity	$C(0)$ if $V < 0$ $\frac{0.44019\sqrt{2\pi}e^{1.1651}}{0.44019\sqrt{2\pi}e^{-\frac{V^2}{0.44019^2}+1.1651}} C(0)$ if $V \geq 0$
Series Resistance per Meter	0 Ohms
Parallel Resistance per Meter	1×10^{200} Ohms
Line Length	1×10^{-1} meters
Maximum Voltage	2 Volts
DC Offset	0 Volts
Pulse Shape	Gaussian
Pulse Width	5×10^{-9} seconds
Frequency Domain Filter Maximum Loss	10
Number of Applications of Frequency Domain Filter	0
Dispersion Factor	$2^n \times 10^{-14}$

2.4 Theory Conclusion

This chapter has shown that, in theory, sharpening should be achievable with an electrically nonlinear transmission line. Furthermore, the amount of sharpening is a function of distance, pulse parameters, and transmission line parameters. Additionally, it has been shown that solitons could be forced through the fabrication of a line with a repeating unit which could be modeled by KdV equation. There is also some support for solitons resulting from the dielectric dispersion and nonlinearity balancing, although no conclusive evidence was found.

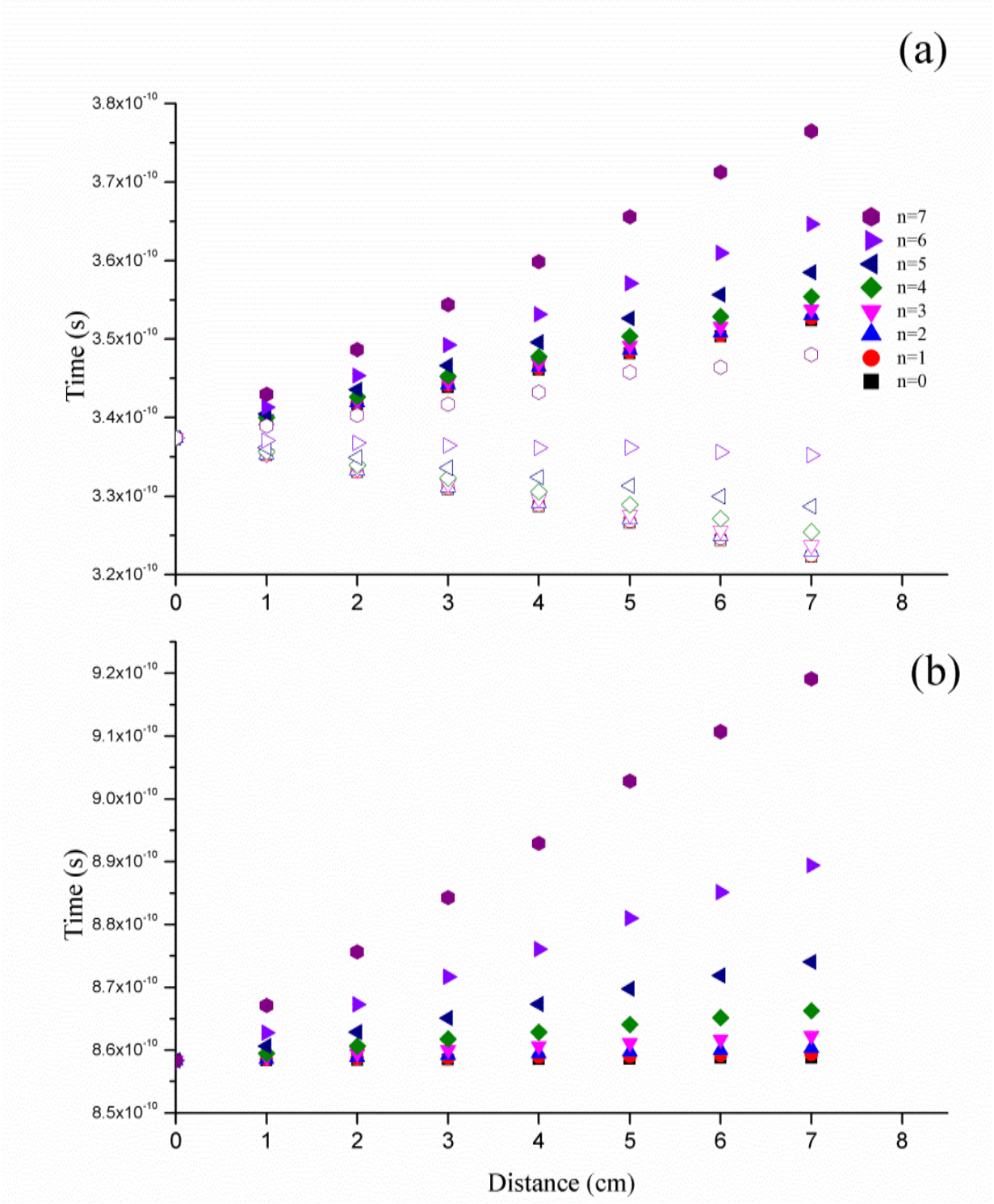

Figure 22: (a) rise time (solid) and fall time (open) and (b) total pulse duration for pulse passing 1 cm increments

3. Materials

3.1 Introduction

Ferroelectric materials are defined as a material with a spontaneous polarization. This polarization is reversible with an applied electric field resulting in a hysteresis loop when the polarization is plotted as a function of electric field [55-59]. Because capacitance is proportional to the dielectric constant which is given by [60, 61]

$$\varepsilon_r = \frac{1}{\varepsilon_0}\frac{\partial P}{\partial E} \tag{72}$$

the shape of the capacitance-voltage (CV) is obtained by plotting the derivative of the hysteresis loop. A typical hysteresis loop and CV curve is shown in Figure 23.

The study of ferroelectric properties dates back to 1921 when Rochelle salt was discovered to behave electrically in a manner that is analogous to the way ferromagnetic

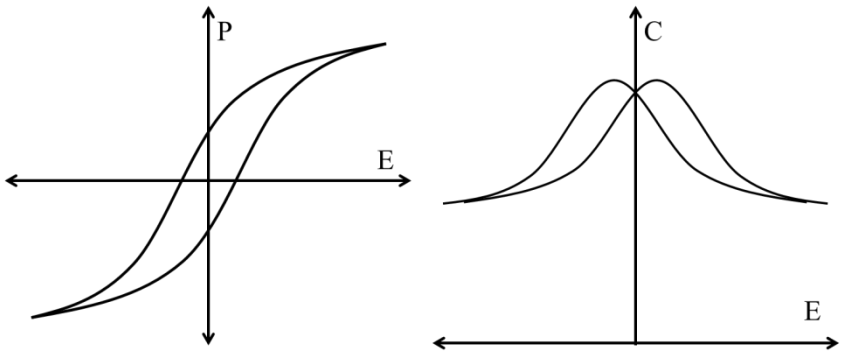

Figure 23: Hysteresis loop and CV curve.

materials behave [62]. In 1930 it was shown by Sawyer and Tower that the dielectric constant of Rochelle salt could be as high as 18,000 when care is taken to ensure quality samples with appropriate electrodes [63]. From the mid 1930's through early 1950's many materials were discovered to be ferroelectric including KH_2PO_4, $BaTiO_3$, $LiNbO_3$, $LiTaO_3$, $PbZr_xTi_{1-x}O_3$, and

$PbNb_2O_6$ [64]. The first ferroelectric thin films appeared in 1970 and the first sol-gel process developed in 1983 [64]. Since then, ferroelectric thin films have been grown by chemical solution deposition [60, 64-74], pulsed laser deposition [60, 64, 75-79], sputtering [60, 64, 80-85], metal organic chemical vapor deposition [60, 64, 86-89], and molecular beam epitaxy [64, 90-95]. These growth methods will be discussed with respect to the growth of barium titanate (BTO), the ferroelectric material of interest for the research discussed in this document.

First, however, an introduction to BTO and its properties will be presented. Next, a short introduction to the characterization techniques of high resolution x-ray diffraction (HR-XRD), x-ray photospectroscopy (XPS), piezoforce response microscopy (PFM), and measurement of the hysteresis loop will provide a foundation for understanding and interpreting results in the analysis sections. Finally, growth results including material quality and performance will be presented for the various growth methods pursued during the course of this work.

3.2 Basic Barium Titanate Properties

BTO is currently a material of great scientific and industrial interest. This interest is due to the performance of the material as a nonlinear dielectric as well as environmental and health concerns that are driving manufacturers to lead free processes [96]. A brief survey of the literature since 2009 shows a focus on the material properties of BTO including phase change dynamics [97, 98], domain properties [99-102], thin film growth [96, 103, 104], and lower dimensional structures [101, 105-109]. Although each of these areas contain interesting information the work presented in this dissertation depends primarily on the dielectric properties of BTO. Therefore, after a brief introduction to the crystal structure the rest of this section will focus on the performance of BTO as a dielectric material.

3.2.1 Crystal structure

BTO is known as an ABO_3 material and is of the perovskite family. It has four phases as a function of temperature, three of which are ferroelectric, and although the changes in lattice spacing are small the effects on the dielectric properties are quite large. Table 7 provides lattice constants for the different phases of BTO [110, 111]. The room temperature, tetragonal, unit cell for BTO is shown in Figure 24 [112]. The ferroelectric behavior of BTO, as well as the other perovskite ferroelectrics, is the result of the Ti^{4+} sitting off center in the unit cell [64].

Table 7: Lattice Parameters of BTO Phases

Phase	a lattice parameter (Angstroms)	c lattice parameter (Angstroms)
Rhombohedral (<180K)	4.00	4.00
Orthorhombic (190K-270K)	3.98	4.02
Tetragonal (280K-350K)	3.99	4.04
Cubic (>350K)	4.01	4.01

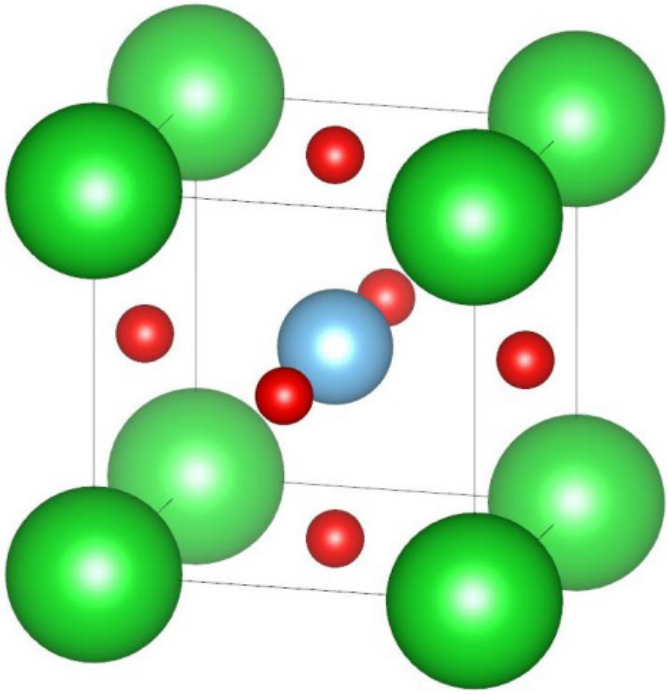

Figure 24: Unit Cell of Tetragonal Phase of BTO [58].

3.2.2 Dielectric Properties

This section presents the dielectric properties of BTO and methods for experimentally measuring such properties. Then examples from the literature of the polarization versus electric field hysteresis, capacitance-voltage (CV) relationship, loss tangent, and dielectric dispersion are all presented. A later section will discuss material grown specifically for this effort.

3.2.2.1 Hysteresis and CV

The typical hysteresis curve shown in Figure 23 is not specific to BTO and can be generalized to all ferroelectric materials. Parameters of interest on such a curve include the positive and negative remnant polarization, $P_{r_\pm}$; the positive and negative coercive field, $E_{c_\pm}$; and the positive and negative spontaneous polarization, $P_{s_\pm}$. Ideally, the hysteresis loop is symmetric so that $P_{r_+} = -P_{r_-}$, $E_{c_+} = -E_{c_-}$, and $P_{s_+} = -P_{s_-}$ [56, 59, 113]. Deviation from such

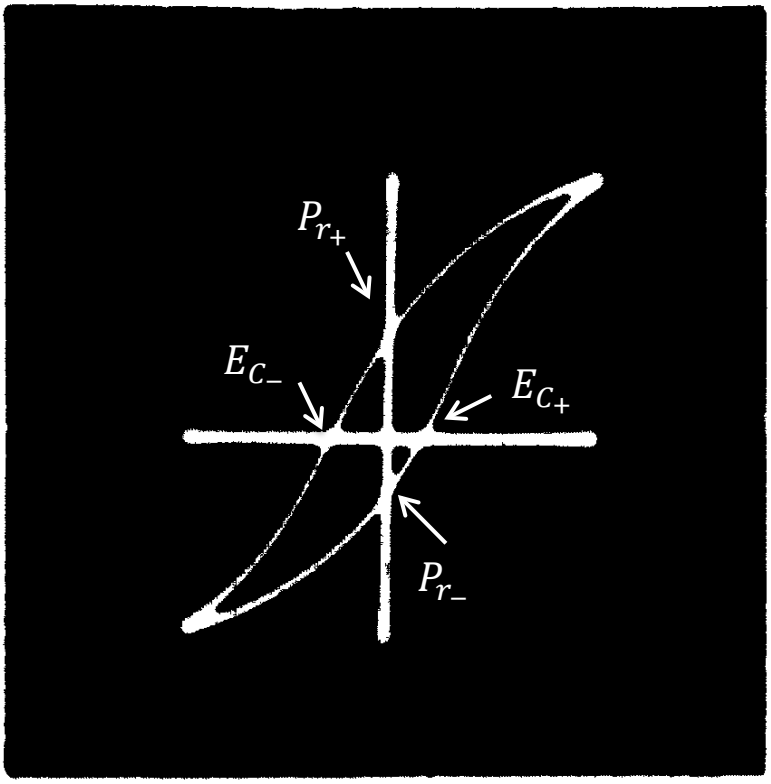

Figure 25: Measured Hysteresis Loop [59] (labels added by author).

symmetry can be caused by strain, defects, method of growth, and film thickness [59, 113]. An example of a measured hysteresis loop for BTO is shown in Figure 25 [114].

Four types of hysteresis measurement techniques, shown in Figure 26, are briefly discussed here. As part of their work Sawyer and Tower developed a circuit, shown in Figure 26(a), which was essentially a capacitor based voltage divider, to plot a hysteresis curve on an oscilloscope [64]. The circuit operated on the principle that the charge on two capacitors in series is equal. Therefore, because $Q = CV$, the voltage between the capacitors is a linear function of the surface charge on the ferroelectric devices. A circuit, Figure 26(b), capable of testing leaky ferroelectric samples was published in 1956. This circuit used a bridge with a compensating resistor [115]. Then, in 1968 Tsui, Hinderaker, and McFadden developed a circuit, Figure 26(c), to eliminate the restrictions on oscilloscope impedance and provided both compensated and uncompensated measurements at the same time. This scheme used operational amplifiers to create virtual grounds and a compensation circuit [116]. This device still operated on the principle of comparing a known capacitor to a device under test. A more recent development, which exploited impedance matched pickoff tees as shown in Figure 26(d), was capable of measurements at frequencies as high as several gigahertz [117]. This measurement used the rise-time of voltage on the test capacitor to determine the capacitance, from which the hysteresis loop could be determined.

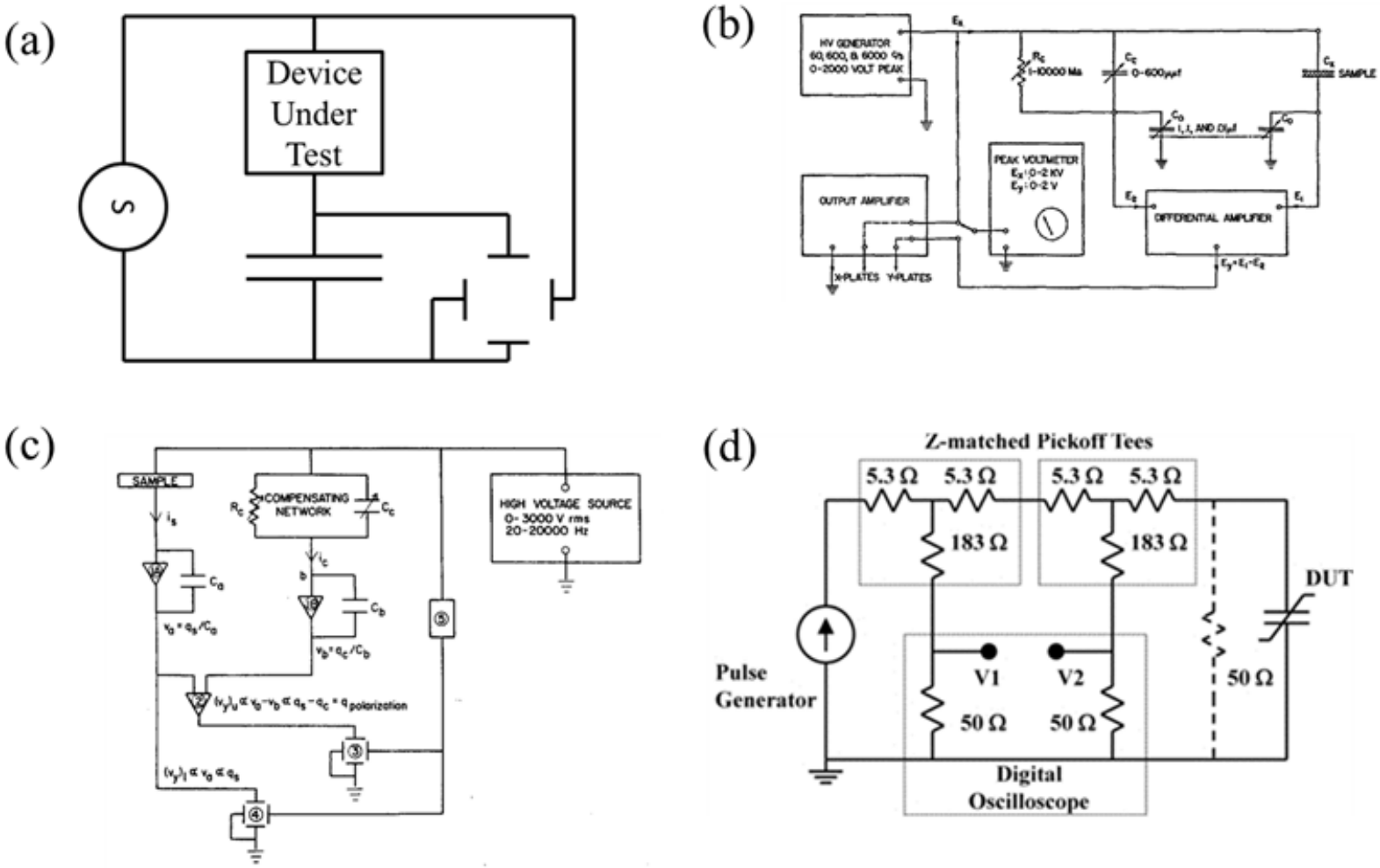

Figure 26: Common devices used to measure hysteresis loops. The devices are (a) a Sawyer-Tower circuit [64], (b) a compensating bridge [115], (c) an operational amplifier based charge converter with compensation [116], and (c) a high frequency pickoff tee based design [117].

The relationship between the CV curve and the hysteresis loop has already been established through Equation 72. Figure 27 shows an experimentally generated CV curve for a sol-gel BTO capacitor with a Ni bottom electrode and Pt top electrodes [71]. Since the capacitance of a sample is linearly dependent on the dielectric constant, the CV curve can be interpreted as a measure of the dielectric constant. In addition to frequency dependence, which will be discussed in the dispersion and loss tangent section, the dielectric constant of a given ferroelectric material may depend on temperature [56, 59, 118], growth quality [59, 118], and strain [93]. The ferroelectric measurements reported in this dissertation were made using a Radient Premier II ferroelectric tester.

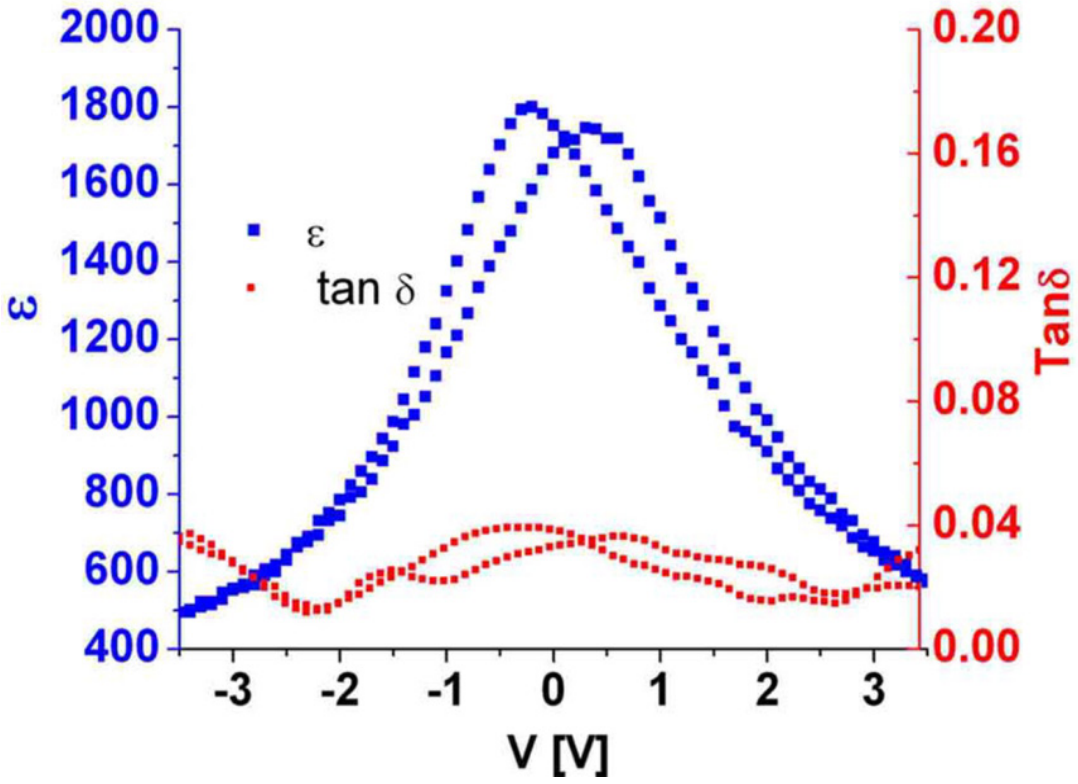

Figure 27: Experimentally obtained CV curve and loss tangent for sol-gel BTO capacitor with Ni bottom electrode and Pt top electrode [71].

3.2.2.2 Dispersion and Loss Tangent

The dispersion of a material is the tendency of waves of different frequencies to propagate at different rates. Dispersion is a result of the dielectric constant varying as a function of frequency. Since the frequency components of a signal can be established using a Fourier transform, the effect of dispersion on that signal can be predicted. The frequency dependence of BSTs dielectric constant is shown in Figure 28 [119].

The loss tangent of a material depends on the complex dielectric constant, $\varepsilon = \varepsilon' - i\varepsilon''$, of that material. Specifically, it is defined as $\tan\delta = \frac{\varepsilon''}{\varepsilon'}$ [120] which allows the dielectric power losses in the capacitor to be written as $P_{loss} = V^2\omega C \tan\delta$. Since the loss tangent is a function of the complex dielectric constant it is a function of everything the dielectric constant depends on including temperature, frequency, and bias voltage. The higher the loss tangent the higher the dielectric loss.

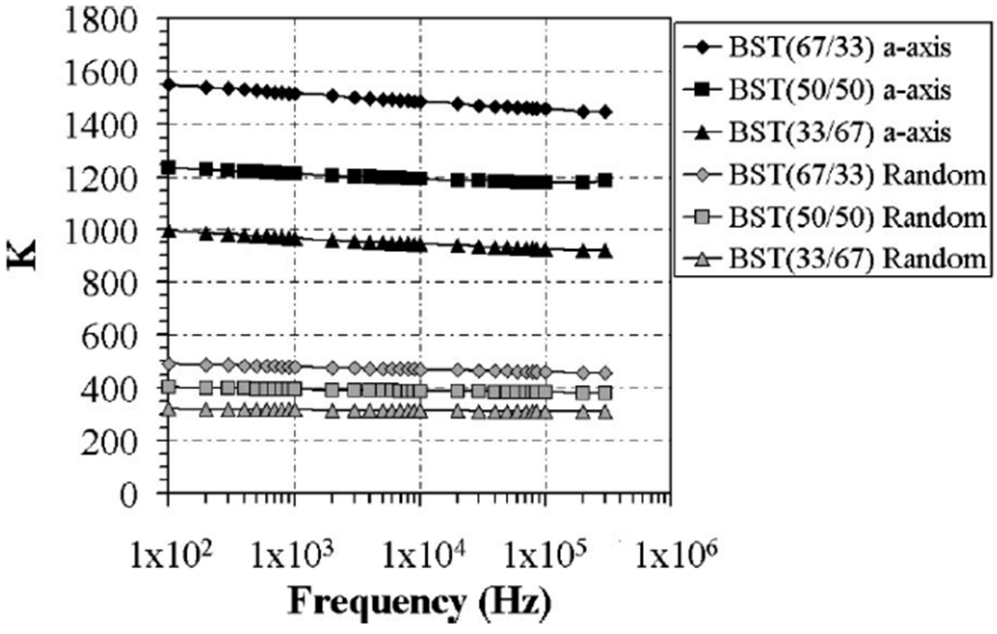

Figure 28: Frequency dependence of dielectric constant for BST [66].

3.3 Background of Growth of Barium Titanate Thin Films

There are many methods of growing BTO thin films including MBE, PLD, RF-magnetron sputtering and sol-gel. Each method has advantages and disadvantages. Each method is briefly discussed with the advantages and disadvantages being highlighted. The growth methods specifically attempted for this research were MBE and sol-gel.

3.3.1 MBE

Early efforts to grow thin films by an MBE process failed due to an inability to control stoichiometry [121]. Then in 1968 Arthur successfully grew GaAs by MBE as a byproduct of studying Ga and As lifetimes and sticking coefficients at a GaAs surface [121, 122]. Since then, MBE has been primarily developed for compound semiconductor material growth [121, 123, 124]. A major advantage of MBE growth is the capability to produce high quality single crystal thin films over an entire substrate [121]. The control of layer thickness, ability to control dopants, and purity of material is unsurpassed by other growth methods. Furthermore, because MBE is an ultra-high vacuum (UHV) system it is compatible with the use of reflective high energy electron diffraction (RHEED). Unfortunately, MBE growth has many disadvantages. These disadvantages include the slow growth rate [121], difficulties in growing ternary materials stoichiometricly [125-127], and expensive ultra-high vacuum (UHV) systems. This section describes the processes of growth by MBE and provides an overview of three methods used to grow ternary materials.

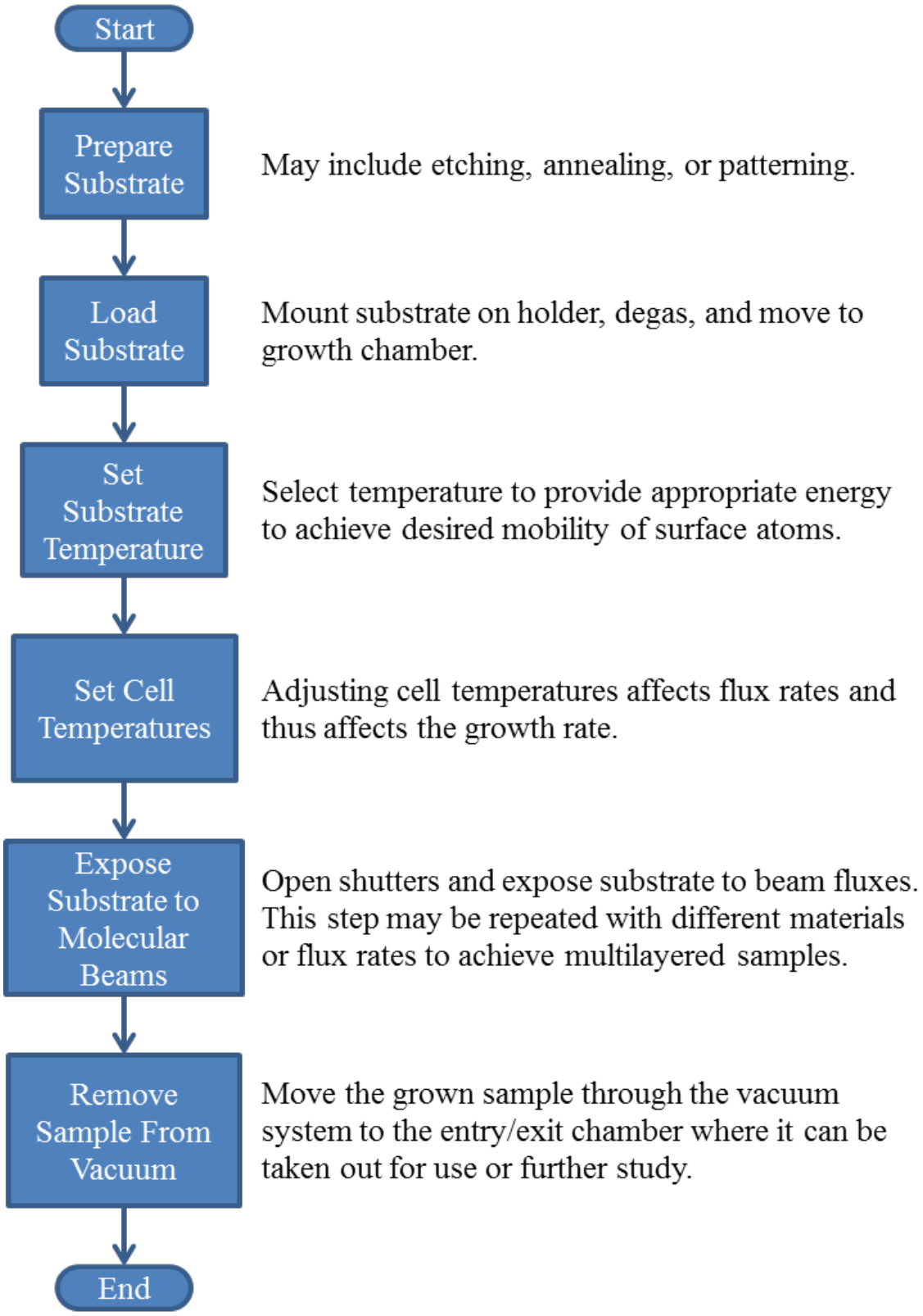

Figure 29: MBE growth flowchart

3.3.1.1 Basic Process

The general MBE growth process, illustrated by the flow chart in Figure 29, occurs in a UHV reactor chamber. The MBE reactor chamber contains four main elements [121, 123]: the entry (exit), the wafer transportation, growth system, and the substrate manipulator. Additional components include a RHEED for insitu characterization [121, 123, 128, 129], temperature measurement tools, or flux measurement gauges.

A diagram of the oxide MBE reactor at the University of Arkansas is shown in Figure 30. This chamber contains barium, strontium, and titanium cells along with an Addon plasma for oxygen. Furthermore, a RHEED system provides insitu growth characterization and a BandiT system for band gap measurement system provides capability for measuring the substrate temperature of a limited selection of substrates using the band edge, and for measuring any substrate with a metal coating through blackbody radiation. Plans for additional chamber features include a quartz crystal microbalance for flux calibration, but this feature was not successfully implemented during these studies.

During the deposition process the effusion cells are heated to increase the vapor pressure of the source material. When the shutter blocking the effusion cell is opened a molecular beam is allowed to enter the chamber. When the chamber pressure is sufficiently low the atoms in the beam typically traverse the distance between the effusion cell and the substrate without collision. Upon collision with the substrate surface a certain number of atoms in the molecular beam stick. Those that do not stick to the surface, along with those that desorb, are trapped by cryopanels or pumped out. The substrate is held at an elevated temperature such that the atoms remaining on the surface have the energy, and thus the mobility, to migrate to a proper lattice location. Layer by layer, the crystal is grown. Because of the slow epitaxial growth high quality semiconductor

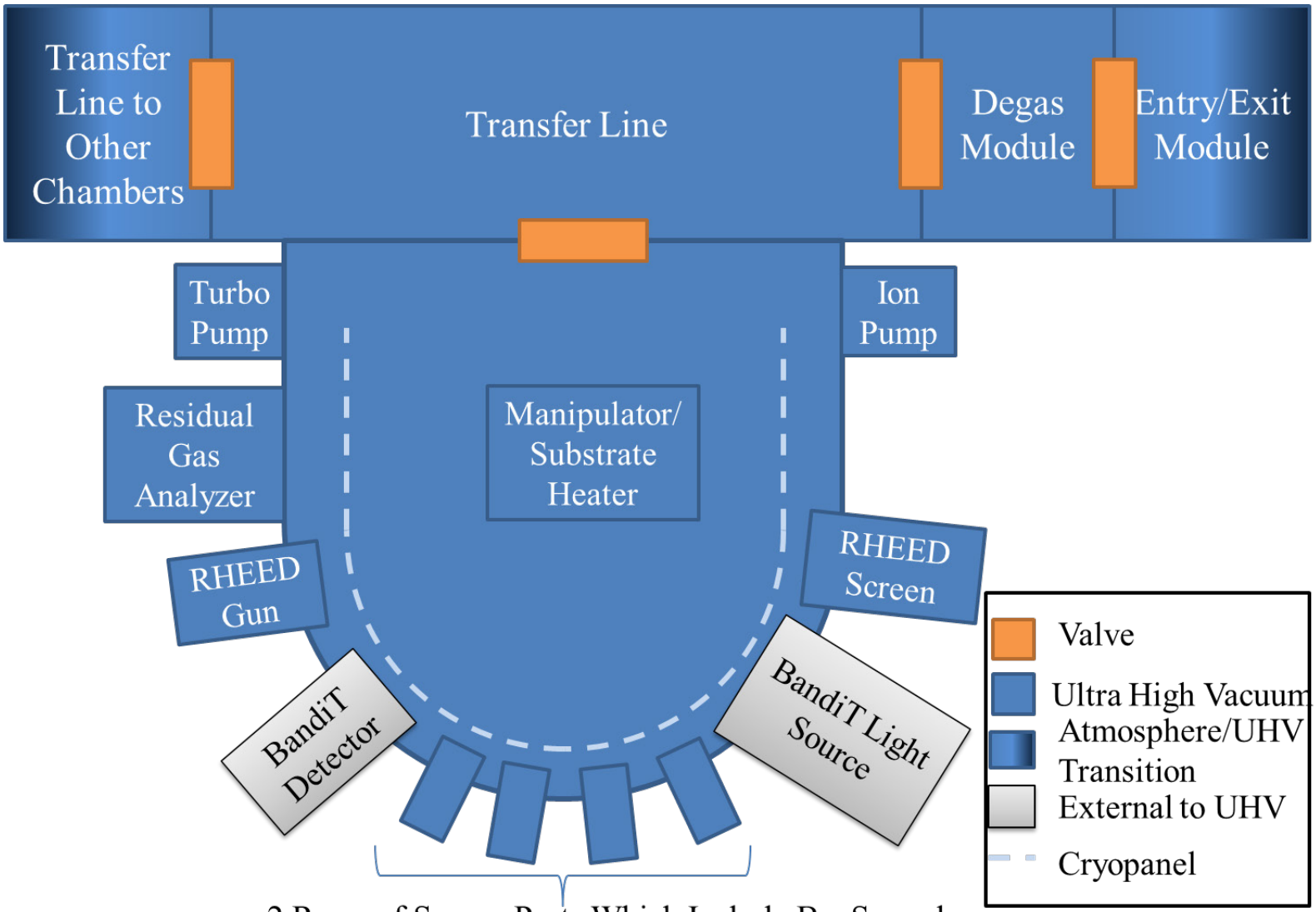

Figure 30: Oxide Molecular Beam Epitaxy Reactor

crystals with arbitrary doping profiles, including near delta doping, are achievable [121, 123, 128, 129]. For many materials there is some range of flux ratios that will result in good growth. For example, the ratio of indium to nitrogen in the growth of InN changes the growth structure but not the material stoichiometry [130]. Growth of BTO requires sufficient oxygen which is provided in abundance using an ozone source [131] or plasma [132, 133]. Maintaining the proper ratio of barium and titanium is critical however. Therefore, careful calibration of the fluxes must be maintained throughout a growth. Two methods based on RHEED have been used to achieve growth of ternary materials with proper stoichiometry. After providing a background on RHEED both the shuttered RHEED growth method and the codeposition using the RHEED reconstruction [126] signal as feedback will be discussed. Additionally, a method relying on electron impact emission [125] will be presented.

3.3.1.2 RHEED introduction

Like a transmission electron microscope, a RHEED system uses electrons to probe a material. Instead of pushing electrons through the material however, a RHEED system bounces them off the sample at a shallow angle as shown in Figure 31. The electrons diffract off the surface of the crystal and are collected by a phosphor coated window resulting in a diffraction pattern that is related to the reciprocal lattice of the material [134], the condition of the surface

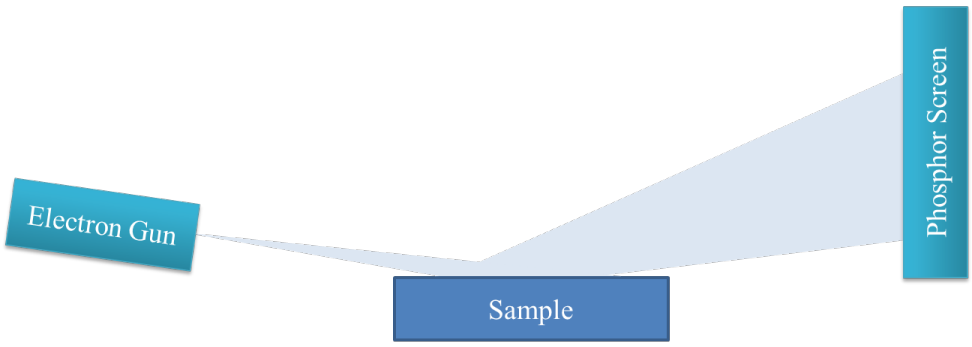

Figure 31: RHEED System

[134], and the atoms that construct that surface [127]. For example, the spacing of the features in the diffraction pattern are related the reciprocal lattice. Additionally, an atomically rough surface has a dimmer and more diffuse diffraction pattern than an atomically smooth surface made of the same material. Finally, some materials reflect better and thus have a brighter diffraction pattern. Using this information, two techniques, shuttered RHEED and RHEED reconstruction feedback, have been developed to ensure proper stoichiometry throughout the growth process of BTO.

3.3.1.3 Shuttered RHEED growth

This growth method ensures stoichiometry by growing single monolayers of barium oxide alternated with single monolayers of titanium dioxide. This is possible because the diffraction pattern of the barium oxide layer is brighter than the diffraction pattern of the titanium dioxide layer [127]. So, starting with a titanium dioxide terminated surface, the barium shutter is opened and a layer of barium oxide begins to grow on the surface. As this layer grows, the RHEED signal increases in intensity to some maximum. At the maximum intensity a full monolayer of barium oxide has been deposited and the shutter should be closed. If a second layer were allowed to form the atomic roughness would increase and the RHEED signal would diminish. Next, the titanium shutter is opened and the next titanium dioxide layer is grown

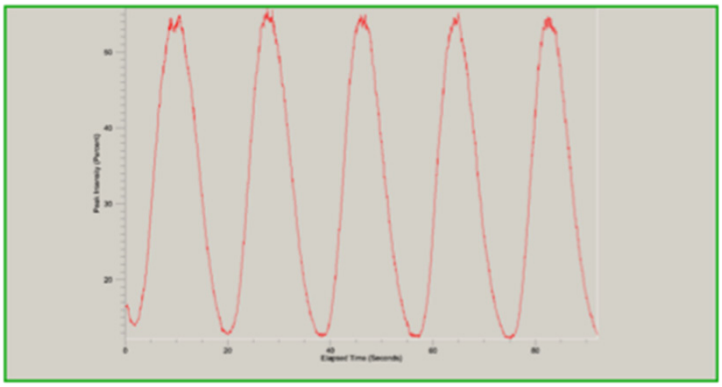

Figure 32: RHEED signal intensity for 5 unit cells of shuttered RHEED growth.

reducing the RHEED signal to some minimum at which time the titanium shutter is closed. This two stage process produces a film that is a single unit cell thick but can be repeated to achieve arbitrary thicknesses [127, 132, 133, 135]. The RHEED signal versus time for a 5 unit cells of BTO film grown by this method is shown in Figure 32.

3.3.1.4 RHEED reconstruction feedback growth

This method has been successfully used to grow STO on silicon. The key to this method is that a strontium oxide terminated surface has a different RHEED pattern than a titanium dioxide surface. Feedback is achieved by observing the deviation of the RHEED signal from an appropriate balance and compensating by adjusting the flux ratios. Growth by this method is slow, occurring at approximately 0.2nm/minute [126].

3.3.1.5 Electron Impact Emission feedback growth

A final method of maintaining proper flux ratios for ternary material growth was developed by Naito, Yamamoto, and Sato who used electron impact emission (EIE) spectroscopy to control the deposition rates of both strontium and titanium to approximately 100fm/s [125]. First developed by C. Lu to control deposition rates, EIE exposes the atomic beam to an orthogonal electron beam. The interaction between the atomic beam and the electron beam imparts some energy to the outer shell electrons of the atomic beam. When these electrons relax back to their ground state they emit a photon that can be collected and used to characterize the atomic species [136]. Once the atomic species in the beam are identified a feedback loop can be created to maintain the proper flux ratios in atomic beam. The RHEED oscillations of STO grown on STO using this method showed good epitaxial growth for at least 98 monolayers at a rate of 0.3 monolayers per second [125]. Atomic force microscopy was also used to show that

when growth was terminated at a partial layer 0.4nm terraces or hollows, which correspond to the height of a single unit cell, exist on the surface [125].

3.3.1.6 Available Substrates

Because MBE growth requires lattice matched substrates capable of withstanding the growth temperatures there are a very limited number of possibilities. Several substrates which are suitable for BTO growth by MBE are identified in Table 8 [93, 137-139] along with their lattice parameter and the percent mismatch with the BTO lattice. These substrates work because they have sufficient lattice match, do not react chemically to film being deposited, can be sufficiently polished, and have similar thermal expansion rates to the thin film [140].

Table 8: Lattice parameters for various substrates used for growth of BTO by MBE

Substrate	Lattice Parameter (Å)	Percent Mismatch (%)
$BaTiO_3$	3.99	0.0
$GdScO_3$	(pseudo) 3.97	0.5
$DyScO_3$	(pseudo) 3.94	1.3
MgO	4.21	-5.2
$SrTiO_3$	3.90	2.3
$LaAlO_3$	(pseudo) 3.79	5.3
$(LaAlO_3)_{0.3}(Sr_2AlTaO_6)_{0.7}$	(pseudo) 3.87	3.1

3.3.2 PLD

Pulsed laser deposition (PLD), sometimes referred to as laser MBE, uses short high power laser pulses to ablate material from a target in a vacuum system. When the material is ablated it creates a plume which is directed at a substrate. The material from the plume that strikes and sticks to the surface forms the new crystal growth [141]. A diagram for a typical PLD system is shown in Figure 33 [139]. A major advantage of PLD growth is that the material is being deposited is from a high purity target. Therefore, the stoichiometry of the material may not be an issue [142]. Difficulties in growing high quality multicomponent thin films by PLD

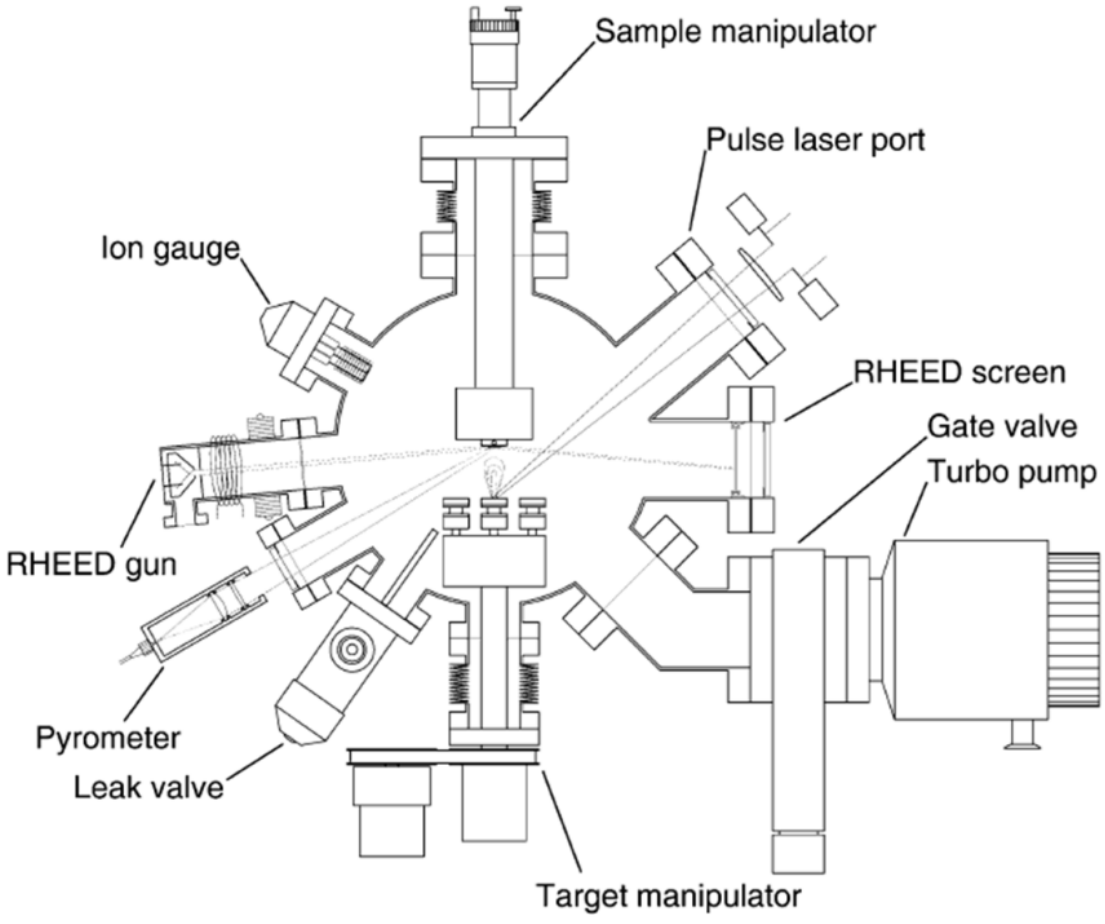

Figure 33: Typical PLD system [139]

include growth uniformity, subsurface implantation of high energy species, micron sized particles resulting from ablation, and nonometer sized particles forming during plume transit [143]. Since the growths are done at substrate temperatures in approximately the same window as the growths in MBE the substrates that have been used in MBE for BTO growth are the same are the same as the substrates that have been used in PLD growth of BTO [93, 140].

3.3.3 RF-Sputtering

RF-sputtering, Figure 34 [139], is similar to PLD in that it uses a stoichiometricly correct target. Instead of a laser, however, this technique uses ions accelerated towards the target by an electric field. When the ions strike the target they create a discharge of material from the target.

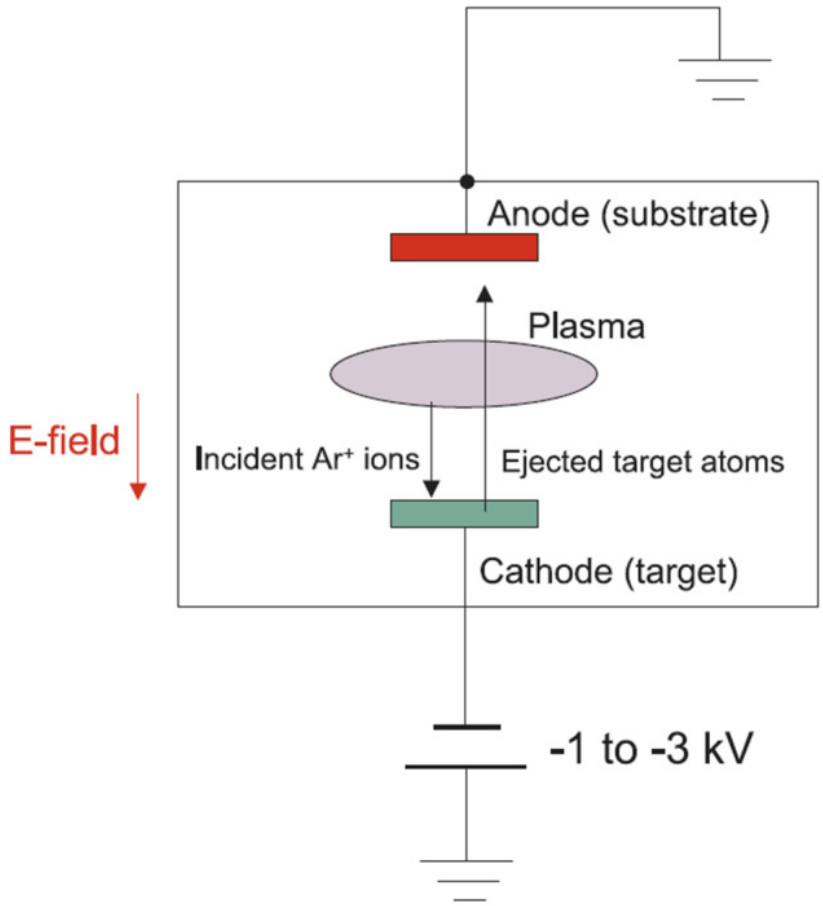

Figure 34: Schematic of RF sputtering system [139].

Some of this discharged material collects on the substrate where it grows as a thin film on the surface [144]. If the materials being grown are insulating, charge will build up, the field will be compensated, and the sputtering will diminish [144, 145]. An RF signal can be used to discharge the static build up during a portion of the cycle while bombarding the target with ions during the other portion of the cycle [146]. Although there are several choices of gas available for ionization, argon (or argon mixed with another gas) is often used [85, 146, 147]. Again, the substrate requirements for single crystal thin film growth are similar to the requirements for MBE so the available substrates are the same [140, 148]. Polycrystalline thin films have been successfully grown on platinum substrates however [146, 149].

3.3.4 Sol-Gel

The sol-gel process is a wet chemical deposition method during which a solution of small particles in a liquid is reduced to the point that the individual particles converge to form a gel [150]. The gel is a mostly liquid material that behaves as a solid because of a cross-linked network of particles. The solution can be reduced to a gel through a reaction that causes a gel to condense, by aging the solution in ambient conditions, or by applying heat [151]. The basic sol-gel process is illustrated in Figure 35.

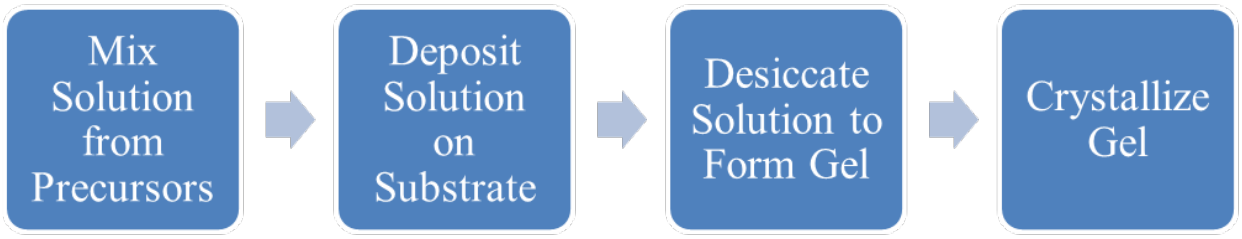

Figure 35: Basic Sol-gel Process

3.3.4.1 Available Substrates

Although it is possible to grow material epitaxially with the sol-gel process [72], it is often used for deposition on metal or other substrates [66, 67, 71, 152-154]. Under such a condition the grown material is polycrystalline [66, 153]. Metal substrates used for sol-gel growth include platinum [154] and nickel [66, 67, 71].

3.3.4.2 Previous Sol-Gel BTO Deposition

Many groups have successfully deposited BTO by the sol-gel process. Primarily, the recipes are similar in that they call for some form of barium and some form of titanium to be mixed with chemicals to form precursors. Next these precursors are combined, often with the addition of another chemical, to form the sol. Using this basic form, many variations exist. For example, one recipe uses barium 2-ethyl hexanoate as a precursor [54]. Another recipe, for barium strontium titanate, calls for barium acetate and strontium acetate to be dissolved in acetic acid before the addition of ethylene glycol [72]. In a final example, barium acetate was dissolved in acetic acid before being diluted with 2-methoxyethanol. Finally, a measured amount of titanium (IV) isopropoxide was added to form the sol [74].

3.4 Analytical Techniques

In addition to electrical characterization three analytical techniques were used in this work to analyze BTO thin films. x-ray diffraction (XRD) provided information concerning film quality and crystalinity, x-ray photoelectron spectroscopy (XPS) provided information concerning film composition, and atomic force microscopy (AFM) provided information concerning surface morphology, piezo response, and conductivity.

3.4.1 X-ray Diffraction

One method of verifying a crystals structure is to use XRD. To do this, a collimated x-rays is directed at some angle towards the crystal. The x-rays scatter spectrally off the atoms in the crystal. At some angles, given by Bragg's Law, Equation 73, the x-rays interfere constructively. In Bragg's law, d is the atomic spacing, λ is the wavelength of the x-ray, θ is the angle of incidence/reflection. The variable n is the order and indicates if the interfering reflections are from nearest neighbors ($n = 1$), next nearest neighbors ($n = 2$), … Figure 36 shows a schematic of this measurement.

$$n\lambda = 2d \sin\theta \tag{73}$$

Table 9 provides the angles and plane spacing for high resolution X-ray diffraction (HRXRD) of the tetragonal (room temperature) phase of BTO when using a Cu $K\alpha_1$ source (0.154 nm wavelength). Factors including strain and defects can change the atomic spacing and thus affect the position and breadth of the peaks.

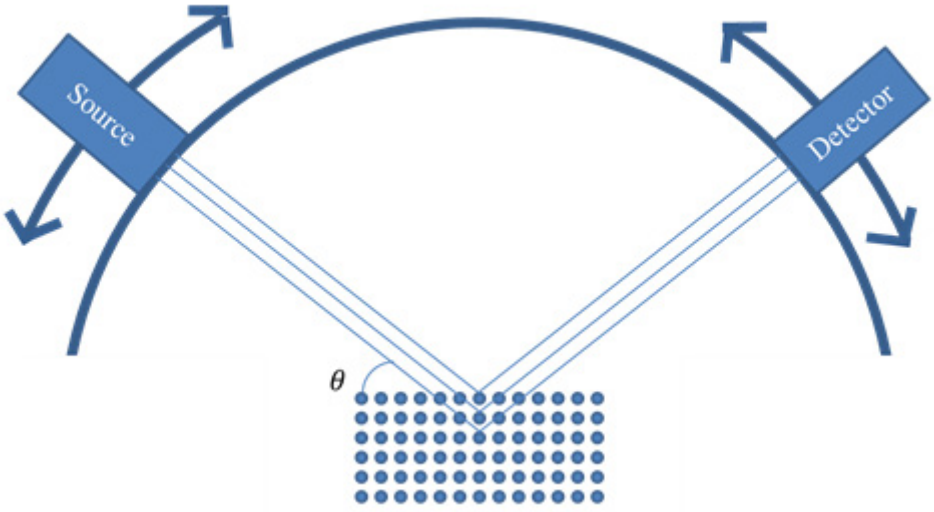

Figure 36: Illustration of XRD measurement showing x-ray source, detector, collimated beams, and crystal lattice.

Table 9: Peak positions for selected lattice planes

h	k	l	Theta (°)	2Theta (°)	d(Å)
0	0	1	10.99151	21.983029	4.04
0	0	2	22.41592	44.831837	2.02
0	0	3	34.88917	69.778340	1.35
0	0	4	49.69877	99.397542	1.01

3.4.2 X-ray Photoelectron Spectroscopy

The power of X-ray photoelectron spectroscopy (XPS) is the ability to identify the chemical environment of atomic species in a sample. The technique uses the photoelectric effect to generate electrons from the sample using X-rays. The energies of the emitted electrons are determined using a spherical capacitive analyzer which is electrically connected to the sample to link the Fermi energies. Because the energy of an ejected electron is related to the energy level the electron started at, by examining the energies of these ejected electrons the atomic species can be determined. Because the chemical environment shifts the electron level of an atom the binding energy changes. Thus the chemical environment may be determined by comparing results with known references. The energy levels in the XPS process are visually depicted in Figure 37. Note that the work function of the detector must be established in order to correctly

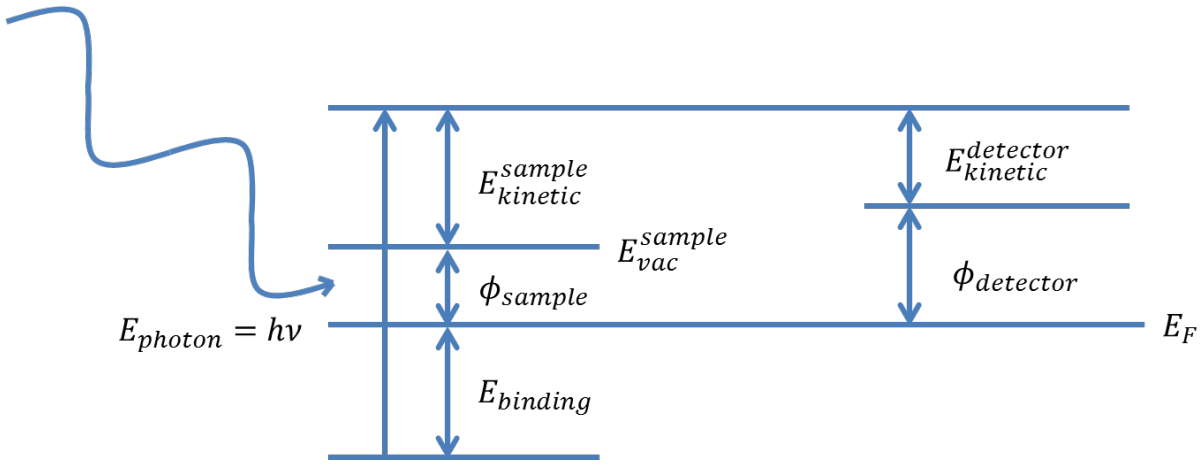

Figure 37: XPS energy level diagram

quantify the binding energy of the electron in the sample.

By examining the areas under the peaks it is possible to determine relative concentrations. Determining the correct peak intensity is complicated by the background subtraction process [155, 156]. Once the peaks have been adjusted for the background the fractional composition of each element in the sample can be determined by using Equation 74 where I_x is the intensity of a given peak and S_x is the sensitivity factor for that peak.

$$C_x = \frac{\frac{I_x}{S_x}}{\sum \frac{I_i}{S_i}} \tag{74}$$

One study which involved several different laboratories examining the same materials found that the uncertainty of compositional analysis was $\pm 2.43\%$ [156].

3.4.3 Atomic Force Microscopy (AFM)

The tool of choice when it comes to determining surface morphology of insulating samples is the AFM. The instrument creates a three dimensional image of the surface by rastering an atomically sharp probe across the surface. The probe is attached to a cantilever which has a laser reflected off the back surface. When the probe is oscillating so that the probe-surface interaction changes the amplitude and phase of the oscillation, the microscope is said to be in tapping mode. When the probe is not oscillated and the probe-surface interaction changes the angle of the cantilever with respect to the reflected beam, the microscope is said to be in contact mode. In both modes, a split optical detector is used to detect changes in the probe-surface interaction. A proportional integral controller then provides a voltage to a piezo tube which adjusts the height of the base of the cantilever to maintain a constant probe-surface interaction. The voltage applied to the piezo tube is plotted and recorded as the probe is rastered

by the controller. If the piezo response of the tube is known the voltages may be converted to units of distance. A block diagram of an AFM is shown in Figure 38.

In addition to topography, an AFM can be used to make many other measurements. Of specific interest to this work is the the piezoresponse. Characterizing the piezoresponce of a sample was important in this work because a ferroelectric material must also be piezoelectric. In piezo force response microscopy (PFM) a conductive probe, in contact mode, is used to apply an AC signal to the sample. If the material is piezoelectric it will expand and contract at the same frequency as the applied AC signal. This changes the angle of the cantilever with respect to the laser beam very slightly. A lock-in amplifier is then used to measure the response of the laser signal oscillating on the photodector at the frequency of the applied AC signal. Typically, both the magnitude and the phase of the piezoresponse are collected because the magnitude is related

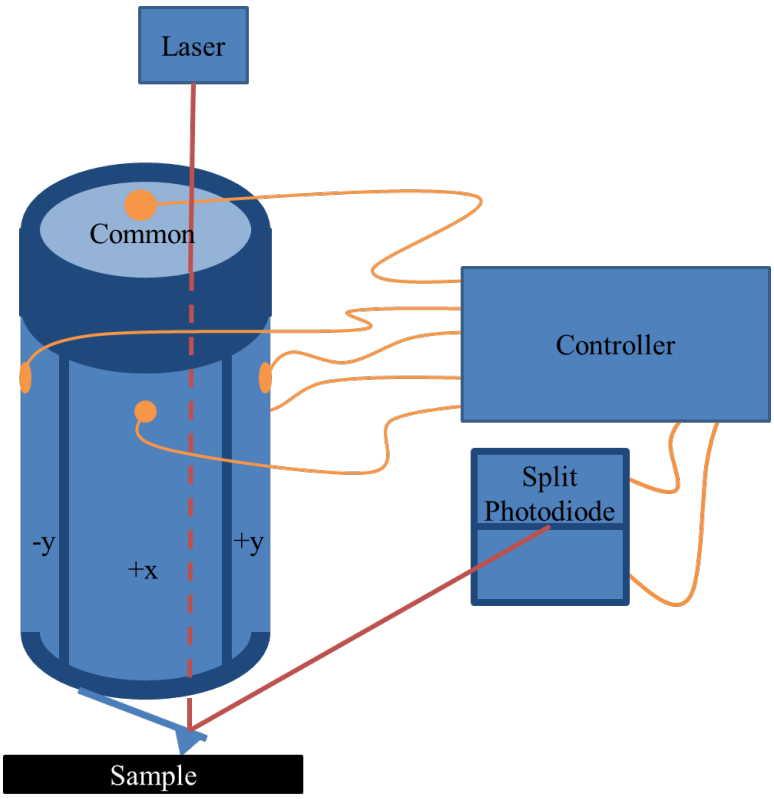

Figure 38: Block diagram of AFM

to the strength of the piezorepsonce and the phase is related to the direction. Often, however, only one image consisting of the magnitude times the phase is shown. A block diagram of this measurement is shown in Figure 39.

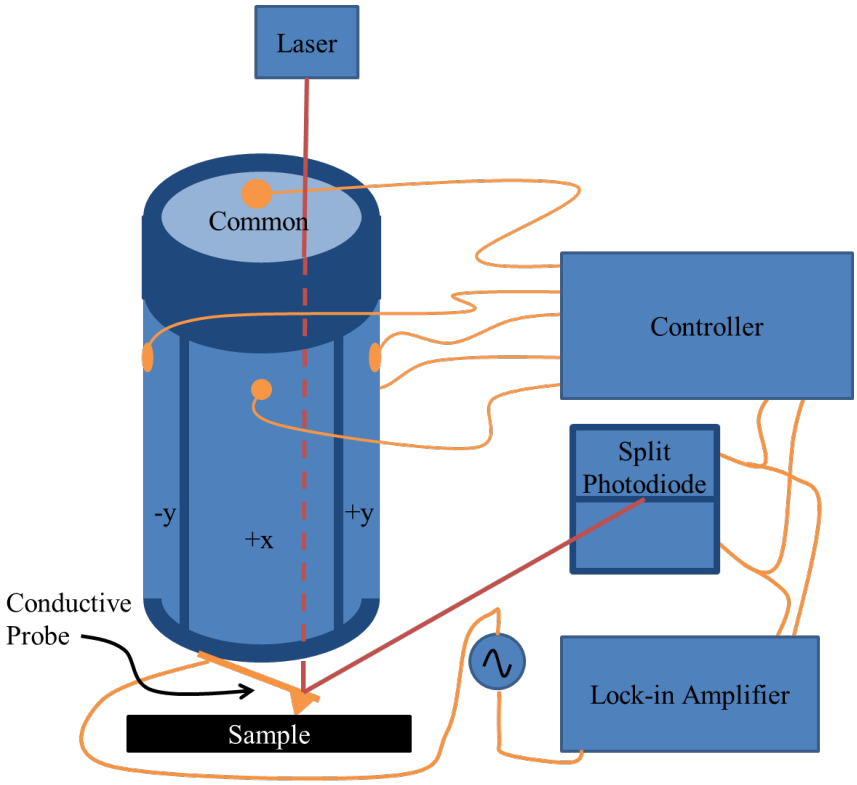

Figure 39: Block diagram of AFM including piezoresponce measurement.

3.5 Growth Approach in this Dissertation and Results

Two growth methods were used in the course of this research. The first method was MBE and the second method was sol-gel. Initially MBE was chosen as the growth method, however, chamber performance and equipment relocation led to a decision to develop sol-gel growth in parallel with the MBE efforts. The growth plans, growths, and growth results are presented in this section.

3.5.1 MBE

The initial proposal for the research presented in this dissertation called for MBE growth of BTO on LiF. After a few initial attempts, BTO was successfully grown on freshly cleaved LiF. The growth was confirmed with both RHEED and XRD. Unfortunately, before additional growths could be completed the chamber performance degraded. Because much of the effort during this period was focused on attempting to grow material with properties that could be improved upon only rapid qualitative measurements were used. These measurements were primarily film resistance as measured by a standard digital multi-meter using two probes and film color by naked eye. Occasionally, the films were also tested for their peizoresponce or their ferroelectric properties.

3.5.1.1 Discolored

Colored films were an indication that sample quality was a problem. When a growth produced a colored film it was assumed that some dopant had contaminated the sample. Films produced during this period ranged in hue from blue to blue green with some non-quantified variation in saturation. The two factors believed to contribute to the film color were undesired dopants and oxygen vacancies. Potential dopant sources include a screw on one of the plasma sources that was heating due to a grounding problem and the substrate heater breaking down. The oxygen vacancy issue appears to be due to non-optimal use of the plasma source. After dealing with both potential dopant sources and increasing the amount of reactive oxygen the sample clarity appeared to improve dramatically.

3.5.1.2 Resistance

When sample quality was suspect, the first electrical measurement made was typically a resistance measurement. Such a measurement consisted of touching the top surface of the sample

with probes connected to a digital multimeter. Because contact area and probe separation were not controlled, these measurements did not provide an absolute measurement of the sample's resistance. They did, however, indicate whether the sample was insulating or not. All samples that showed discoloration were not insulating. Again, after removing the potential dopant sources and improving the oxidation, the resistance of the sample increased dramatically.

3.5.1.3 No piezoresponse

At least one of the earliest samples grown on Nb:STO by MBE showed a strong piezoresponse as measured by PFM after polling a 1um area in the center of a 5um scan. This measurement is shown in Figure 40 where the left panel shows the topography and the right panel shows the piezoresponse. Once the performance of the chamber degraded samples stopped having a significant piezoresponse. On a couple of occasions the later samples did show some response that was detectable just above the noise level.

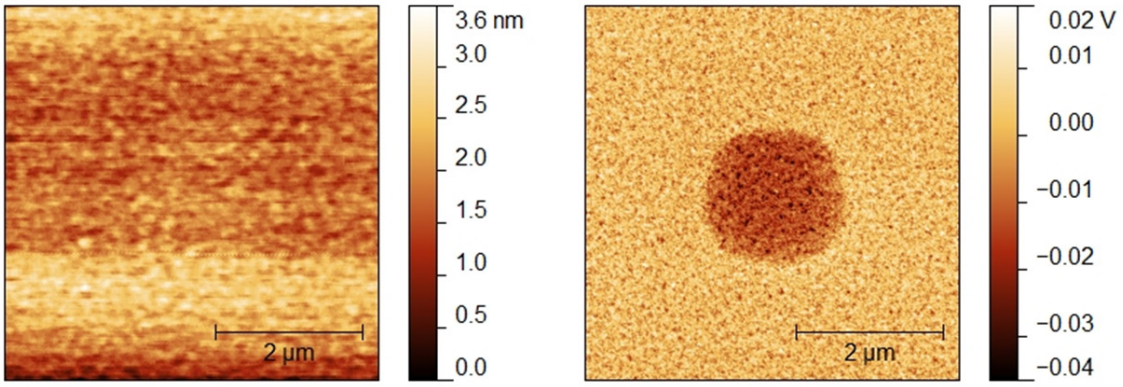

Figure 40: Topography and piezoresponse of early MBE grown BTO showing polled area in the center of a 5um scan.

3.5.1.4 No Nonlinear Behavior

Regardless of any other observations or measurements made, any sample must demonstrate nonlinearity in the capacitance versus voltage measurement to be usable in this

research. Relatively low field (up to $4\,\frac{kV}{cm}$) measurements were made using interdigital devices when the samples were grown on insulating substrates. When the samples were grown on conductive substrates, however, much higher maximum fields (approximately $1000\,\frac{kV}{cm}$) were applied. In both cases, smaller fields were used initially to ensure no damage to the sample. The fields were then incrementally increased with the hope that a sample might appear to be linear at low fields but show a nonlinearity of at least 10% at higher fields. At the time of writing, no sample from the Oxide MBE chamber has demonstrated such nonlinearity.

3.5.2 Sol-gel

Since the MBE chamber was not producing viable samples it was decided to pursue additional growth methods in parallel to continuing the MBE effort. The sol-gel process went through many incremental improvements throughout the course of this research. At times the growths produced samples with promising properties. Often the success was intermittent however. This section presents the recipe as originally implemented and discusses the challenges discovered in producing viable samples before identifying specific recipe modifications. Finally, results of both the less successful growths and the more successful growths are presented.

3.5.2.1 Recipe

The recipe used to grow BTO by sol-gel for this research was based on work from a research group at Pennsylvania State University [66, 67, 71]. The major drawback of this recipe was that it used a nickel substrate that was susceptible to oxidation. This meant that precise control of both oxygen partial pressure and temperature was required during annealing to ensure that the BTO was fully oxidized without oxidizing the nickel substrate. The original recipe used a reducing furnace system to achieve these strict requirements [66]. To avoid the need for such

precise control, the substrate was changed. A variety of substrates were used including STO, Nb:STO, and platinum coated Nb:STO. A flow chart of the initial growth recipe used in this research is shown in Figure 41. There were two precursors. One consisted of $1.2771g$ barium acetate and $6ml$ of acetic acid mixed for two hours in a dry nitrogen atmosphere. The second was $1.516ml$ of titanium isopropoxide mixed with $1ml$ acetyl acetone mixed in a dry nitrogen atmosphere. The two precursors were combined and $3ml$ of acetic acid was added to the solution which was stirred for 12 hours in a dry nitrogen environment. Finally, $1.6ml$ of 2-methoxyethanol was stirred into the solution in order to stabilize it [71]. The solution was spun onto the substrates at 3,000 rotations per minute and pyrolized on a 220C hotplate for 7 minutes. Two layers were spun onto the substrate before the film was crystalized at 800C for 60 seconds using a rapid thermal annealer. The spinning process was then repeated again until a total of 8 layers, or about $330nm$, was deposited. Finally, the sample was oxidized at 600C in an oxygen atmosphere.

3.5.2.2 Recipe Modifications

Unfortunately, the recipe, as presented above, did not consistently produce samples of sufficient quality. Therefore, several modifications were made to the methods used and the recipe itself. These modifications were increasing the pyrolization, using a higher crystallization temperature, improving measurement precision, adjusting the barium acetate mass, and better oxidation control. The reasons these adjustments were made and the results of implementing them are discussed in the remainder of this section.

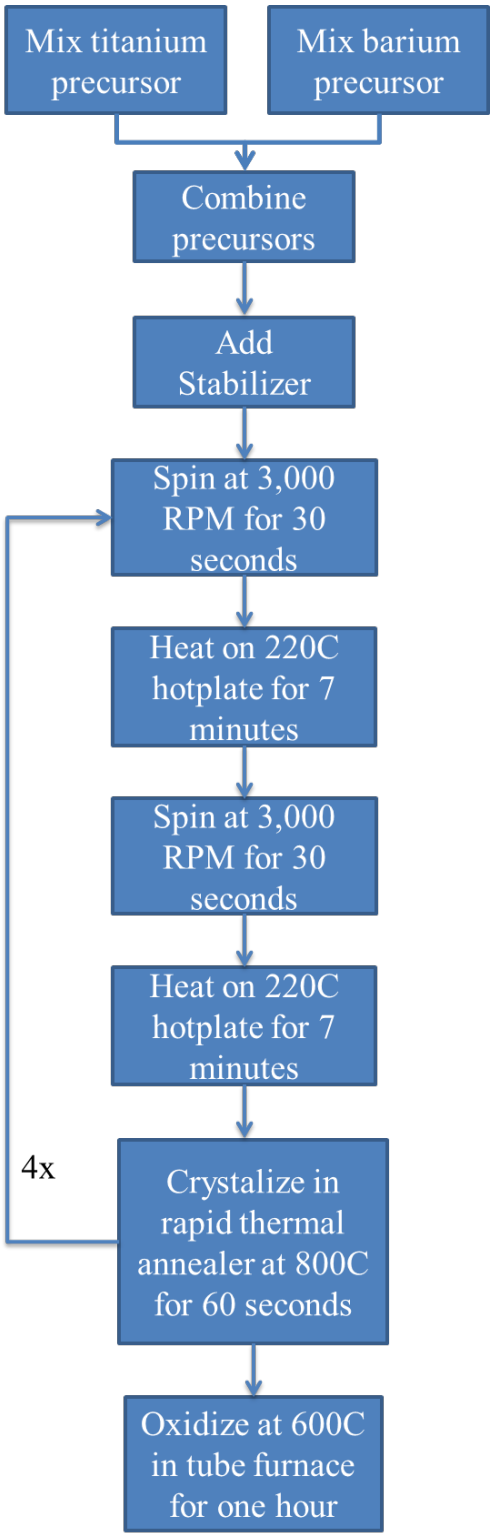

Figure 41: Original sol-gel process flow chart

3.5.2.2.1 Increased Pyrolization

Pyrolization, as it applies to this work, is the process of removing the organic material from the sol by heating. The result of pyrolization is an increased concentration of the Barium and Titanium constituents. When a sol has been partial pyrolized it is referred to as a gel. In this stage, the cross linking between the individual constituents increases. A sol that is completely pyrolized should consist only of barium, titanium, and oxygen. One of the concerns about the recipe discussed in Section 3.5.2.1 was the completeness of the pyrolization. The temperature [157], time [158], and stages of heating [159] all play a role in the amount of pyrolization achieved. The final samples in this research were created using a multi-stage pyrolysis. This process used a low temperature hotplate (150°C), a high temperature hotplate (250°C), and a two stage rapid thermal annealing process. The hotplates were both used for seven minutes after every time the sol was spun onto the sample. The rapid thermal annealing process first ramped to 350°C for one minute before ramping to 700°C for one minutes once the hotplate step had been completed after every other spinning of the sol meaning all films were an even number of spins.

3.5.2.2.2 Higher Crystallization Temperature

In addition to increasing the pyrolization, changing the crystallization parameters had major effects. It is well known that both the temperature and ramp rate make a substantial difference in the dielectric performance of the film [160]. The crystallization temperature is often limited by substrate choice. For example, BTO crystalized on platinum coated silicon substrates with a titanium adhesion layer at 800°C showed diffusion of the silicon through the metal layers and into thin film [161]. However when attempting to grow epitaxially on Nb:STO substrates higher temperature crystallization improved the crystallinity, resulted in a higher dielectric constant, and increased the nonlinearity.

3.5.2.2.3 Improved Liquid Measurement Precision

Initial sols were created in nitrogen atmospheres using vials with septas, which meant that syringes with needles were used to measure liquid chemicals. Eventually it was discovered that mixing the sol in an inert atmosphere made little difference to the end result. Rather, the inert atmosphere was primarily used to extend the lifetime of one of the constituent chemicals. The problem chemical, titanium isopropoxide, could be purchased in small sealed quantities. Therefore, the sols were no longer mixed under flowing nitrogen allowing for the use of pippetters. Before the migration to pippetters the sol-gel growth resulted in inconsistently poor quality films that showed enough promise to continue efforts. After the adoption of pipetting the sol-gel films increased dramatically in quality. It is believed that this improvement in performance was due to the improved stoichiometry of the sol. One measure of quality of a sol is the shelf life which is measured as the length of time before the sol becomes opaque. Early sols, made using syringes lasted for one to two weeks. The first sol made using the pippetters formed deposits on the side of the glassware but otherwise remained translucent for three months.

3.5.2.2.4 Adjusting Ba Concentration

The original recipe specifies a number of barium acetate molecules to be used in mixing the sol [71]. This number was converted to a mass using the molecular mass of barium acetate. However, since acetates are hygroscopic [162, 163], meaning they absorb moisture from the atmosphere, adjustments must be made to the calculated mass in order to account for the additional water content. After discovering this phenomena an additional one percent barium acetate was added to the sol. The result was a sol which remained translucent for over three weeks without forming deposits on the sides of the glassware.

3.5.2.2.5 Oxidation Adjustment

As the research progressed, it became clear that use of Nb:STO as a substrate for this work was unacceptable due to it's relatively low conductivity. Additionally, deposition of BTO on platinum was also ruled out since the platinum dewetted from the STO substrates at the temperatures required for crystallization. Therefore, nickel and nickel coated STO (doped or undoped) became the substrates of choice. This meant that oxidation of the BTO without oxidation of the nickel became important. To achieve this, an oxide MBE reactor was used to provide a controlled background pressure of O_2 and a controlled substrate temperature. Use of an Ellingham diagram [164-166] with the vertical axis showing Torr of pure O_2, shown in Figure

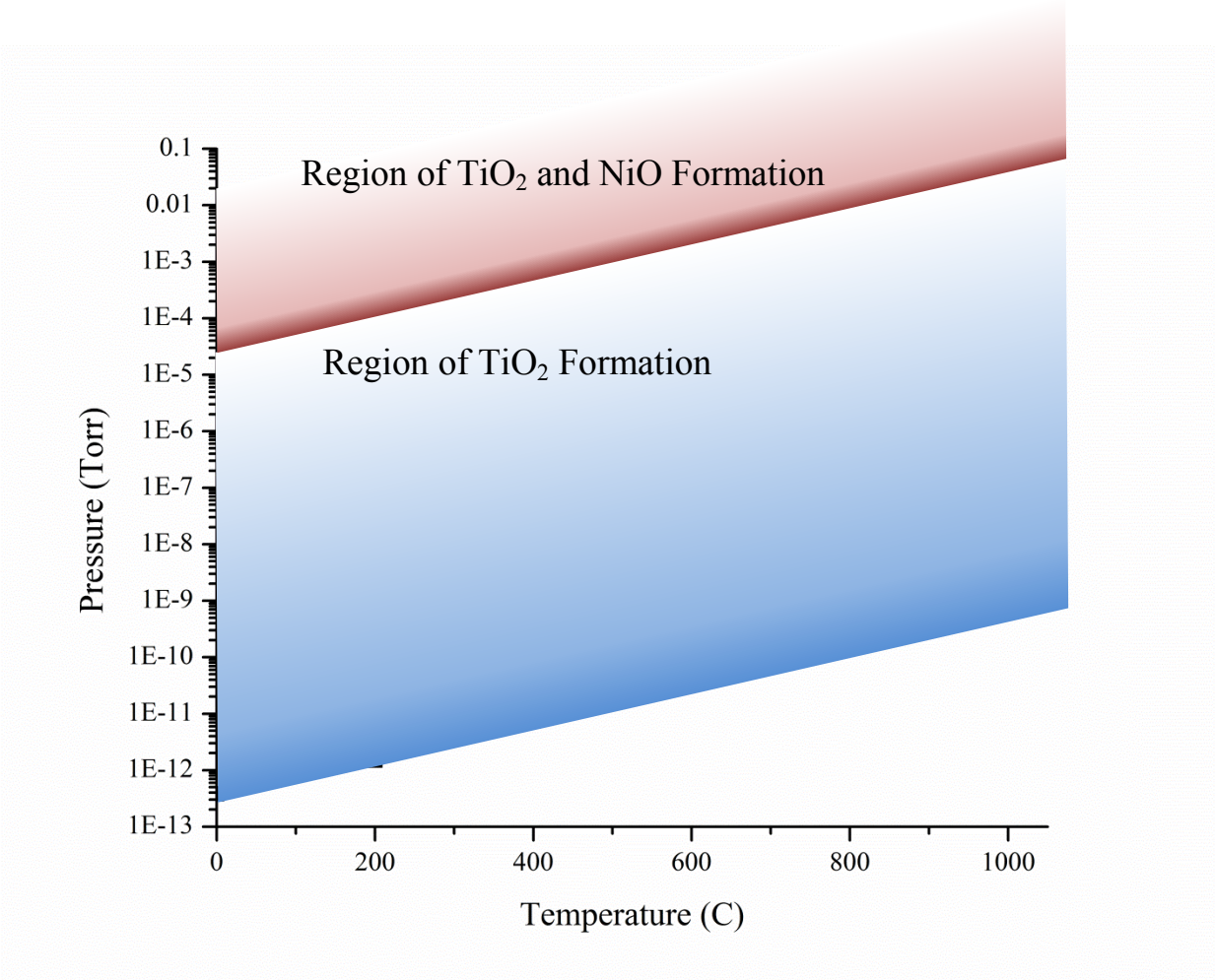

Figure 42: Temperature versus pressure for the formation of TiO2 and NiO

42, determined the temperature and pressure settings used during the oxidation process. Since it was suspected that the O_2 pressure was substantially higher at the sample than at the chamber pressure gauge, some tooling factor adjustments were to be made. Experimentally, it was found that annealing with an oxygen pressure of $2.0 \times 10^{-6}\ Torr$ resulted in the formation of nickel oxide while annealing with an oxygen pressure of $1.0 \times 10^{-6}\ Torr$ did not result in the formation of nickel oxide. Therefore, all the material used for devices was annealed at an oxygen pressure of $1.0 \times 10^{-6}\ Torr$.

3.5.2.3 XRD

Results of XRD measurements indicated that the grown films had lattice constants consistent with BTO. Figure 43 shows high resolution theta-2theta measurement for two typical

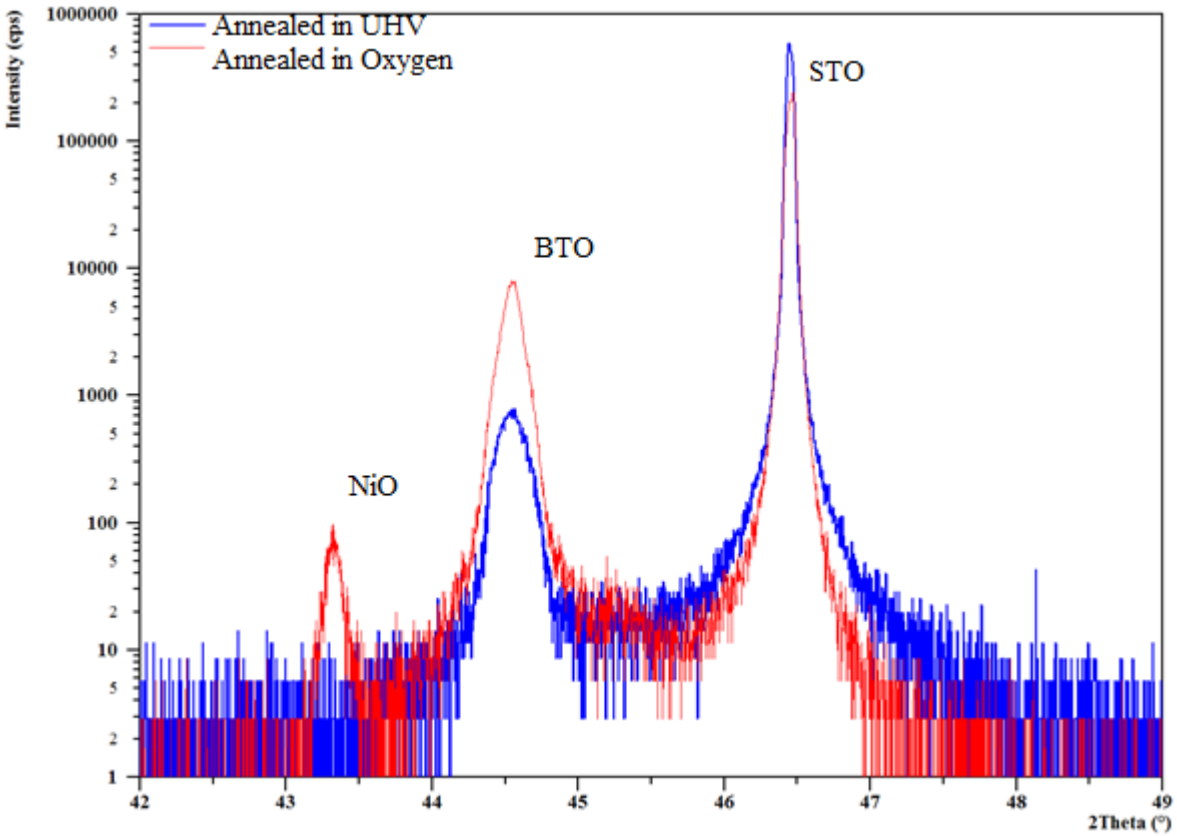

Figure 43: Typical theta-2theta measurements for a sample with NiO after annealing in O_2 atmosphere and a sample without NiO after annealing in ultrahigh vacuum.

BTO films grown on a nickel coated Nb:STO substrates. The theta-2theta measurements had peaks that matched the (002) peak of STO and the (002) peak of BTO. Notice that the measurement from sample 082312-1, the thin red curve, had a peak at 43.34 degrees that was not present in the measurement from sample 082312-2, which was the thick blue curve. This peak was consistent with NiO and indicated that the oxygen pressure was too high during the oxidation process. Sample 082312-2 was also oxidized with sufficient pressure to form NiO but the oxygen was driven out of the nickel by annealing in a vacuum. This demonstrated the ability to sufficiently control both temperature and oxygen pressure to oxidize the BTO without oxidizing the Ni using the MBE reactor.

3.5.2.4 XPS

Analysis by XPS shows the concentrations of barium and titanium to be within the error of the instrument. Furthermore, a depth profile shows there is no carbon below the surface. This means that the pyrolization and crystallization process is removing all the carbon from the gel. Figure 44 shows a survey scan of a typical sample. There is carbon peak which results from exposure to atmosphere. Other than carbon, the only elements found in the sample are barium, titanium, and oxygen. Analysis of element specific scans results in the fractional elemental concentrations of 3.7% carbon, 17.3% barium, 16.9% titanium, and 62.1% oxygen. After accounting for the carbon over layer and the relative error associated with XPS this measurement is within the expected range.

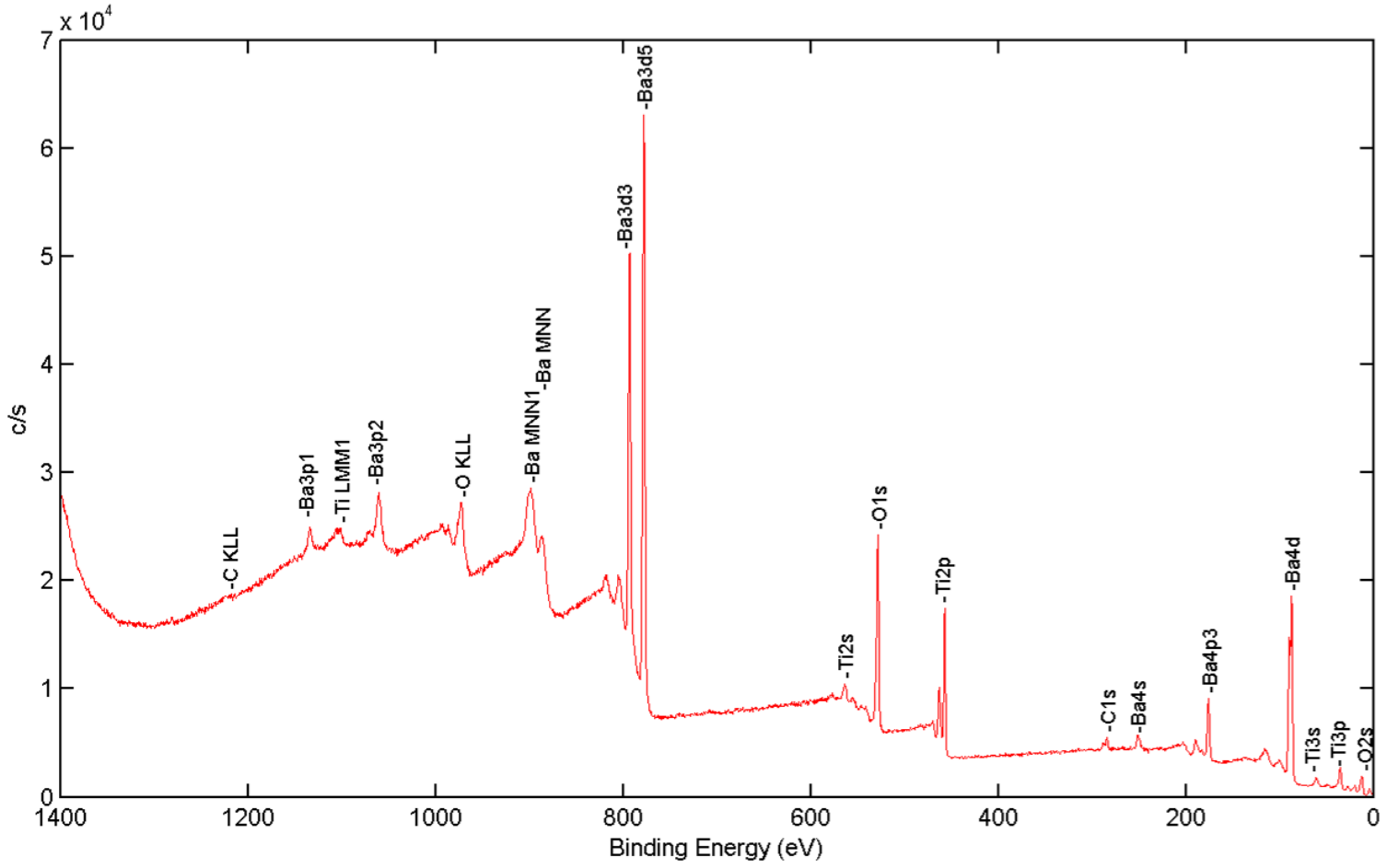

Figure 44: XPS spectrum of typical sol-gel grown BTO.

3.5.2.5 TEM

High resolution TEM, Figure 45, showed that the lattice spacing of the sol-gel grown BTO was 4 Angstroms which matches the lattice parameters given in Table 8. Also, the TEM image confirmed the thickness of the deposition to be approximately $40nm$ per spin of the sol. This result was in good agreement with the deposition rates presented in the paper on which the recipe was based [71].

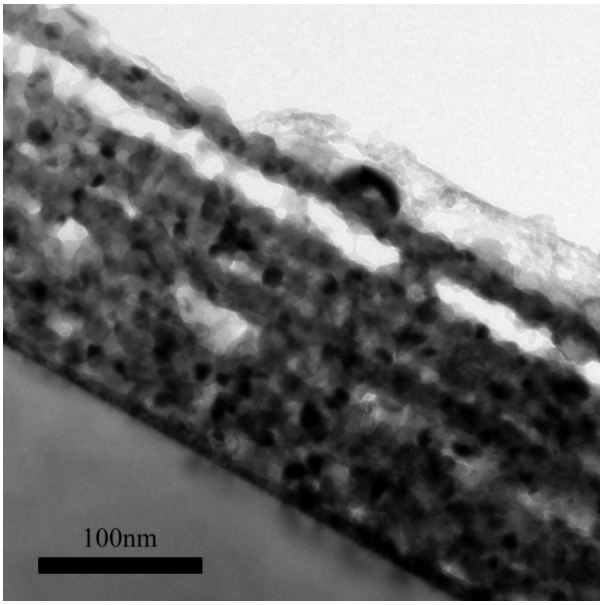

Figure 45: Cross sectional transmission electron micrograph of sol-gel prepared BTO made with four spins.

3.5.2.6 Hysteresis and CV

The hysteresis and CV of the samples were examined to determine if there was sufficient nonlinearity for the proposed device. Early sol-gel films showed little or no nonlinearity. However, more recent films showed more nonlinearity in the CV curve. For example, Figure 46 shows the CV curve for a thin film from which a device, presented in the next chapter, was fabricated. Although the leakage current through the film was larger than 0 A the resistance of $2.9 \times 10^{11}\Omega \cdot cm$ was still sufficiently near infinity as to be negligible.

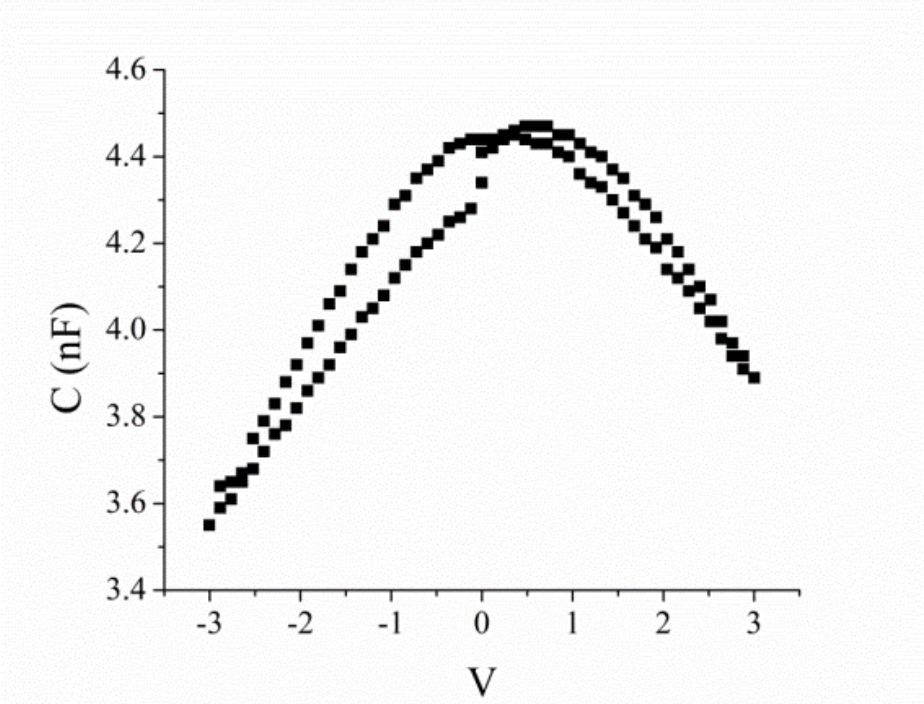

Figure 46: Capacitance versus voltage for sol-gel grown BTO on nickel on Nb:STO.

3.6 Conclusion

In conclusion, several growth methods were investigated for this work and two were implemented. The results of MBE growth of BTO showed limited success but continued to improve providing hope for future materials. Growth of films by the sol-gel method showed more promising results. Film performance was shown to be adequate for the research needs. Adapting the film growth to metallic substrates was achieved by precisely controlling oxidation conditions.

4. Device Design, Fabrication, and Testing

4.1 Introduction

This chapter presents the design, fabrication, and testing of a ferroelectric thin film based nonlinear transmission line. The original intent of this research was to develop a continuous transmission line. This mission was altered slightly to develop a discrete transmission line using ferroelectric thin film material in order to reduce fabrication problems. The next section briefly discusses the logic behind this decision and presents the finalized device design. A section concerning device fabrication will then discuss the steps involved in creating the transmission line. Finally, the results of testing the transmission line will be presented and compared to theory.

4.2 Device Design

As indicated previously, the original intention of the research presented in this dissertation was to create a continuous nonlinear transmission line using a ferroelectric thin film. The two options considered for the design of this device were a microstrip transmission line and a coplanar transmission line. When the microstrip design was investigated the metal resistance was found to be problematic. Assuming the losses are negligible compared to the inductance and capacitance, which is the goal of this effort, then the transmission line impedance is given by

$$Z = \sqrt{\frac{L}{C}} \tag{75}$$

where L is the inductance of the line per unit length and C is the capacitance of the line per unit length which is given by $C = \varepsilon_0 \varepsilon_r \frac{w}{d}$ where ε_0 is the permittivity of a vacuum, ε_r is the relative

permittivity of the dielectric, w is the width of the line, and d is the thickness of the dielectric. Because a signal would propagate at the speed of light if the dielectric were vacuum,

$$c = \frac{1}{\sqrt{LC_0}} \tag{76}$$

where c is the speed of light and C_0 is the capacitance per unit length when the dielectric is assumed to be a vacuum. To see how these parameters effect the geometry of the line this system of equations is solved for w yielding

$$w = \frac{d}{c\varepsilon_0 Z\sqrt{\varepsilon_r}}. \tag{77}$$

Since the transmission line must be impedance matched to the cabling connecting it to the function generator and the oscilloscope, $Z = 50\ \Omega$ and $d = 330$ nm were used based on measurements of the film properties discussed in Chapter 3, then all terms are known. Therefore w is calculated as 110 nm. Silver, which has a resistivity of $1.59 \times 10^{-8}\ \Omega \cdot \mathrm{m}$, was investigated as the trace material to maximize conductance. Using the calculated trace width and silver to calculate resistance led to the curve shown in Figure 47 for a 1 cm long transmission line. Notice that even at a trace thickness of 1 mm the resistance was still greater than 1 Ω. Therefore, the trace would require an aspect ratio of approximately ten thousand. By migrating to a discrete line the impedance matching of the line was maintained at the cost of being able to fabricate a monolithic device.

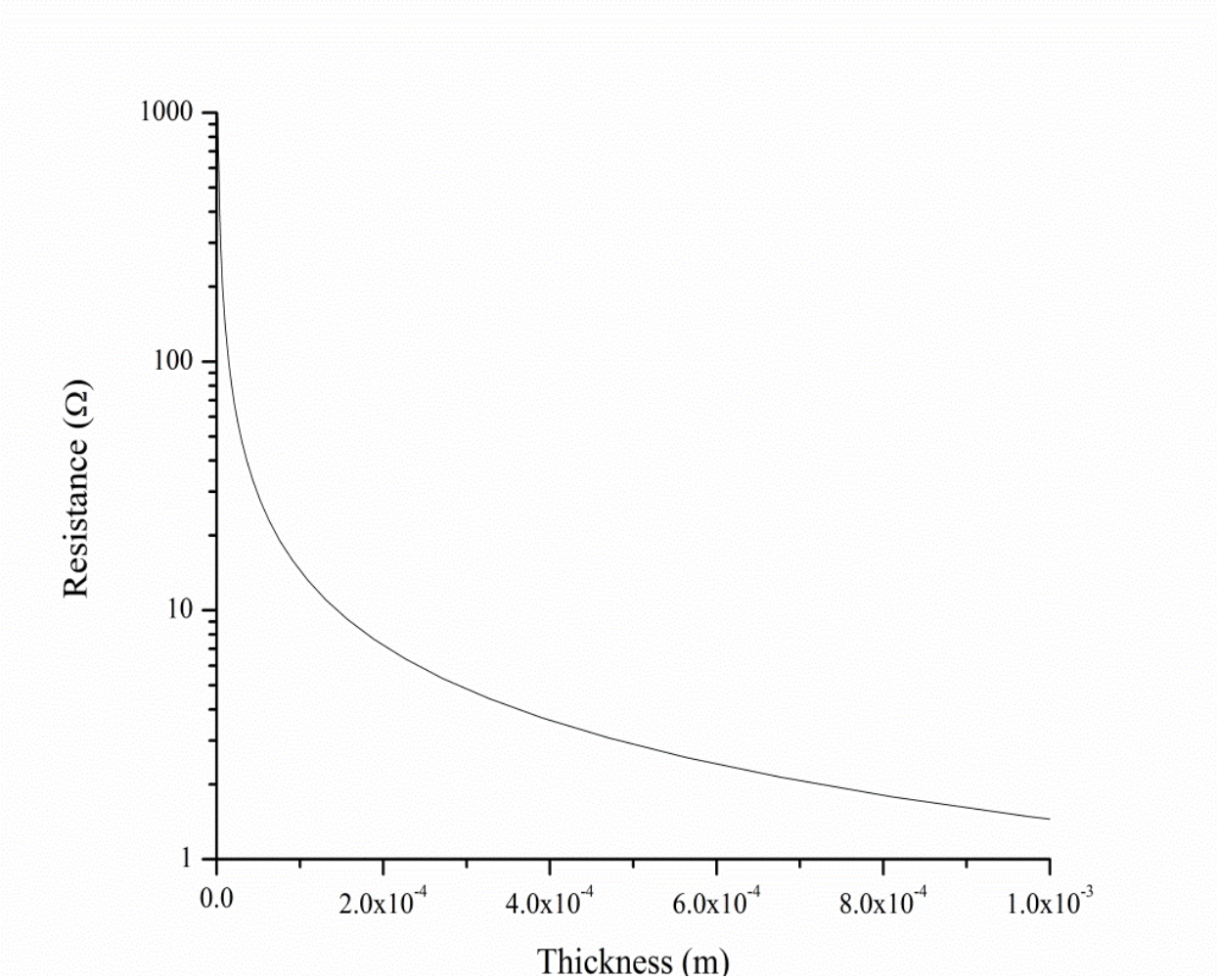

Figure 47: Trace resistance versus trace thickness for 110nm wide silver trace

The size of the thin film capacitors, 3.8×10^{-9} m^2, was chosen such that it was near the limit for wedge bonding with the available equipment. The capacitance of each pad was designed to be 4.8 pF. The number of nodes in the device was limited by the chip carrier, JCC8446002 from Global Chip Materials, LLC, which was chosen to maximize density while maintaining ease of fabrication. Although chip carriers with more pins are available they are in packages such as a ball grid array which would require soldering to leads under the chip. Also, a higher density of pins would have required additional layers in the printed circuit board leading to increased cost of design and manufacturing. The inductance between each node was chosen based on the

value of the capacitance to be 120 nH to create a line that was 50 Ω. The single layer printed circuit board (PCB) designed for this project is shown in Figure 48. An error in the printed circuit board layout was later found and corrected by shorting two pins of the chip carrier. This had the effect of shortening the transmission line by one unit cell.

The length, width, and weight of the traces were chosen to ensure that the contribution to the inductance of the system was less than ten percent of the overall inductance. Specifically, the inductance of parallel lines of 1oz copper was approximately 1.2 nH/mm when the traces were 0.25 mm wide with a spacing of 1 mm [167]. The traces in the discrete transmission line PCB used $2oz$ copper and were slightly wider than the number indicated above. Since the typical trace length was less than 10mm this means that the typical trace inductance of the PCB was less than 12 nH.

Since many inductors use ferrite cores inductor linearity was a concern for this device. Examining a single LC circuit with a 50Ω load showed that a step input results in a maximum current of less than 40 mA. The inductors chosen for the transmission line, TDK part number

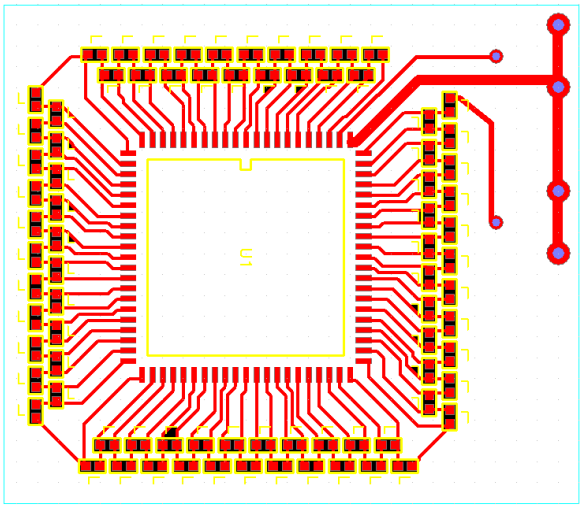

Figure 48: Layout of discrete element transmission line PCB

MLZ1608DR22DT, were nearly constant to currents over 100 mA according to both the data sheet [168] and to tests performed on an a series circuit of 22 inductors using an HP4192 impedance analyzer. The 22 inductors were shown to have an impedance of 3.03 μH with 2.6 mA of current and 3 μH of inductance at 36.3 mA of current. Since this change was only one percent, the nonlinearity in the circuit was a result of the nonlinear capacitors. To further alleviate any concerns about the performance of the inductors, a linear artificial transmission line was constructed using linear off the shelf capacitors. The results from testing the linear device will be presented in parallel to the results of the nonlinear device. Note that if the inductors were chosen differently two nonlinear elements that act in the same direction could have been exploited.

4.3 Device Fabrication

Fabrication of a nonlinear transmission line consisted of seven steps once the ferroelectric material had been grown and characterized. First, a series of capacitors were created using electron beam lithography. Next, the size of the capacitors was verified. Third, the sample was attached to the chip carrier. Then, each pin on the chip carrier was wire bonded to a capacitor. Fifth, the chip was soldered to a PCB. The PCB was then populated with inductors. Finally, Bayonet Neill-Concelman (BNC) connectors were soldered to the board. A picture of a final device is shown in Figure 49.

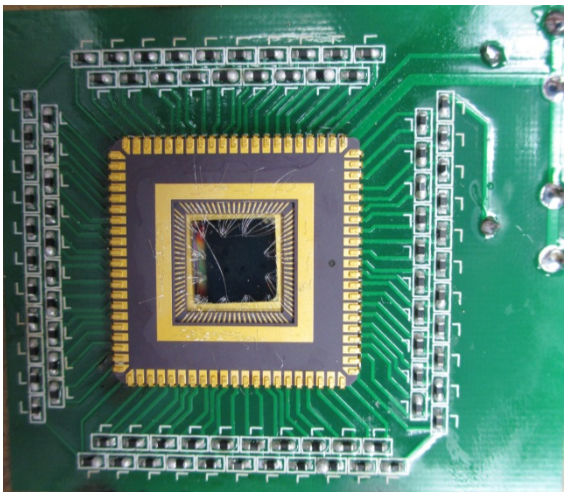

Figure 49: Discrete ferroelectric thin film based transmission line.

4.4 Device Testing

The nonlinear transmission line was tested using a Tektronix TDS 2012 oscilloscope and a Stanford Research Systems DS345 function generator. The line was loaded with a resistance of 56Ω to match the impedance of the transmission line. The function generator was set to produce 1 MHz single period sinusoids with an offset and a phase shift such that the result was a positive pulse from a 0 V background.

In addition to the nonlinear transmission line two other devices were tested. The first was simply a female BNC to female BNC adapter, known as a bullet, used to show the effect of the lines, the connections, and the load. The second was the linear transmission line discussed in Section 4.2. The full results are shown in Figure 50. The error bars represent the standard deviation of the bullet measurements. When taken as a whole, the data did not appear to provide evidence of sharpening. However a piecewise examination, which is indicated on the graph showed a region of sharpening. The two regions of Figure 50 are plotted separately in Figure 51 and Figure 52 and are described in the following paragraphs.

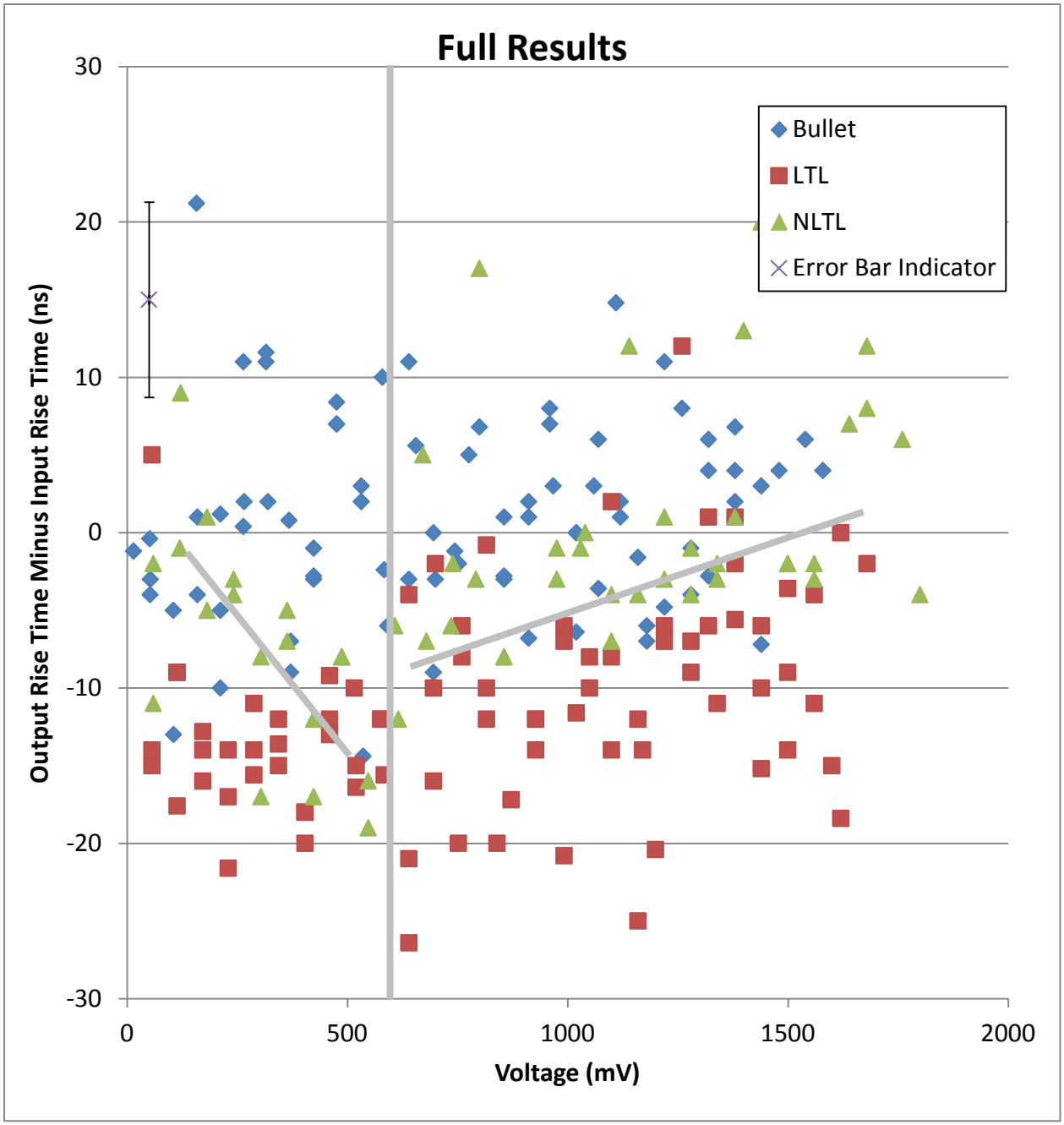

Figure 50: Full Measurement Data from the Bullet, the Linear Transmission Line and the Nonlinear Transmission Line.

Figure 51 displays the results from the measurements from pulses with a peak voltage of 0 V to 600 mV with panel (a) showing the data from the bullet, panel (b) showing the data from the linear transmission line, and panel (c) showing the data from the nonlinear transmission line. The error bars are from the standard deviation ten measurements made at a single voltage for

each device after disconnecting and reconnecting the cables. The slopes of the fit lines are $0.0055\ \mathrm{ns/mV}$ for the bullet, $-0.0047\ \mathrm{ns/mV}$ for the linear transmission line, and $-0.0243\ \mathrm{ns/mV}$ for the nonlinear transmission line. These data showed that for voltages of less than $600\ \mathrm{mV}$ there is a trend of sharpening for the nonlinear transmission line.

Figure 52 shows the results for the measurements from pulses with a peak voltage of greater than $600\ \mathrm{mV}$. Again, panel (a) shows the data from the bullet, panel (b) shows the data from the linear transmission line, and panel (c) shows the data from the nonlinear transmission line. The error bars have the same meaning as in the Figure 51. In this case the line of best fit for all the devices had positive slopes. Specifically, the slopes of the fit lines are $0.0034\ \mathrm{ns/mV}$ for the bullet, $0.0053\ \mathrm{ns/mV}$ for the linear transmission line, and $0.0039\ \mathrm{ns/mV}$ for the nonlinear transmission line.

There was no explanation found of why the performance of the line changed slope. The data was collected three times and all data sets showed the same trend. This indicated that, at least for the potentials tested, the degradation in performance was not attributable to the material breaking down from fatigue or overvoltage. One possibility was that there was sufficient current and loss in the system to be causing a change in temperature that effected the material properties. In this case, one would expect enough heat to cause a phase change at about $600mV$ where the kink in the data was found.

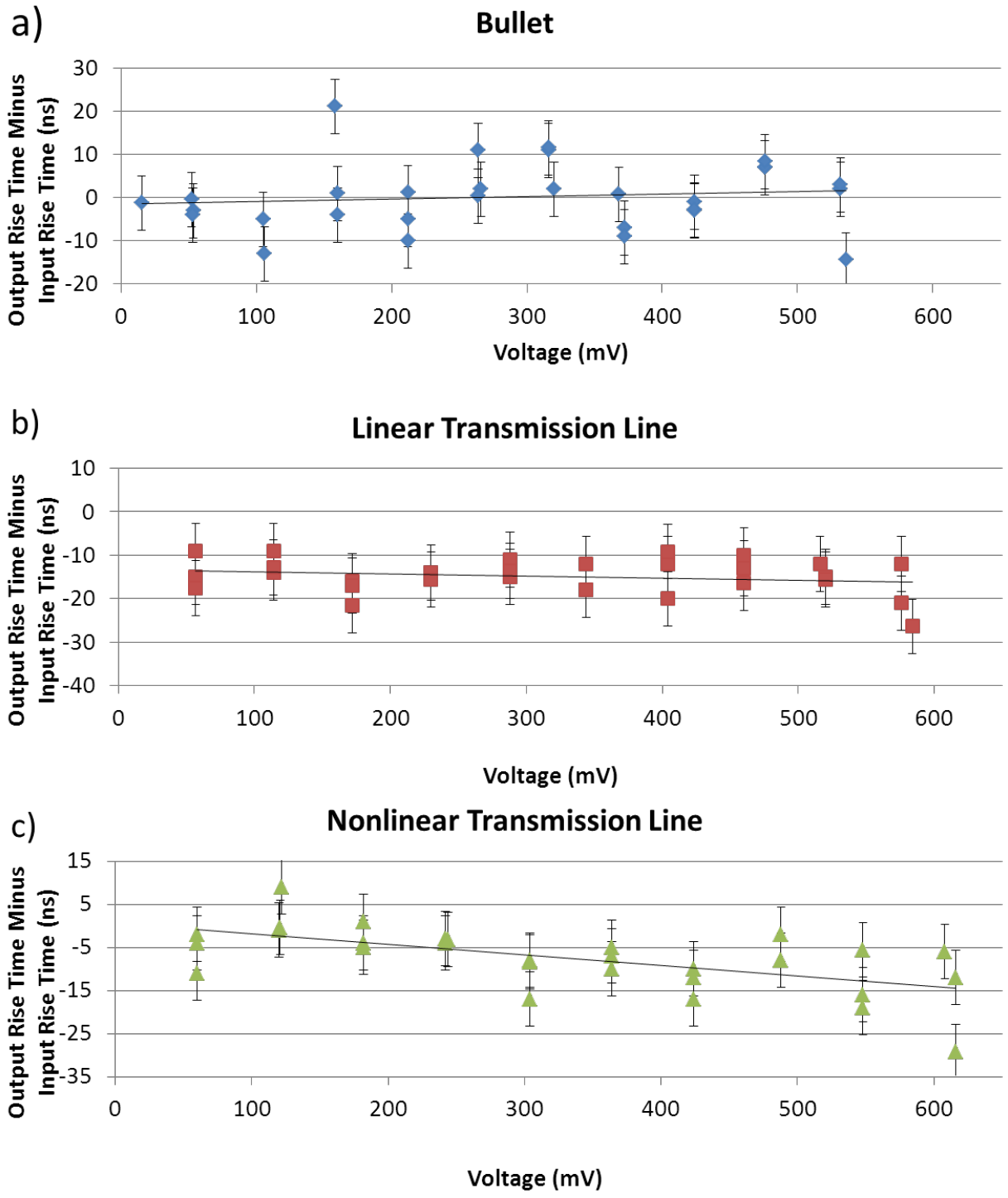

Figure 51: Rise Time at Device Output Minus Rise Time at Device Input as a Function of Voltage for Less Than 600 mV.

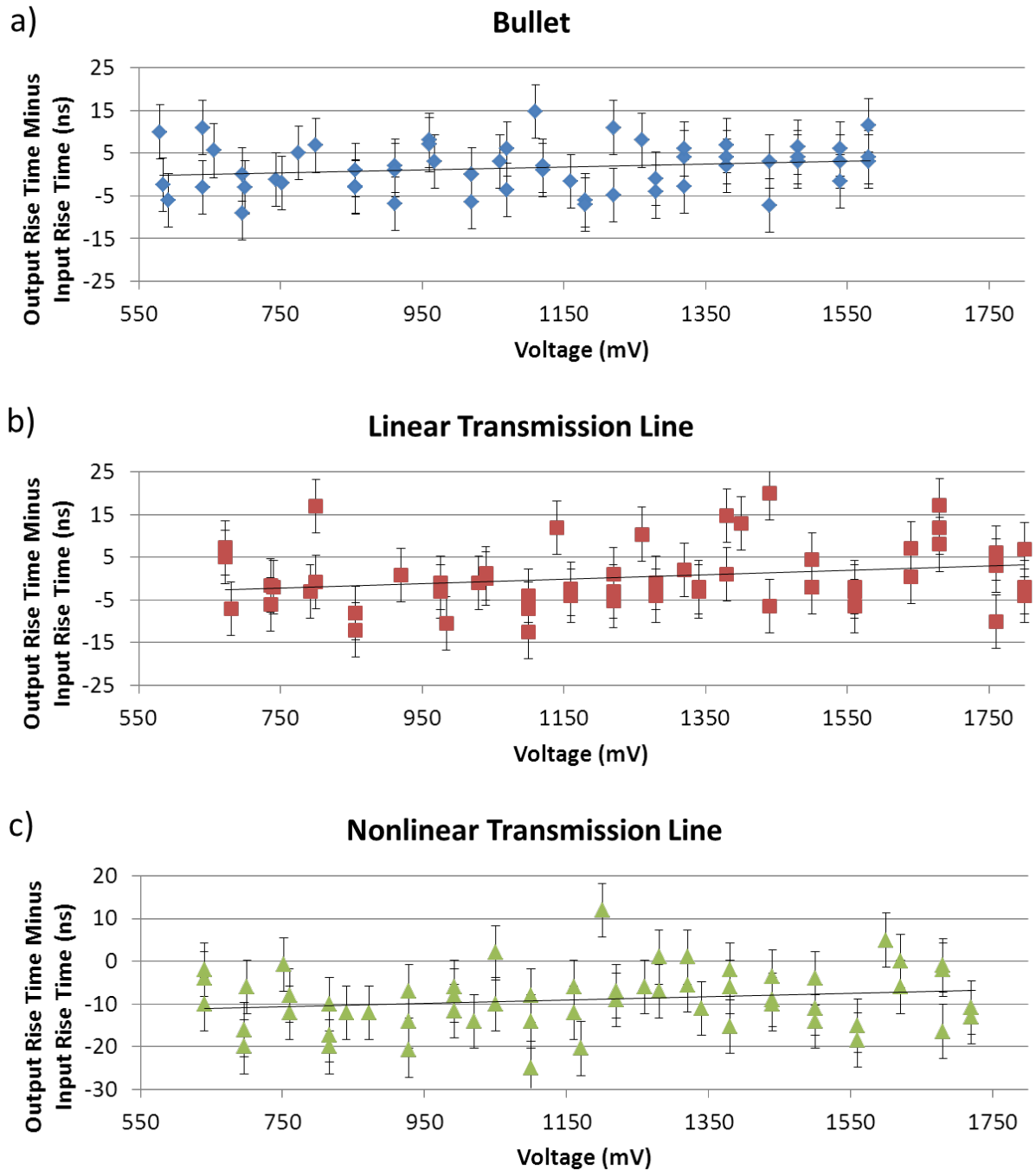

Figure 52: Rise Time at Device Output Minus Rise Time at Device Input as a Function of Voltage for Greater Than 600 mV.

5. Conclusion

At the beginning of the research for this dissertation it was proposed that a nonlinear transmission line be studied and fabricated. It was expected that the line would shape electrical propagating electrical pulses and generate sharp rising edge transitions. The proposed device would operate at lower voltages and be smaller in size than the current state of the art.

The state of the art systems were found to have several drawbacks including voltage required, device size, and performance limitations. It was proposed that these limitations could be overcome by utilizing advances in material science and exploiting the properties of thin film ferroelectric material. To the best of the author's knowledge thin film ferroelectric transmission lines have not previously been studied.

The objective of the research presented in this dissertation was to simulate, fabricate, and demonstrate a thin film ferroelectric transmission line. To that end, simulations were developed and used to predict the behavior of such a transmission line, thin film ferroelectric samples were grown and characterized, a transmission line was created using the grown material, and behavior of the transmission line was investigated.

There are several outcomes from the research performed for this dissertation. First, the theory was advanced to include both frequency dependent losses and dispersion. Second, a molecular beam epitaxy reactor was used to precisely control both the temperature and the oxygen pressure during the oxidation process. This allowed for optimal oxidation of the barium titanate while avoiding the formation of NiO. Third, a thin film ferroelectric transmission line was constructed using discrete elements. Finally, the thin film ferroelectric transmission line was shown to sharpen the rising edge of pulses with a peak voltage of 600 mV by 15 ns.

The next step in the development of the device presented in this dissertation should focus towards making a continuous and monolithic nonlinear transmission line. Such a device would not suffer from any of the voltage, size, or performance disadvantages discussed above. Once a continuous monolithic device has been demonstrated it could be incorporated into existing electronics. However, to optimize the usability of a ferroelectric based nonlinear transmission line in electronic devices it must be integrated with other devices. Hopefully current research trends in oxide materials will lead to opportunities for such integration.

References

[1] E. Afshari and A. Hajimiri, "Nonlinear transmission lines for pulse shaping in silicon," *Solid-State Circuits, IEEE Journal of,* vol. 40, pp. 744-752, 2005.

[2] M. Tan, C. Y. Su, and W. J. Anklam, "7× electrical pulse compression on an inhomogeneous nonlinear transmission line," *Electronics Letters,* vol. 24, pp. 213-215, 1988.

[3] F. Ellinger, H. Jackel, and W. Bachtold, "Varactor-loaded transmission-line phase shifter at C-band using lumped elements," *Microwave Theory and Techniques, IEEE Transactions on,* vol. 51, pp. 1135-1140, 2003.

[4] G. A. Mundy, "Pulse Sharpening by Magnetic Compression," Stanford Linear Accelerator Center, Stanford, CA February 1991 1991.

[5] C. R. Wilson, M. M. Turner, and P. W. Smith, "Pulse sharpening in a uniform <e1>L</e1>C ladder network containing nonlinear ferroelectric capacitors," *Electron Devices, IEEE Transactions on,* vol. 38, pp. 767-771, 1991.

[6] G. Branch and P. W. Smith, "ELECTROMAGNETIC SHOCK-WAVES IN DISTRIBUTED DELAY LINES WITH NONLINEAR DIELECTRICS," in *Power Modulator Symposium, 1992. Conference Record of the 1992 Twentieth*, 1992, p. 355.

[7] M. Remoissenet, *Waves Called Solitons: Concepts and Experiments*, 3rd ed. New York, New York: Springer, 1999.

[8] M. F. Hamilton and D. T. Blackstock, *Nonlinear acoustics*: Academic Press, 1998.

[9] D. Donskoy, A. Sutin, and A. Ekimov, "Nonlinear acoustic interaction on contact interfaces and its use for nondestructive testing," *NDT & E International,* vol. 34, pp. 231-238, 2001.

[10] R. Kompfner, "Nonlinear acoustic microscopy," *Appl. Phys. Lett.,* vol. 28, p. 295, 1976.

[11] M. A. Averkiou, D. N. Roundhill, and J. E. Powers, "A new imaging technique based on the nonlinear properties of tissues," in *Ultrasonics Symposium, 1997. Proceedings., 1997 IEEE*, 1997, pp. 1561-1566 vol.2.

[12] J. J. Stoker, *Water Waves: The Mathematical Theory with Applications*. New York, New York: Wiley, 1992.

[13] K.-H. Lee and N. Mizutani, "Experimental Study of Wave Breaking of Periodic Waves on a Gravel Beach," *Journal of Coastal Research,* pp. 967-975, 2011/04/15.

[14] T. H. C. Herbers, S. Elgar, N. A. Sarap, and R. T. Guza, "Nonlinear Dispersion of Surface Gravity Waves in Shallow Water*," *Journal of Physical Oceanography,* vol. 32, pp. 1181-1193, 2002.

[15] J. L. Lara, A. Ruju, and I. J. Losada, "Reynolds averaged Navierâ€“Stokes modelling of long waves induced by a transient wave group on a beach," *Proceedings of the Royal Society A: Mathematical, Physical and Engineering Science,* vol. 467, pp. 1215-1242, May 8, 2011.

[16] A. T. Filippov, *The versatile soliton*. Boston; New York; London: Birkhäuser ; Springer [distributor].

[17] M. Remoissenet, *Waves called solitons : concepts and experiments*. Berlin; New York: Springer, 1999.

[18] T. Dauxois and M. Peyrard, *Physics of Solitons*. Cambridge, UK: Cambrideg University Press, 2006.

[19] M. Wadati, "Introduction to solitons," *Pramana,* vol. 57, pp. 841-847, 2001.

[20] J. W. Miles, "Solitary Waves," *Annual Review of Fluid Mechanics,* vol. 12, pp. 11-43, 1980.

[21] K. Fujioka, K. Okino, T. Kanamatsu, and Y. Ohara, "Morphology and origin of the Challenger Deep in the Southern Mariana Trench," *Geophys. Res. Lett.,* vol. 29, p. 1372, 2002.

[22] J. Gower, "The 26 December 2004 tsunami measured by satellite altimetry," *International Journal of Remote Sensing,* vol. 28, pp. 2897-2913, 2012/01/31 2007.

[23] S. S. Voit, "Tsunamis," *Annual Review of Fluid Mechanics,* vol. 19, pp. 217-236, 1987.

[24] R. W. Boyd, *Nonlinear optics*: Academic Press, 2003.

[25] E. Cumberbatch, "Self-focusing in Non-linear Optics," *IMA Journal of Applied Math,* vol. 6, pp. 250-262, 1970.

[26] M. Segev and G. Stegeman, "Self-Trapping of Optical Beams: Spatial Solitons," *Physics Today,* vol. 51, pp. 42-48, 1998.

[27] J. L. Shultz and G. J. Salamo, "Experimental Observation of the Continuous Pulse-Train Soliton Solution to the Maxwell-Bloch Equations," *Physical Review Letters,* vol. 78, p. 855, 1997.

[28] F. M. Knox, W. Forysiak, and N. J. Doran, "10-Gbt/s soliton communication systems over standard fiber at 1.55 μm and the use of dispersion compensation," *Lightwave Technology, Journal of,* vol. 13, pp. 1955-1962, 1995.

[29] R. Gangwar, S. P. Singh, and N. Singh, "Soliton Based Optical Communication," *Progress in Electromagnetics Research,* vol. 74, pp. 157-166, 2007.

[30] H. Hatami-Hanza, A. Mostofi, and P. L. Chu, "A multilevel soliton communication system," in *Lasers and Electro-Optics Society Annual Meeting, 1995. 8th Annual Meeting Conference Proceedings, Volume 1., IEEE*, 1995, pp. 35-36 vol.2.

[31] R. A. Baki, T. K. K. Tsang, and M. N. El-Gamal, "Distortion in RF CMOS short-channel low-noise amplifiers," *Microwave Theory and Techniques, IEEE Transactions on,* vol. 54, pp. 46-56, 2006.

[32] S. A. Maas, *Nonlinear microwave and RF circuits*: Artech House, 2003.

[33] R. I. Neophytou and A. C. Metaxas, "Investigation of the Harmonic Generation in Convetional Radio Frequency Heating Systems," *Journal of Microwave Power and Electromagnetic Energy,* vol. 34, pp. 84-96, 1999.

[34] H. Aintablian, "The harmonic currents of commercial office buildings due to non-linear electronic equipment," in *Southcon/96. Conference Record*, 1996, pp. 610-615.

[35] M. Yamaguchi, K. Ki-Hyeon, T. Kuribara, and A. Ken-Ichi, "Thin-film RF noise suppressor integrated in a transmission line," *Magnetics, IEEE Transactions on,* vol. 38, pp. 3183-3185, 2002.

[36] F. Maiwald, F. Lewen, B. Vowinkel, W. Jabs, D. G. Paveljev, M. Winnewisser, and G. Winnewisser, "Planar Schottky diode frequency multiplier for molecular spectroscopy up to 1.3 THz," *Microwave and Guided Wave Letters, IEEE,* vol. 9, pp. 198-200, 1999.

[37] J. R. Thorpe, P. Steenson, and R. E. Miles, "Non-linear transmission lines for millimeter-wave frequency multiplier applications," in *Terahertz Electronics Proceedings, 1998. THz Ninety Eight. 1998 IEEE Sixth International Conference on*, 1998, pp. 54-57.

[38] W. Han, D. Nezich, K. Jing, and T. Palacios, "Graphene Frequency Multipliers," *Electron Device Letters, IEEE,* vol. 30, pp. 547-549, 2009.

[39] T. H. Lee, "Device physics: Electrical solitons come of age," *Nature,* vol. 440, pp. 36-37, 2006.

[40] M. C. W. Lindmark, "Switched Mode Power Supply," U. S. P. a. T. Office, Ed. United States of America, 1978, p. 5.

[41] R. Landauer, "Parametric Amplification along Nonlinear Transmission Lines," *J. Appl. Phys.,* vol. 31, p. 479, 1960.

[42] D. M. Pozar, *Microwave engineering*: J. Wiley, 2005.

[43] T. Tsuboi and F. M. Toyama, "Computer experiments on solitons in a nonlinear transmission line. I. Formation of stable solitons," *Physical Review A,* vol. 44, pp. 2686-2690, 1991.

[44] R. H. Freeman and A. E. Karbowiak, "An investigation of nonlinear transmission lines and shock waves," *Journal of Physics D: Applied Physics,* vol. 10, p. 633, 1977.

[45] F. A. Benson, J. D. Last, and V. I. Zharikov, "Analysis of lumped-parameter nonlinear transmission lines," *Electronics Letters,* vol. 1, pp. 247-248, 1965.

[46] D. J. Korteweg and G. de Vries, "On the change of form of long waves advancing in a rectangular canal and on a new type of long stationary waves," *Phil. Mag.,* vol. 39, pp. 422-443, 1895.

[47] R. M. Miura, "The Korteweg-de Vries Equation: A Survey of Results," *SIAM Review,* vol. 18, pp. 412-459, 1976.

[48] C. S. Gardner, J. M. Greene, M. D. Kruskal, and R. M. Miura, "Method for Solving the Korteweg-deVries Equation," *Physical Review Letters,* vol. 19, p. 1095, 1967.

[49] P. D. Lax, P. Sarnak, and A. Majda, "Periodic Solutions of the KdV Equation," in *Selected Papers Volume I*: Springer New York, 2005, pp. 390-437.

[50] A. Jeffrey and T. Kakutani, "Weak Nonlinear Dispersive Waves: A Discussion Centered Around the Korteweg--De Vries Equation," *SIAM Review,* vol. 14, pp. 582-643, 1972.

[51] T. Taniuti and K. Nishihara, *Nonlinear Waves*. Marshfield, Massachusetts: Pitman Publings Incorporated, 1977.

[52] H. Ghafouri-Shiraz and P. Shum, "Formation of narrow pulses in a nonlinear lossy LC ladder network," *Circuits and Systems I: Fundamental Theory and Applications, IEEE Transactions on,* vol. 43, pp. 243-245, 1996.

[53] M. P. J. Tiggelman, K. Reimann, M. Klee, D. Beelen, W. Keur, J. Schmitz, and R. J. E. Hueting, "Electrical characterization of thin film ferroelectric capacitors," in *Proceedings of the 9th annual workshop on Semiconductor Advances for Future Electronics and Sensors 2006*, Veldhoven, The Netherlands, 2006.

[54] M. N. Kamalasanan, N. D. Kumar, and S. Chandra, "Dielectric and ferroelectric properties of BaTiO[sub 3] thin films grown by the sol-gel process," *Journal of Applied Physics,* vol. 74, pp. 5679-5686, 1993.

[55] F. Seitz and D. Turnbull, *Solid State Physics: Advances in Research and Applications*: Academic Press, 1957.

[56] E. Fatuzzo and W. J. Merz, *Ferroelectricity*: North-Holland Pub. Co., 1967.

[57] K. Uchino, *Ferroelectric devices*: Marcel Dekker, 2000.

[58] C. Kittel, *Introduction to solid state physics*: Wiley, 2005.

[59] D. Dragan, "Ferroelectric, dielectric and piezoelectric properties of ferroelectric thin films and ceramics," *Reports on Progress in Physics,* vol. 61, p. 1267, 1998.

[60] S. Gevorgian, *Ferroelectrics in Microwave Devices, Circuits and Systems*. London, England: Springer, 2009.

[61] A. K. Tagantsev, J. Lu, and S. Stemmer, "Temperature dependence of the dielectric tunability of pyrochlore bismuth zinc niobate thin films," *Applied Physics Letters,* vol. 86, pp. 032901-3, 2005.

[62] J. Valasek, "Piezo-Electric and Allied Phenomena in Rochelle Salt," *Physical Review,* vol. 17, pp. 475-481, 1921.

[63] C. B. Sawyer and C. H. Tower, "Rochelle Salt as a Dielectric," *Physical Review,* vol. 35, pp. 269-273, 1930.

[64] G. H. Haertling, "Ferroelectric Ceramics: History and Technology," *Journal of the American Ceramic Society,* vol. 82, pp. 797-818, 1999.

[65] W. J. Borland, J. F. Ihlefeld, A. I. Kingon, and J.-P. Maria, "Thin film dielectrics for capacitors and methods of making thereof," U. S. P. a. T. Office, Ed. Unitaed State of America: E. I. duPont de Nemours and Compny, North Carolina State University, 2006.

[66] T. Dechakupt, "Microstructure-processing-property Relations in Chemical Solution Deposited Barium Titanate Films," in *Materials Science and Engineering*. vol. Ph. D. University Park, PA: Pennsylvania State University, 2007, p. 172.

[67] T. Dechakupt, G. Yang, C. A. Randall, S. Trolier-McKinstry, and I. M. Reaney, "Chemical Solution-Deposited BaTiO3 Thin Films on Ni Foils: Microstructure and Interfaces," *Journal of the American Ceramic Society,* vol. 91, pp. 1845-1850, 2008.

[68] M. H. Frey and D. A. Payne, "Synthesis and processing of barium titanate ceramics from alkoxide solutions and monolithic gels," *Chemistry of Materials,* vol. 7, pp. 123-129, 1995.

[69] Y. Guo, K. Suzuki, K. Nishizawa, T. Miki, and K. Kato, "Thickness Dependence of Electrical Properties of Highly (100)-Oriented BaTiO₃ Thin Films Prepared by One-Step Chemical Solution Deposition," *Japanese Journal of Applied Physics,* vol. 45, pp. 855-859, 2006.

[70] M. C. Gust, L. A. Momoda, N. D. Evans, and M. L. Mecartney, "Crystallization of Sol–Gel-Derived Barium Strontium Titanate Thin Films," *Journal of the American Ceramic Society,* vol. 84, pp. 1087-1092, 2001.

[71] R. D. Levi, M. M. Samantaray, S. Trolier-McKinstry, and C. A. Randall, "Influence of substrate microstructure on the high field dielectric properties of BaTiO[sub 3] films," *Journal of Applied Physics,* vol. 104, pp. 104117-8, 2008.

[72] S. B. Majumder, M. Jain, A. Martinez, R. S. Katiyar, F. W. Van Keuls, and F. A. Miranda, "Sol--gel derived grain oriented barium strontium titanate thin films for phase shifter applications," *Journal of Applied Physics,* vol. 90, pp. 896-903, 2001.

[73] T. Noh, S. Kim, and C. Lee, "Chemical Preparation of Barium-Strontium Titanate," *Bulletin of the Korean Chemical Society,* vol. 16, pp. 1180-1184, 20 December 1995 1995.

[74] H. B. Sharma and A. Mansingh, "Sol-gel processed barium titanate ceramics and thin films," *Journal of Materials Science,* vol. 33, pp. 4455-4459, 1998.

[75] H. N. Lee, H. M. Christen, M. F. Chisholm, C. M. Rouleau, and D. H. Lowndes, "Strong polarization enhancement in asymmetric three-component ferroelectric superlattices," *Nature,* vol. 433, pp. 395-399, 2005.

[76] V. Craciun and R. K. Singh, "Characteristics of the surface layer of barium strontium titanate thin films deposited by laser ablation," *Applied Physics Letters,* vol. 76, pp. 1932-1934, 2000.

[77] J. Gonzalo, R. Gómez San Román, J. Perrière, C. N. Afonso, and R. Pérez Casero, "Pressure effects during pulsed-laser deposition of barium titanate thin films," *Applied Physics A: Materials Science & Processing,* vol. 66, pp. 487-491, 1998.

[78] R. Ramesh, A. Inam, W. K. Chan, F. Tillerot, B. Wilkens, C. C. Chang, T. Sands, J. M. Tarascon, and V. G. Keramidas, "Ferroelectric PbZr[sub 0.2]Ti[sub 0.8]O[sub 3] thin films on epitaxial Y-Ba-Cu-O," *Applied Physics Letters,* vol. 59, pp. 3542-3544, 1991.

[79] C. Zaldo, D. S. Gill, R. W. Eason, J. Mendiola, and P. J. Chandler, "Growth of KNbO[sub 3] thin films on MgO by pulsed laser deposition," *Applied Physics Letters,* vol. 65, pp. 502-504, 1994.

[80] T. Horikawa, N. Mikami, T. Makita, J. Tanimura, M. Kataoka, K. Sato, and M. Nunoshita, "Dielectric Properties of (Ba, Sr)TiO$_{3}$ Thin Films Deposited by RF Sputtering," *Japanese Journal of Applied Physics,* vol. 32, 1993.

[81] W. Shu-Yau, "A new ferroelectric memory device, metal-ferroelectric-semiconductor transistor," *Electron Devices, IEEE Transactions on,* vol. 21, pp. 499-504, 1974.

[82] S. B. Krupanidhi, N. Maffei, M. Sayer, and K. El-Assal, "rf planar magnetron sputtering and characterization of ferroelectric Pb(Zr,Ti)O[sub 3] films," *Journal of Applied Physics,* vol. 54, pp. 6601-6609, 1983.

[83] W. W. Grannemann and V. S. Dharmadhikari, "Studif of the Photovoltaic Effect in Thin Film Barium Titanate," The University of New Mexico, Albuquerque, New Mexico EE-273(82)NASA-931-1, January 1982.

[84] M. Ishida, H. Matsunami, and T. Tanaka, "Preparation and properties of ferroelectric PLZT thin films by rf sputtering," *Journal of Applied Physics,* vol. 48, pp. 951-953, 1977.

[85] H. Adachi, T. Mitsuyu, O. Yamazaki, and K. Wasa, "Ferroelectric (Pb,La)(Zr,Ti)O[sub 3] epitaxial thin films on sapphire grown by rf-planar magnetron sputtering," *Journal of Applied Physics,* vol. 60, pp. 736-741, 1986.

[86] H. Fujisawa, K. Kita, M. Shimizu, and H. Niu, "Low-Temperature Fabrication of Ir/Pb(Zr,Ti)O$_{3}$/Ir Capacitors Solely by Metalorganic Chemical Vapor Deposition," *Japanese Journal of Applied Physics,* vol. 40, p. 5551, 2001.

[87] F. Weiss, J. Lindner, J. P. Senateur, C. Dubourdieu, V. Galindo, M. Audier, A. Abrutis, M. Rosina, K. FrÃ¶hlich, W. Haessler, S. Oswald, A. Figueras, and J. Santiso,

"Injection MOCVD: ferroelectric thin films and functional oxide superlattices," *Surface and Coatings Technology,* vol. 133â€“134, pp. 191-197, 2000.

[88] J. F. Roeder, T. H. Baum, S. M. Bilodeau, G. T. Stauf, C. Ragaglia, M. W. Russell, and P. C. Van Buskirk, "Liquid-delivery MOCVD: chemical and process perspectives on ferro-electric thin film growth," *Advanced Materials for Optics and Electronics,* vol. 10, pp. 145-154, 2000.

[89] K. Tominaga, A. Shirayanagi, T. Takagi, and M. Okada, "Switching and Fatigue Characteristics of (Pb, La)(Zr, Ti)O$_{3}$ Thin Films by Metalorganic Chemical Vapor Deposition," *Japanese Journal of Applied Physics,* vol. 32, pp. 4082-4085, 1993.

[90] P. S. Anderson, S. Guerin, B. E. Hayden, M. A. Khan, A. J. Bell, Y. Han, M. Pasha, K. R. Whittle, and I. M. Reaney, "Synthesis of the Ferroelectric Solid Solution, Pb(Zr<inf>1-x</inf>Ti<inf>x</inf>)O<inf>3</inf> on a Single Substrate Using a Modified Molecular Beam Epitaxy (MBE) Technique," in *Applications of Ferroelectrics, 2007. ISAF 2007. Sixteenth IEEE International Symposium on*, 2007, pp. 159-162.

[91] C. D. Theis and D. G. Schlom, "Epitaxial lead titanate grown by MBE," *Journal of Crystal Growth,* vol. 174, pp. 473-479, 1997.

[92] S. Imada, S. Shouriki, E. Tokumitsu, and H. Ishiwara, "Epitaxial Growth of Ferroelectric YMnO$_{\textbf{3}}$ Thin Films on Si (111) Substrates by Molecular Beam Epitaxy," *Japanese Journal of Applied Physics,* vol. 37, pp. 6497-6501, 1998.

[93] K. J. Choi, M. Biegalski, Y. L. Li, A. Sharan, J. Schubert, R. Uecker, P. Reiche, Y. B. Chen, X. Q. Pan, V. Gopalan, L. Q. Chen, D. G. Schlom, and C. B. Eom, "Enhancement of Ferroelectricity in Strained BaTiO3 Thin Films," *Science,* vol. 306, pp. 1005-1009, November 5, 2004 2004.

[94] J. C. Jiang, X. Q. Pan, W. Tian, C. D. Theis, and D. G. Schlom, "Abrupt PbTiO[sub 3]/SrTiO[sub 3] superlattices grown by reactive molecular beam epitaxy," *Applied Physics Letters,* vol. 74, pp. 2851-2853, 1999.

[95] M. P. Warusawithana, C. Cen, C. R. Sleasman, J. C. Woicik, Y. Li, L. F. Kourkoutis, J. A. Klug, H. Li, P. Ryan, L.-P. Wang, M. Bedzyk, D. A. Muller, L.-Q. Chen, J. Levy, and D. G. Schlom, "A Ferroelectric Oxide Made Directly on Silicon," *Science,* vol. 324, pp. 367-370, April 17, 2009 2009.

[96] K.-I. Park, S. Y. Lee, S. Kim, J. Chang, S.-J. L. Kang, and K. J. Lee, "Bendable and Transparent Barium Titanate Capacitors on Plastic Substrates for High Performance Flexible Ferroelectric Devices," *Electrochemical and Solid-State Letters,* vol. 13, pp. G57-G59.

[97] J.-H. Ko, T. H. Kim, K. Roleder, D. Rytz, and S. Kojima, "Precursor dynamics in the ferroelectric phase transition of barium titanate single crystals studied by Brillouin light scattering," *Physical Review B,* vol. 84, p. 094123.

[98] P. Sedykh and D. Michel, "Ferroelectric phase transition in barium titanate nanoparticles," *Physical Review B,* vol. 79, p. 134119, 2009.

[99] Y. Zhang, J. Li, and D. Fang, "Oxygen-vacancy-induced memory effect and large recoverable strain in a barium titanate single crystal," *Physical Review B,* vol. 82, p. 064103.

[100] B. J. Rodriguez, L. M. Eng, and A. Gruverman, "Web-like domain structure formation in barium titanate single crystals," *Applied Physics Letters,* vol. 97, pp. 042902-3.

[101] A. Schilling, D. Byrne, G. Catalan, K. G. Webber, Y. A. Genenko, G. S. Wu, J. F. Scott, and J. M. Gregg, "Domains in Ferroelectric Nanodots," *Nano Letters,* vol. 9, pp. 3359-3364, 2012/05/01 2009.

[102] P. Potnis, N.-T. Tsou, and J. Huber, "A Review of Domain Modelling and Domain Imaging Techniques in Ferroelectric Crystals," *Materials,* vol. 4, pp. 417-447.

[103] G. Collins, D. Elam, R. Hackworth, R. Kotha, A. Ayon, A. Chabanov, and C. Chen, "Pulsed laser deposition (PLD) employed in the fabrication of low temperature barium titanate (BTO) films on carbon fibers," in *Electronics, Communications and Computer (CONIELECOMP), 2010 20th International Conference on*, pp. 23-25.

[104] G. Collins, D. Elam, R. Hackworth, R. Kotha, A. Ayon, A. Chabanov, and C. Chen, "The use of pulsed laser deposition to produce low-temperature barium titanate films on nickel tape and carbon fiber fabric," *Microsystem Technologies,* vol. 17, pp. 701-706.

[105] I. Badro, A. J. Upendra, L. Kyung Hee, and L. Jae Sung, "Growth of single crystalline barium titanate nanowires from TiO 2 seeds deposited on conducting glass," *Nanotechnology,* vol. 21, p. 425601.

[106] Y. Su and J.-N. Du, "Existence conditions for single-vertex structure of polarization in ferroelectric nanoparticles," *Applied Physics Letters,* vol. 95, pp. 012903-3, 2009.

[107] J. Hong, G. Catalan, D. N. Fang, E. Artacho, and J. F. Scott, "Topology of the polarization field in ferroelectric nanowires from first principles," *Physical Review B,* vol. 81, p. 172101.

[108] H. Fu and L. Bellaiche, "Ferroelectricity in Barium Titanate Quantum Dots and Wires," *Physical Review Letters,* vol. 91, p. 257601, 2003.

[109] J. E. Spanier, A. M. Kolpak, J. J. Urban, I. Grinberg, L. Ouyang, W. S. Yun, A. M. Rappe, and H. Park, "Ferroelectric Phase Transition in Individual Single-Crystalline BaTiO3 Nanowires," *Nano Letters,* vol. 6, pp. 735-739, 2012/05/02 2006.

[110] G. H. Kwei, A. C. Lawson, S. J. L. Billinge, and S. W. Cheong, "Structures of the ferroelectric phases of barium titanate," *The Journal of Physical Chemistry,* vol. 97, pp. 2368-2377, 2012/05/02 1993.

[111] H. F. Kay and P. Vousden, "Symmetry Changes in Barium Titanate at Low Temperatures and Their Relation to Its Ferroelectric Properties," *Philosophical Magazine,* vol. 40, pp. 1019-1040, 1949.

[112] K. Momma and F. Izumi, "VESTA 3 for three-dimensional visualization of crystal, volumetric and morphology data," *Journal of Applied Crystallography,* vol. 44, pp. 1272-1276.

[113] D. Dragan, "The Science of Hysteresis." vol. 3, G. Bertotti and I. D. Mayergoyz, Eds.: Elsevier Science, 2006, pp. 337-465.

[114] A. von Hippel, "Ferroelectricity, Domain Structure, and Phase Transitions of Barium Titanate," *Reviews of Modern Physics,* vol. 22, pp. 221-237, 1950.

[115] H. Diamant, K. Drenck, and R. Pepinsky, "Bridge for Accurate Measurement of Ferroelectric Hysteresis," *Review of Scientific Instruments,* vol. 28, pp. 30-33, 1957.

[116] Y. T. Tsui, P. D. Hinderaker, and F. J. McFadden, "New Ferroelectric Hysteresis Curve Tracer Featuring Compensation and Virtual Sample Grounding," *Review of Scientific Instruments,* vol. 39, pp. 1423-1424, 1968.

[117] A. Grigoriev, M. M. Azad, and J. McCampbell, "Ultrafast electrical measurements of polarization dynamics in ferroelectric thin-film capacitors," *Review of Scientific Instruments,* vol. 82, pp. 124704-5.

[118] J. F. Ihlefeld, W. J. Borland, and J. P. Maria, "Enhanced Dielectric and Crystalline Properties in Ferroelectric Barium Titanate Thin Films," *Advanced Functional Materials,* vol. 17, pp. 1199-1203, 2007.

[119] J. T. Dawley and P. G. Clem, "Dielectric properties of random and <100> oriented SrTiO[sub 3] and (Ba,Sr)TiO[sub 3] thin films fabricated on <100> nickel tapes," *Applied Physics Letters,* vol. 81, pp. 3028-3030, 2002.

[120] B. Lewis, "Energy Loss Processes in Ferroelectric Ceramics," *Proceedings of the Physical Society,* vol. 73, p. 17, 1959.

[121] J. R. Arthur, "Molecular beam epitaxy," *Surface Science,* vol. 500, pp. 189-217, 2002.

[122] J. J. R. Arthur, "Interaction of Ga and As[sub 2] Molecular Beams with GaAs Surfaces," *Journal of Applied Physics,* vol. 39, pp. 4032-4034, 1968.

[123] J. L. Vossen and W. Kern, *Thin Film Processes II*: Academic Press, 1991.

[124] C. T. Foxon, "Three decades of molecular beam epitaxy," *Journal of Crystal Growth,* vol. 251, pp. 1-8, 2003.

[125] M. Naito, H. Yamamoto, and H. Sato, "Reflection high-energy electron diffraction and atomic force microscopy studies on homoepitaxial growth of SrTiO3(001)," *Physica C: Superconductivity,* vol. 305, pp. 233-250, 1998.

[126] Z. Yu, Y. Liang, C. Overgaard, X. Hu, J. Curless, H. Li, Y. Wei, B. Craigo, D. Jordan, R. Droopad, J. Finder, K. Eisenbeiser, D. Marshall, K. Moore, J. Kulik, and P. Fejes,

"Advances in heteroepitaxy of oxides on silicon," *Thin Solid Films,* vol. 462â€“463, pp. 51-56, 2004.

[127] J. H. Haeni, C. D. Theis, and D. G. Schlom, "RHEED Intensity Oscillations for the Stoichiometric Growth of SrTiO₃ Thin Films by Reactive Molecular Beam Epitaxy," *Journal of Electroceramics,* vol. 4, pp. 385-391, 2000.

[128] M. B. Panish, "Molecular Beam Epitaxy," *Science,* vol. 208, pp. 916-922, May 23, 1980 1980.

[129] B. A. Joyce, "Molecular beam epitaxy," *Reports on Progress in Physics,* vol. 48, p. 1637, 1985.

[130] S. P. Minor, "Plasma-Assisted Molecular Beam Epitaxial Growth of Indium Nitride for Future Device Fabrication," in *ProQuest Dissertations and Theses* United States -- Arkansas: University of Arkansas.

[131] C. Xumin, Y. Seolun, K. Ji-Hyun, K. Hyung-Do, K. Jae-Sung, R. Geoffrey, S. Ralph, L. Haidong, B. Anand, S. Tiffany, G. Nathan, B. Matthias, G. Alexei, and E. Axel, "Ultrathin BaTiO 3 templates for multiferroic nanostructures," *New Journal of Physics,* vol. 13, p. 083037.

[132] M. J. Dicken, K. Diest, Y.-B. Park, and H. A. Atwater, "Growth and optical property characterization of textured barium titanate thin films for photonic applications," *Journal of Crystal Growth,* vol. 300, pp. 330-335, 2007.

[133] T. Tsurumi, T. Suzuki, M. Yamane, and M. Daimon, "Fabrication of Barium Titanate/Strontium Titanate Artificial Superlattice by Atomic Layer Epitaxy," *Japanese Journal of Applied Physics,* vol. 33, pp. 5192-5195, 1994.

[134] W. Braun, *Applied Rheed: Reflection High-Energy Electron Diffraction During Crystal Growth*: Springer, 1999.

[135] Y. Yoneda, K. Sakaue, and H. Terauchi, "RHEED observation of BaTiO3 thin films grown by MBE," *Surface Science,* vol. 529, pp. 283-287, 2003.

[136] C. A. Gogol, "Rate controlling and composition analysis of Si/Al--Si processes by electron impact emission spectroscopy (EIES)," *Journal of Vacuum Science and Technology,* vol. 16, pp. 884-887, 1979.

[137] Y. Yoneda, K. Sakaue, and H. Terauchi, "Dielectric Investigation of BaTiO₃ Thin-Film Capacitor," *Japanese Journal of Applied Physics,* vol. 39, pp. 4839-4842, 2000.

[138] H. F. Kay and P. Vousden, "XCV. Symmetry changes in barium titanate at low temperatures and their relation to its ferroelectric properties," *Philosophical Magazine Series 7,* vol. 40, pp. 1019-1040, 2012/08/07 1949.

[139] A.-B. Posadas, M. Lippmaa, F. Walker, M. Dawber, C. Ahn, and J.-M. Triscone, "Growth and Novel Applications of Epitaxial Oxide Thin Films

Physics of Ferroelectrics." vol. 105: Springer Berlin / Heidelberg, 2007, pp. 219-304.

[140] H.-U. Habermeier, "Thin films of perovskite-type complex oxides," *Materials Today,* vol. 10, pp. 34-43, 2007.

[141] H. M. Smith and A. F. Turner, "Vacuum Deposited Thin Films Using a Ruby Laser," *Appl. Opt.,* vol. 4, pp. 147-148, 1965.

[142] D. H. Lowndes, D. B. Geohegan, A. A. Puretzky, D. P. Norton, and C. M. Rouleau, "Synthesis of Novel Thin-Film Materials by Pulsed Laser Deposition," *Science,* vol. 273, pp. 898-903, August 16, 1996 1996.

[143] D. P. Norton, "Pulsed Laser Deposition of Complex Materials: Progress Towards Applications," in *Pulsed Laser Deposition of Thin Films: Applications-Led Growth of Functional Materials*, R. Eason, Ed.: Wiley-Interscience, 2006, pp. 3-32.

[144] P. D. Davidse and L. I. Maissel, "Dielectric Thin Films through rf Sputtering," *Journal of Applied Physics,* vol. 37, pp. 574-579, 1966.

[145] Y. W. Chung, *Introduction to Materials Science and Engineering*: Taylor & Francis, 2006.

[146] I. H. Pratt, "Characteristices of RF Spttered Barium Titanate Thin Films," *Proceedings of the IEEE,* vol. 59, p. 1440, 1971.

[147] S. Mahieu, W. P. Leroy, D. Depla, S. Schreiber, and W. Moller, "Noble gas retention in the target during rotating cylindrical magnetron sputtering," *Applied Physics Letters,* vol. 93, pp. 061501-3, 2008.

[148] S.-T. Lee, N. Fujimura, and T. Ito, "Epitaxial Growth of BaTiO3 Thin Films and Thier Internal Stresses," *Japanese Journal of Applied Physics,* vol. 34, p. 5168, 1995.

[149] R. Vu Huy Dat and C. Baumberger, "Ferroelectricity of Barium Titanate Thin Films of less than One Micron Thickness," *physica status solidi (b),* vol. 22, pp. K67-K70, 1967.

[150] S. K. Young, "Overview of Sol-Gel Science and Technology," A. R. Laboratory, Ed. Aberdeen Proving Ground, MD, 2002.

[151] L. L. Hench and J. K. West, "The sol-gel process," *Chemical Reviews,* vol. 90, pp. 33-72, 2012/06/26 1990.

[152] R. D. Levi, S. Trolier-McKinstry, and C. A. Randall, "High voltage dielectric properties of spin coated BaTiO3 on Ni foils," in *Applications of Ferroelectrics, 2008. ISAF 2008. 17th IEEE International Symposium on the*, 2008, pp. 1-3.

[153] I. P. Koutsaroff, A. Kassam, M. Zelner, P. Woo, L. McNeil, T. Bernacki, A. Cervin-Lawry, and A. Patel, "Dielectric Properties of (Ba,Sr)TiO3 Thin Film Capacitors Fabricated on Alumina Substrates," in *Materials Research Society*, Boston, MA, 2003.

[154] F. M. Pontes, C. D. Pinheiro, E. Longo, E. R. Leite, S. R. de Lazaro, R. Magnani, P. S. Pizani, T. M. Boschi, and F. Lanciotti, "Theoretical and experimental study on the

photoluminescence in BaTiO3 amorphous thin films prepared by the chemical route," *Journal of Luminescence,* vol. 104, pp. 175-185, 2003.

[155] C. J. Powell and A. Jablonski, "Progress in quantitative surface analysis by X-ray photoelectron spectroscopy: Current status and perspectives," *Journal of Electron Spectroscopy and Related Phenomena,* vol. 178â€“179, pp. 331-346.

[156] A. Jablonski, "Quantitative Surface Analysis by X-ray Photoelectron Spectroscopy," *Polish Journal of Chemistry,* vol. 74, pp. 1533-1566, 2000.

[157] K. Sugawara, H. Sakusabe, T. Nishino, T. Sugawara, K.-j. Ogiwara, and J. S. Dranoff, "Thermal decomposition of barium titanate precursor prepared by a wet chemical method," *AIChE Journal,* vol. 43, pp. 2837-2843, 1997.

[158] T.-I. Chang, S.-C. Wang, C.-P. Liu, C.-F. Lin, and J.-L. Huang, "Thermal Behaviors and Phase Evolution of Lead Zirconate Titanate Prepared by Sol–Gel Processing: The Role of the Pyrolysis Time before Calcination," *Journal of the American Ceramic Society,* vol. 91, pp. 2545-2552, 2008.

[159] P. K. Sehdar, "Process development and characterization of sol-gel lead zirconate titanate films for fabriaction of flexural plate wave devices," in *Department of Electrical Engineering*. vol. Master of Science Tampa, Florida: University of South Florida, 2005, p. 67.

[160] S. M. Aygun and U. North Carolina State, *Processing Science of Barium Titanate*: North Carolina State University, 2009.

[161] T. M. Stawski, W. J. C. Vijselaar, O. F. GÃ¶bel, S. A. Veldhuis, B. F. Smith, D. H. A. Blank, and J. E. ten Elshof, "Influence of high temperature processing of solâ€“gel derived barium titanate thin films deposited on platinum and strontium ruthenate coated silicon wafers," *Thin Solid Films,* vol. 520, pp. 4394-4401.

[162] J. O. Braithwaite, *Yearbook of Pharmacy: Comprising Abstracts of Papers Relating to Pharmacy, Materia Medica and Chemistry Contributed to British and Foreign Journal...with the Transactions of the British Pharmaceutical Conference*: J. & A. Churchill, 1895.

[163] T. Mouganie, M. Moram, J. Sumner, B. Glowacki, B. Schoofs, I. Driessche, and S. Hoste, "Chemical and Physical Analysis of Acetate-Oxide Sol-Gel Processing Routes for the Y-Ba-Cu-O System," *Journal of Sol-Gel Science and Technology,* vol. 36, pp. 87-94, 2005.

[164] T. B. Reed, *Free Energy of Formation of Binary Compounds: An Atlas of Charts for High-temperature Chemical Calculations*: Biomass Energy Foundation Press, 2000.

[165] J. R. Davis, *Metals Handbook Desk Edition 2nd Edition*: Taylor & Francis, 1998.

[166] H. Kishimoto, K. Yamaji, M. E. Brito, T. Horita, and H. Yokokawa, "Generalized Ellingham Diagrams for Utilization in Solid Oxide Fuel Cells," *Journal of Mining and Metallurgy, Section B: Metallurgy,* vol. 44, pp. 39-48, 2008.

[167] W. C. Bosshart, *Printed Circuit Boards: Design and Technology*: Tata McGraw-Hill, 1983.

[168] "Inductors for Decoupling Circuits: Multilayer/STD magnetic shielded MLZ series," TDK, 2012.

Appendix A: Description of Research for Popular Publication

A potentially major breakthrough concerning the development ultrafast communications has been recently been made by a Rob Sleezer, a researcher at the University of Arkansas. His work involves the reshaping of electrical pulses as they propagate along an artificial transmission line. Applications of such transmission lines could lead to performance improvements in cellular phones, laptop computers, wireless networks, and possibly even voltage converters.

The transmission line that was developed by Sleezer is a relatively small line that would be more likely to connect integrated circuits on a printed circuit board than to deliver power to houses. The pulse shaping is very similar to the way waves are reshaped as they move along a beach. Using a water wave as an example, the sharpening is caused by the bottom part of the wave encountering the sand and slowing down. When this happens, the peak of the wave, which is now moving faster, stacks up on the front of the wave and the rising edge of the wave sharpens. The big difference between the water waves on a beach example and the electrical pulses in the nonlinear transmission line is that instead of slowing down the bottom of the pulse the nonlinear transmission line speeds up the top of the pulse.

It does this by exploiting a class of materials known as ferroelectrics. You may be familiar with ferromagnets such as iron or nickel. These are materials which orient themselves to magnetic fields. If you put them in a magnetic field of sufficient strength they will become magnetically polarized even when removed from the magnetic field. Likewise if you put a ferroelectric into an electric field of sufficient strength the ferroelectric will become electrically polarized even when removed from the electric field. One of the results of this effect is that the ferroelectric material responds more quickly to higher electric fields.

Transmission lines made using ferroelectric materials have been previously made and have shown that the pulse sharpening described above does occur. The lines constructed previously were built with bricks of ferroelectric material about 1cm thick that required many kilovolts of potential to create a sufficient electric field to operate. Obviously such voltages are not found in consumer level devices. Therefore, if a nonlinear line is going to be used in such devices something must be done to reduce the voltage required for operation. The line constructed by Sleezer uses ferroelectric thin films that are only a few hundred nanometers thick. With such a thin material a much smaller voltage is required to exploit the nonlinear behavior of the transmission line.

Unfortunately, the constructed transmission line is not a continuous line but rather a series of capacitors and inductors put together in such a way as to create an artificial transmission line. This means that, while it is not the size of the lines created several years ago it is still relatively large. As a result it will not be possible to immediately integrate the line into consumer electronic applications. Additional work must be done to make the line continuous and monolithic. Despite these issues, this step represents a potentially substantial step forward for consumer communications technologies.

Appendix B: Executive Summary of Newly Created Intellectual Property

A concise numbered list of the major new IP created during the research presented in this dissertation.

1. A Process to Cold Weld Ferroelectric Capacitors
2. Design and Fabrication of a Discrete Thin Film Ferroelectric Transmission Line
3. Lossy transmission line simulation algorithm
4. Dispersive transmission line simulation algorithm

Appendix C: Potential Patent and Commercialization Aspects of each Numbered Item in Appendix B

1. The cold welded ferroelectric capacitors can be patented

2. The discrete thin film ferroelectric line can be patented

3. The lossy transmission line simulation algorithm cannot be patented due to publication

4. The dispersive transmission line simulation algorithm can be patented

Commercialization Possibilities

1. The cold welded ferroelectric capacitor should be patented if an entity can be found which wants to license the technology. At the time of writing the cold welded ferroelectric capacitor had been unsuccessfully marketed.

2. The discrete thin film ferroelectric line is likely to be too large and cumbersome to be of any value. Therefore, it is recommended that no effort be made to pursue a patent.

3. Discussing the patenting of the lossy transmission line simulation is pointless because it cannot be patented.

4. The dispersive transmission line simulation algorithm is not likely to have broader applications so it is not recommended that an effort be made to pursue a patent.

Prior Disclosure

1. There has been no known disclosure of the cold welded ferroelectric capacitors.

2. There have been other nonlinear transmission lines discussed in the literature. No publications or patents are known that would cause a problem with the patenting of this device.

3. The lossy transmission line simulation algorithm was presented at The 2009 Villa Conference on Complex Oxides Heterostructures.

4. There has been no known disclosure of the dispersive transmission line simulation algorithm. There are no known patents that would obstruct the progress of this intellectual property.

Appendix D: Broader Impact

Applicability of research methods to other problems

This research has applications specific impacts to the ferroelectric effort of Greg Salamo's group at the University of Arkansas. Specifically they are to ramp up on technologies used to test and evaluate ferroelectric materials as well as the development of test both coplanar and parallel plate test structures. Outside the specific research group, the algorithms created as part of this effort could be used in other research involving lossy dispersive systems.

Impact of research on the US and global economy

This research is not expected to have any direct impact on the US or the global economy. It is possible that if the research is extended it could have high end applications including military and space uses. It is likely that implementation of the technology resulting from this work would be too costly for consumer applications in the near and midterm time scale.

Appendix E: Microsoft Project Printout of Research Project Plan

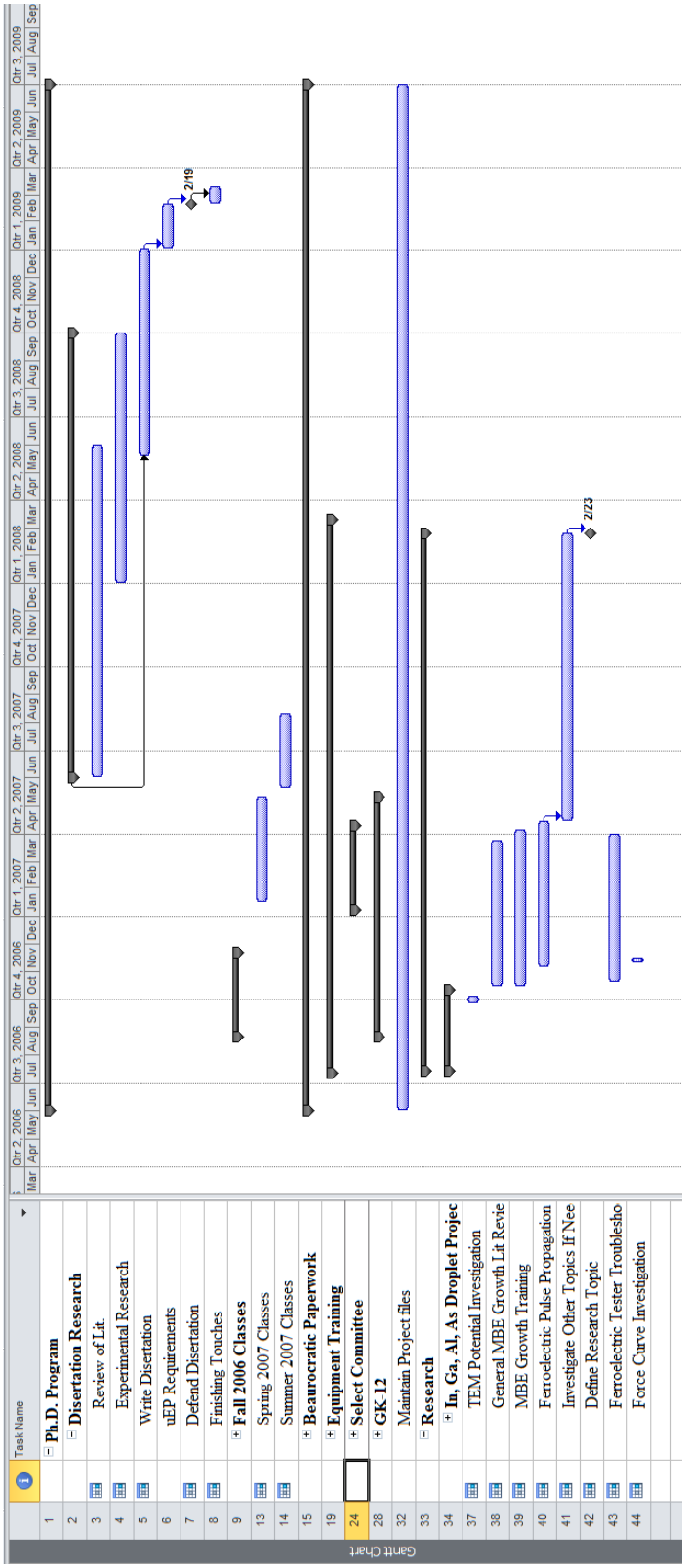

Appendix F: Identification of All Software Used in Research and Dissertation for Each Computer Used

Computer #1:

Model Number and Serial Number: T5400, No serial number found

Location: Physics 129

Owner: University of Arkansas

Software #1:	Software #2:	Software #3
Name: M.S. Office	Name: Origin	Name: Matlab
Purchased by: UA	Purchased by: UA	Purchased by: UA
License #: 02260-018-0000106-48978	License #: GF3S4-9489-7603011	License #: 601103

Software #4:	Software #5:
Name: End Note	Name: M.S. Visual Studio
Purchased by: Student	Purchased by: Student
License #: 5221102063	License #: 01018-573-8075886-70407

Computer #2:

Model Number and Serial Number: E5510, No serial number found

Location: Unknown

Owner: Student

Software #1:	Software #2:
Name: M.S. Office	Name: End Note
Purchased by: UA	Purchased by: Student
License #: 02260-018-	License #: 5221102063

0000106-48978

Computer #3:

Model Number and Serial Number: Various UA computers I was told not to worry about during uEP orientation.

Location: Unknown

Owner: UA

Software #1:	Software #2:
Name: M.S. Office	Name: Matlab
Purchased by: UA	Purchased by: UA
License #: Unknown	License #: Unknown

Appendix G: All Publications Pertaining to Research Published, Submitted, or Planned

R. Sleezer, Z. Zeng, J. Krasinski, and G. Salamo, "Revisiting Oxide Based Nonlinear Transmission Lines," The 2009 Villa Conference on Complex Oxides Heterostructures, St. Thomas, U.S. Virgin Islands, US, 13-18 September, 2009. [Presented by **R. Sleezer**.]

Appendix H: C++ Code for Simulations

```
// RK4test.cpp : Defines the entry point for the console application.
//


#include "stdafx.h"


using namespace std;


double Cdx(double V);

double dCdV(double V);

void propagate(long N_in, double dt_in, double t_in, double ep_in, double Cbase_in, double Rsbase_in, double Rpbase_in, double Rcbase_in, double L_in, double Vmax_in, int signal_type_in, double pulse_len_in, long print_frac_in, string o_file, string hdr_file, double f_factor, double maxLoss, long no_filters, double dispFrac);


void feval(int n, double t, double** y, double* dydt);

void RK4stp(int n, int N, double t, double** yode, double* ak0, double* ak1, double* ak2, double* ak3, double h, double* dydt, double** ytemp);
```

```
long loc = 0;  //global variables used instead of redeclaring in each subroutine

long loc2 = 0;

double C_base = 0;  //global variable used instead of redeclaring in each subroutine base conductance

double Ldx = 0;  //global variable used instead of redeclaring in each subroutine,

double dCdV_curr = 0; //global variable used instead of redeclaring in each subroutine

double Cdx_curr = 0; //global variable used instead of redeclaring in each subroutine

double Cdx_prev = 0; //global variable used instead of redeclaring in each subroutine

double Rsdx = 2718; //global variable used instead of redeclaring in each subroutine

double Rpdx = 0;  //global variable used instead of redeclaring in each subroutine

double Rcdx = 0;  //global variable used instead of redeclaring in each subroutine


double C_nl = 0; //global variable for forcing the nonlinearity to be linear the third input will be put here


int main(int argc, char* argv[])

{
```

```
long runs;

long N;

double dt;

double t;

double ep;

double Cbase_loc;

double Rsbase;

double L;

double Rpbase;

double Rcbase;

double Vmax;

double f_factor;

double pulse_len;

int signal_type;

long print_frac;

double maxLoss;

long no_filters;
```

```
double dispFrac;

char o_file[64];

char hdr_file[64];



for (int s = 0; s<64; s++)

        o_file[s] = 0;

cout<<"Input file 1: "<<o_file<<endl;



cin>>o_file;

cout<<"Input file 2: "<<o_file<<endl;

ifstream fin(o_file,ios::in);

cout<<"Input file 3: "<<o_file<<endl;



fin>>runs;

cout<<"RUNS: "<<runs<<endl;



for (int i = 0; i<runs; i++)
```

```
{
        fin>>N;
        fin>>dt;
        fin>>f_factor;
        fin>>t;
        fin>>ep;
        fin>>Cbase_loc;
        fin>>Rsbase;
        fin>>Rpbase;
        fin>>Rcbase;
        fin>>L;
        fin>>Vmax;
        fin>>signal_type;
        fin>>pulse_len;
        fin>>print_frac;
        fin>>maxLoss;
        fin>>no_filters;
```

```
                fin>>dispFrac;

                fin>>o_file;



                strcpy(hdr_file, o_file);

                strcat(hdr_file, "_hdr.txt");

                strcat(o_file, ".txt");



        //=================================================================
=======================================

                C_nl = f_factor;

        //=================================================================
=======================================


                cout<<"hdr:"<<hdr_file<<" o:"<<o_file<<endl;

        cout<<N<<'\t'<<dt<<'\t'<<f_factor<<'\t'<<t<<'\t'<<ep<<'\t'<<Cbase_loc<<'\t'<<Rsbase<<
```

```
'\t'<<Rpbase<<'\t'<<Rcbase<<'\t'<<'L'<<L<<'\t'<<Vmax<<'\t'<<"type:"<<signal_type<<'\t'<<pul
se_len<<'\t'<<print_frac<<'\t'<<o_file<<'\t'<<hdr_file<<endl;

        propagate(N,dt,t,ep,Cbase_loc,Rsbase,Rpbase,Rcbase,L,Vmax,signal_type,pulse_len,prin
t_frac,o_file,hdr_file,f_factor,maxLoss,no_filters,dispFrac);

                }


                fin.close();


                return 0;

        }


        void propagate(long N_in, double dt_in, double t_in, double ep_in, double Cbase_in,
double Rsbase_in, double Rpbase_in, double Rcbase_in, double L_in, double Vmax_in, int
signal_type_in, double pulse_len_in, long print_frac_in, string o_file, string hdr_file, double
f_factor, double maxLoss, long no_filters, double dispFrac)

        {

                char dummy;

                bool tmr = true; //enable the output counter
```

```
long percent_done = 0; //The simulation is currently not started


double c = 3.0*pow(double(10),8); //speed of light

double pi = 3.1415926535897932385;


double L = L_in; //length of the line

long N = N_in;  //number of nodes

double t = t_in; //time of the simulation


double ep = ep_in; //epsilon of the dielectric material

double Cm_base = Cbase_in;  //capactance of 1 meter of the line with ep = 1 in F

double Lm = 1/(pow(c,2)*Cm_base);  //inductance of 1 meter of the line in H

double Cdx_base = Cm_base*L/N;  //capacitance of the line per unit step in C

Ldx = Lm*L/N; //inductance of the line per unit step in H

Rpdx = Rpbase_in*L/N;  //shunt resistance of the line per unit step in ohms

Cdx_curr = 0;  //voltage dependent capacitance

dCdV_curr = 0;  //derivative of capacitance with respect to voltage at the current
node and time
```

```
Cdx_prev = 0;  //voltage dependant capacitance at previous node

double Rsm = Rsbase_in; //series resistance of 1 meter of the line in Ohms (for a
.5mm wide .5um thick line of Au the value is 1e-2)

Rsdx = Rsm*L/double(N);  //series Resistance of the line per unit step in Ohms

Rcdx = Rcbase_in*L/N;



double curr_t = 0;  //current time in the simulation

long stepOverCnt = 0; //the number of step overs in simulation



double dt = dt_in; //time step in sumplation

long no_t = long(ceil(t/dt));  //number of time steps

cout<<"no_t: "<<no_t<<endl;

double *p_t_arr = new double[no_t]; //set asside the space for the time array

//=============================================================
==========================================================

//=============================================================
==========================================================
```

```
//The Ldx below is for a specific test of a discrete transmission line and should be
removed before
//any general simulation are run. Leaving this WILL RESULT IN AN ERROR
//=============================================================
==========================================
//=============================================================
==========================================================
//Ldx = 1.47e-6;
//=============================================================
==========================================================
//=============================================================
==========================================================
//The Ldx above is for a specific test of a discrete transmission line and should be
removed before
//any general simulation are run. Leaving this WILL RESULT IN AN ERROR
//=============================================================
==========================================
//=============================================================
==========================================================
```

```
if (p_t_arr == 0)

{

        cout<<"memory error"<<endl;

        cin>>dummy;

        exit(0);

}



C_base = Cdx_base*ep;



double **p_Y = new double* [2];

p_Y[0] = new double[N+2]+1;

p_Y[1] = new double[N+2]+1;



if (p_Y[0] == 0 || p_Y[1] == 0 )        {

        cout<<"memory error"<<endl;

        cin>>dummy;
```

```
        exit(0);
}

long Nt = 256;
double **p_y_buff = new double* [N];
for (int i = 0; i<N; i++)
{
        p_y_buff[i] = new double[Nt];
        if (p_y_buff[i] == 0) {
                cout<<"memory error"<<endl;
                cin>>dummy;
                exit(0);
        }
}

double *p_t_buff = new double[Nt];
if (p_t_buff == 0) {
```

```
        cout<<"memory error"<<endl;
        cin>>dummy;
        exit(0);
}

for (int i = 0; i<N; i++)
        for(int j = 0; j<Nt; j++)
                p_y_buff[i][j] = 0;

fftw_complex* t_filter;
fftw_complex* t_signal;
fftw_complex* t_fft;
fftw_complex* t_signal2;
fftw_complex* t_fft2;

t_filter = (fftw_complex*)fftw_malloc(sizeof(fftw_complex)*Nt);
t_signal = (fftw_complex*)fftw_malloc(sizeof(fftw_complex)*Nt);
```

```
t_fft = (fftw_complex*)fftw_malloc(sizeof(fftw_complex)*Nt);

t_signal2 = (fftw_complex*)fftw_malloc(sizeof(fftw_complex)*Nt);

t_fft2 = (fftw_complex*)fftw_malloc(sizeof(fftw_complex)*Nt);



for (int i = 0; i<Nt; i++)

{

    t_filter[0][i] = t_filter[1][i] = 0;

    t_signal[0][i] = t_signal[1][i] = 0;

    t_signal2[0][i] = t_signal2[1][i] = 0;

}

fftw_plan fft_t_forward;

fftw_plan fft_t_backward;



fft_t_forward =
fftw_plan_dft_1d(Nt,t_signal,t_fft,FFTW_FORWARD,FFTW_ESTIMATE);

fft_t_backward =
fftw_plan_dft_1d(Nt,t_fft2,t_signal2,FFTW_BACKWARD,FFTW_ESTIMATE);
```

```
/* The filter represents the dielectric losses in the system (the loss tangent). A triangular filter is used to approximate the losses

based on several papers. Also, the losses were shown to be fairly linear up to 10GHz in work by Xinen Zhu. This is published in a

Ph.D. dissertation titled "Switchable and Tunable Ferroelectric Thin Film Radio Frequency Components" written in 2009 at The

University of Michigan. This filter might be fair because it is applied to inverse time.*/


if (Nt%2==1)

        t_filter[Nt/2][0]=t_filter[Nt/2][1]=max(1.0-maxLoss,0.0);

for (int m = 0; m<Nt/2; m++)

        if ((1-(double)m*maxLoss/(double)Nt)>0)

                t_filter[m][0]=t_filter[Nt-1-m][0]=t_filter[m][1]=t_filter[Nt-1-m][1]=1-(double)m*maxLoss/(double)Nt;

        else

                t_filter[m][0]=t_filter[Nt-1-m][0]=t_filter[m][1]=t_filter[Nt-1-m][1]=0;
```

```
double **p_Ytemp = new double* [2];

p_Ytemp[0] = new double[N+2]+1;

p_Ytemp[1] = new double[N+2]+1;



if (p_Ytemp[0] == 0 || p_Ytemp[1] == 0 )     {

        cout<<"memory error"<<endl;

        cin>>dummy;

        exit(0);

}



long filter_frac;

bool filter_flag = true;

if (no_filters == 0)

{

        filter_frac = -99;

        filter_flag = false;

}
```

```
else
        filter_frac = no_t/no_filters;
fftw_complex* filter;
fftw_complex* signal;
fftw_complex* signal_fft;
fftw_complex* phase_shift;

int C_space = 100; //This is used to adjust the electrical distance of a FE so the FFT is fair
int* C_electrical_dist = new int[N];
double* wave_vect = new double[N*C_space];
double C0 = Cdx(0);
int c_pos_ctr = 0;

signal = (fftw_complex*)fftw_malloc(sizeof(fftw_complex)*(N)*C_space);
signal_fft = (fftw_complex*)fftw_malloc(sizeof(fftw_complex)*(N)*C_space);
filter = (fftw_complex*)fftw_malloc(sizeof(fftw_complex)*(N)*C_space);
phase_shift = (fftw_complex*)fftw_malloc(sizeof(fftw_complex)*(N)*C_space);
```

```
double* dispersion = new double[N*C_space];  //This is the frequency dependant
dispersion


for (int i = 0; i<N*C_space/2; i++)
{
	wave_vect[i] = i;
}
for (int i = N*C_space/2; i<N*C_space; i++)
{
	wave_vect[i] = N*C_space-i-1;
}


//==========================Move to input
file=============================================================================
====================

double dispersion_fraction = dispFrac; //This is the dispersion in the system
should probably be moved to input file. It is not yet tied to anything meaningful but the higher
the value the more the dispersion
```

```
//============================Move to input
file=================================================================
==================

/* The filter represents the dielectric losses in the system (the loss tangent). A
triangular filter is used to approximate the losses

based on several papers. Also, the losses were shown to be fairly linear up to
10GHz in work by Xinen Zhu. This is published in a

Ph.D. dissertation titled "Switchable and Tunable Ferroelectric Thin Film Radio
Frequency Components" written in 2009 at The

University of Michigan. This filter is not fair because it is applied to inverse space
not inverse time.*/


if (N%2==1)

        filter[N/2][0]=filter[N/2][1]=max(1.0-maxLoss,0.0);

for (int m = 0; m<N/2; m++)

        if ((1-(double)m*maxLoss/(double)N)>0)

                filter[m][0]=filter[N-1-m][0]=filter[m][1]=filter[N-1-m][1]=1-
(double)m*maxLoss/(double)N;
```

```
            else
                    filter[m][0]=filter[N-1-m][0]=filter[m][1]=filter[N-1-m][1]=0;
            /*
            int cut_off = N/4;
            for (int m = 0; m<N/2-cut_off; m++)
            filter[m][0]=filter[N-1-m][0]=filter[m][1]=filter[N-1-m][1]=1;
            for (int m = N/2-cut_off; m<N/2; m++)
            filter[m][0]=filter[N-1-m][0]=filter[m][1]=filter[N-1-m][1]=0;
            if(N%2==1)
            filter[N/2][0]=filter[N/2][1]=0;

            if (N%2==1)
            filter[N/2][0]=filter[N/2][1]=0;
            for (int m = 0; m<N/2; m++)
            filter[m][0]=filter[N-1-m][0]=filter[m][1]=filter[N-1-m][1]=pow(2.718281828,-
20/(double)(N/2-m));

            maxLoss = 0.9;
```

```
cut_off = N/4;

if (N%2==1)

filter[N/2][0]=filter[N/2][1]=1-maxLoss;

for (int m = 0; m<cut_off; m++)

filter[m][0]=filter[N-1-m][0]=filter[m][1]=filter[N-1-m][1]=1;

for (int m = cut_off; m<N/2; m++)

filter[m][0]=filter[N-1-m][0]=filter[m][1]=filter[N-1-m][1]=1-(double)(m-
cut_off)*maxLoss*2/(double)(N-cut_off*2);



double slope = 0.005;

double position = 800;

if (N%2==1)

filter[N/2][0]=filter[N/2][1]=0;

for (int m = 0; m<N/2; m++)

filter[m][0]=filter[N-1-m][0]=filter[m][1]=filter[N-1-m][1]=1-
1/(1+pow(2.718281828,(slope*(-m+position))));



double sigma = 1000;
```

```
if (N%2==1)

filter[N/2][0]=filter[N/2][1]=0;

for (int m = 0; m<N/2; m++)

filter[m][0]=filter[N-1-m][0]=filter[m][1]=filter[N-1-m][1]=pow(2.718281828,(-
m*m/(2*sigma*sigma)));

*/

fftw_plan fft_V_forward;

fftw_plan fft_V_backward;



fft_V_forward = fftw_plan_dft_1d(N*C_space, signal, signal_fft,
FFTW_FORWARD, FFTW_ESTIMATE);

fft_V_backward = fftw_plan_dft_1d(N*C_space, signal_fft, signal,
FFTW_BACKWARD, FFTW_ESTIMATE);



if (signal==0 || signal_fft==0 || filter ==0) {

    cout<<"memory error"<<endl;

    cin>>dummy;

    exit(0);
```

```
}

double *p_dydt = new double[2];

double* ak0 = new double[N];
double* ak1 = new double[N];
double* ak2 = new double[N];
double* ak3 = new double[N];

if(ak0 == 0 || ak1 == 0 || ak2 == 0 || ak3 == 0)
{
        cout<<"memory error"<<endl;
        cin>>dummy;
        exit(0);
}

long loc10 = long(floor(N*0.1));
```

```
long loc20 = long(floor(N*0.2));

long loc30 = long(floor(N*0.3));

long loc40 = long(floor(N*0.4));

long loc50 = long(floor(N*0.5));

long loc60 = long(floor(N*0.6));

long loc70 = long(floor(N*0.7));

long loc80 = long(floor(N*0.8));

long loc90 = long(floor(N*0.9));



double Vmax = Vmax_in;

double pulse_len = pulse_len_in;

cout<<"test 1: "<<no_t<<endl;

double *p_Vs = new double[no_t];

cout<<"test 2"<<endl;

long pulse_end = long(floor(no_t*pulse_len));

cout<<"test 3"<<endl;
```

```
if (p_Vs == 0)
{
	cout<<"memory error";
	cin>>dummy;
	exit(1);
}

const char *p_o_name = o_file.c_str();

ofstream outMain(p_o_name,ios::out|ios::trunc);

if(!outMain.is_open())
{
	cout<<"output file error"<<endl;
	cin>>dummy;
	exit(0);
}
```

```
ofstream outFull("full.txt",ios::out|ios::trunc);


if(!outFull.is_open())
{
        cout<<"output file error"<<endl;
        cin>>dummy;
        exit(0);
}


const char *p_hdr_name = hdr_file.c_str();


ofstream outHdr(p_hdr_name,ios::out|ios::trunc);


if(!outHdr.is_open())
{
        cout<<"output file error"<<endl;
```

```
        cin>>dummy;
        exit(0);
}

ofstream outFFT("fftOut.txt",ios::out|ios::trunc);

if(!outFFT.is_open())
{
        cout<<"output file error"<<endl;
        cin>>dummy;
        exit(0);
}
ofstream outV("VOut.txt",ios::out|ios::trunc);

if(!outV.is_open())
{
        cout<<"output file error"<<endl;
```

```
        cin>>dummy;

        exit(0);

}


for (double Volts = -1; Volts<2; Volts = Volts + 0.1){

        outV<<Volts<<'\t'<<Cdx(Volts)<<'\t'<<dCdV(Volts)<<'\n';

}


outV.close();




//for (int j = 0; j<Nt; j++)

//{

//        outFFT<<j<<'\t'<<t_filter[j][0]<<endl;

//}


cout<<p_o_name<<endl;
```

```
cout<<"type="<<signal_type_in<<endl;

outHdr<<"Simulation Parameters:"<<"\n\tVmax = "<<Vmax<<'\n';

outHdr<<"\tSimulation Time = "<<t<<'\n';

outHdr<<"\tSignal Type = "<<signal_type_in<<'\n';

outHdr<<"\tPulse Length = "<<pulse_len<<'\n';

outHdr<<"\tPulse Peak = "<<Vmax<<'\n';

outHdr<<"\tNumber of Nodes = "<<N<<'\n';

outHdr<<"\tdt = "<<dt<<'\n';

outHdr<<"\tep = "<<ep<<'\n';

outHdr<<"\tC/m = "<<Cm_base<<'\n';

outHdr<<"\tRs/m = "<<Rsm<<'\n';

outHdr<<"\tRp/m = "<<Rpbase_in<<'\n';

outHdr<<"\tRc/m = "<<Rcbase_in<<'\n';

outHdr<<"\tL/m = "<<Lm<<'\n';

outHdr<<"\tLine Length = "<<L<<'\n';

outHdr<<"\tFreq Factor ="<<f_factor<<'\n';

outHdr<<"\tMax Loss ="<<maxLoss<<'\n';
```

```
outHdr<<"\tNumber of Filters = "<<no_filters<<'\n';

outHdr<<"\tFilter:"<<'\n';

outHdr<<"\tDispersion Fraction = "<<dispersion_fraction<<'\n';



for (int m = 0; m<N; m++)

        outHdr<<filter[m][0]<<'\t';



outHdr<<endl;



outHdr.close();

//outMain<<"t"<<"\t"<<"Vin"<<"\t"<<"p1"<<"\t"<<"p2"<<"\t"<<"p3"<<"\t"<<"p
4"<<"\t"<<"p5"<<"\t"<<"p6"<<"\t"<<"p7"<<"\t"<<"p8"<<"\t"<<"p9"<<"\t"<<"EOL"<<"\n";



long k = 0; //counter variable for time

long n = 0; //counter variable for position

long t_frac = no_t/1000;

long print_frac = print_frac_in;
```

```
long excessive_gain = 100;



for (n=-1;n<N+1;n++)

{

        p_Y[0][n] = 0; //derivative of voltage

        p_Y[1][n] = 0; //voltage

}



for (k = 0; k < no_t; k++)

{



        p_t_arr[k] = k*dt;

        p_Vs[k] = 0;



}



if (signal_type_in == 1)  //pulse type 1 is half of a sine period
```

```
{
        for (k=0; k<floor(no_t*pulse_len); k++)
        {
                p_Vs[k] = Vmax*sin(pi/p_t_arr[pulse_end]*p_t_arr[k]);
        }
} else if (signal_type_in == 2)  //type 2 is a rising edge sigmoid
{
        for (k=0; k<no_t; k++)
        {
                p_Vs[k] = Vmax/(1+pow(2.718281828,-(p_t_arr[k]-
p_t_arr[long(floor(no_t*pulse_len))])*10/p_t_arr[long(floor(no_t*pulse_len))]));
                //                      if (k/floor(no_t*pulse_len)<1)
                //                              p_Vs[k] =
Vmax/(no_t*pulse_len)*k;
                //                      else
                //                              p_Vs[k] = Vmax;
        }
} else if (signal_type_in == 3)  //random square pulses
```

```
{
        bool pulse_flag = true;
        long k_start = 0;
        for (k = 0; k<floor(no_t*pulse_len); k++)
        {
                if (pulse_flag)
                {
                        p_Vs[k] = Vmax;
                        if (k-k_start >= (no_t*pulse_len)/1000)
                                pulse_flag = false;
                } else if ((double(rand())/double(RAND_MAX)) < .0001) {
                        pulse_flag = true;
                        k_start = k;
                }
        }

} else if (signal_type_in == 4)  //many periods of sine wave
```

```
{
        for (k=0; k<floor(no_t*pulse_len); k++)
        {
                p_Vs[k] = Vmax*sin((f_factor)*pi/p_t_arr[pulse_end]*p_t_arr[k]);
        }
} else if (signal_type_in == 5) //single gaussian with 1V bias
{
        double e = 2.718281828;
        double mu = floor(no_t*pulse_len/2.0);
        double sigma = floor(mu/5);
        double exponent = 0;
        for (k=0; k<floor(no_t*pulse_len); k++)
        {
                exponent = -((k-mu)*(k-mu)/(2*sigma*sigma));
                p_Vs[k] = Vmax*pow(e,exponent);
        }
        for (k = floor(no_t*pulse_len); k<no_t; k++)
```

```
                p_Vs[k] = 0;
} else
{
        cout<<"pulse type error"<<endl;
}

for(k = 0; k<no_t-1; k++)
{

        if (tmr == 1 && k%t_frac == 0)
                cout<<k/t_frac<<endl;

        p_Y[1][-1] = p_Vs[k];

        for (n = 0;n<N-1;n++) {

                if (p_Y[1][n]-p_Y[1][n-1] != 0 || p_Y[1][n]-p_Y[1][n+1] != 0)
```

```
                {
                        Cdx_curr = Cdx(p_Y[1][n]);
                        dCdV_curr = dCdV(p_Y[1][n]);
                        Cdx_prev = Cdx(p_Y[1][n-1]);
                        //RK4 call goes here!!!

RK4stp(n,2,p_t_arr[k],p_Y,ak0,ak1,ak2,ak3,dt,p_dydt,p_Ytemp);
                }

        }

        //=================================================================
==================

        //=================================================================
==================
```

```
	//=================================================================
==================

		//THE BELOW SECTION IS FOR DISPERSION UNCOMMENT TO
INCLUDE FREQENCY DOMAIN DISPERSION

	//=================================================================
==================

	//=================================================================
==================

	//=================================================================
==================

		for (int i = 0; i<N*C_space/2; i++)

		{

			phase_shift[i][0] =
cos(wave_vect[i]*wave_vect[i]*dispersion_fraction);
```

```
                    phase_shift[i][1] = sin(-
wave_vect[i]*wave_vect[i]*dispersion_fraction);
                }
                for (int i = N*C_space/2; i<N*C_space; i++)
                {
                    phase_shift[i][0] =
cos(wave_vect[i]*wave_vect[i]*dispersion_fraction);
                    phase_shift[i][1] =
sin(wave_vect[i]*wave_vect[i]*dispersion_fraction);
                }
                for (int i = 0; i<N; i++)
                {
                    C_electrical_dist[i] = floor(Cdx(p_Y[1][i])/C0*C_space);
                }

                c_pos_ctr=0;

                for (int i = 0; i<N; i++)
```

```
        {
                for (int j = 0; j<C_electrical_dist[i]; j++)
                {


                        signal[c_pos_ctr][0] = p_Y[1][i];
                        signal[c_pos_ctr][1] = 0;
                        c_pos_ctr++;
                }
        }


        for (int i = c_pos_ctr; i<N*C_space; i++)
        {
                signal[i][0] = signal[i][1] = 0;
        }


/*      outFFT<<"pre1:  ";
        for (int i = 0; i<N*C_space-1; i++)
```

```
{
        outFFT<<signal[i][0]<<'\t';
}
outFFT<<endl;
*/
fftw_execute(fft_V_forward);

for (int i = 0; i<N*C_space; i++)
{
//
outFFT<<i<<'\t'<<signal_fft[i][0]<<'\t'<<signal_fft[i][1]<<'\t'<<phase_shift[i][0]<<'\t'<<
phase_shift[i][1]<<'\t';
        signal_fft[i][0] = signal_fft[i][0]*phase_shift[i][0]-
signal_fft[i][1]*phase_shift[i][1];
        signal_fft[i][1] =
signal_fft[i][0]*phase_shift[i][1]+signal_fft[i][1]*phase_shift[i][0];
//      outFFT<<signal_fft[i][0]<<'\t'<<signal_fft[i][1]<<'\n';
}
```

```
//                  outFFT<<endl;



                    //&&&&&&&&&&&&&&&&&&&&&&&&

                    //Advance phase here

                    //&&&&&&&&&&&&&&&&&&&&&&&&



                    fftw_execute(fft_V_backward);



/*                  outFFT<<"post1: ";

                    for(int i = 0; i<N*C_space; i++)

                    {

                            outFFT<<signal[i][0]/10000.0<<'\t';

                    }

                    outFFT<<endl;

          */

                    c_pos_ctr = 0;
```

```
for (int i = 0; i<N; i++)

{

        p_Y[1][i] = signal[c_pos_ctr][0]/(N*C_space);  //These will need
to be modified to account for changes in C

        c_pos_ctr = c_pos_ctr+C_electrical_dist[i];



}



//==================================Top of
block============================

c_pos_ctr=0;



for (int i = 0; i<N; i++)

{

        for (int j = 0; j<C_electrical_dist[i]; j++)
```

```
                {


                        signal[c_pos_ctr][0] = p_Y[0][i];  //These will need to be
modified to account for changes in C
                        signal[c_pos_ctr][1] = 0;
                        c_pos_ctr++;
                }
        }



        for (int i = c_pos_ctr; i<N*C_space; i++)
        {
                signal[i][0] = signal[i][1] = 0;
        }


/*      outFFT<<"pre1:  ";
        for (int i = 0; i<N*C_space-1; i++)
        {
```

```
                outFFT<<signal[i][0]<<'\t';

            }

            outFFT<<endl;

            */

            fftw_execute(fft_V_forward);



            for (int i = 0; i<N*C_space; i++)

            {

    //

    outFFT<<i<<'\t'<<signal_fft[i][0]<<'\t'<<signal_fft[i][1]<<'\t'<<phase_shift[i][0]<<'\t'<<
phase_shift[i][1]<<'\t';

                signal_fft[i][0] = signal_fft[i][0]*phase_shift[i][0]-
signal_fft[i][1]*phase_shift[i][1];

                signal_fft[i][1] =
signal_fft[i][0]*phase_shift[i][1]+signal_fft[i][1]*phase_shift[i][0];

    //              outFFT<<signal_fft[i][0]<<'\t'<<signal_fft[i][1]<<'\n';

            }

    //          outFFT<<endl;
```

```
                //&&&&&&&&&&&&&&&&&&&&&&&&
                //Advance phase here
                //&&&&&&&&&&&&&&&&&&&&&&&&


                fftw_execute(fft_V_backward);
/*
                outFFT<<"post1: ";
                for(int i = 0; i<N*C_space; i++)
                {
                        outFFT<<signal[i][0]/10000.0<<'\t';
                }
                outFFT<<endl;
        */
                c_pos_ctr = 0;
```

```
                for (int i = 0; i<N; i++)

                {

                        p_Y[0][i] = signal[c_pos_ctr][0]/(N*C_space);  //These will need
to be modified to account for changes in C

                        c_pos_ctr = c_pos_ctr+C_electrical_dist[i];



                }

        //=============================================================
==================

        //=============================================================
==================

        //=============================================================
==================

                //THE ABOVE SECTION IS FOR DISPERSION UNCOMMENT TO
INCLUDE FREQENCY DOMAIN DISPERSION
```

```
        //=================================================================
==================

        //=================================================================
==================

        //=================================================================
==================

        //=================================================================
==================

        //=================================================================
==================

        //=================================================================
==================

                //THE BELOW SECTION IS FOR FILTERING UNCOMMENT TO
INCLUDE FREQENCY DOMAIN FILTERING
```

```
	//=================================================================
==================

	//=================================================================
==================

	//=================================================================
==================

	/*		if (filter_flag && k%filter_frac==0) {

			for (int i = 0; i<N; i++)

			{

				//outFFT<<1<<'\t'<<i<<'\t'<<p_Y[1][i]<<'\t';

				for (int j = Nt-2; j>=0; j--)

				{

					p_y_buff[i][j+1]=p_y_buff[i][j];

				}



				p_y_buff[i][0] = p_Y[1][i];
```

```
for (int j = 0; j<Nt; j++)

{

        //outFFT<<p_y_buff[i][j]<<'\t';

        t_signal[j][0]=p_y_buff[i][j];

        t_signal[j][1]=0;

}

//outFFT<<endl;



//outFFT<<t_signal[0][0]<<'\t';



fftw_execute(fft_t_forward);



//outFFT<<1<<'\t';

for (int j = 0; j<Nt; j++)

{

        t_fft2[j][0] = t_fft[j][0]*t_filter[j][0];
```

```
            t_fft2[j][1] = t_fft[j][1]*t_filter[j][1];

            //outFFT<<t_fft2[j][0]+t_fft2[j][1]<<'\t';

        }

        //outFFT<<endl;

        fftw_execute(fft_t_backward);



        //outFFT<<2<<'\t'<<i<<'\t'<<p_Y[1][i]<<'\t';



        //outFFT<<2<<'\t';

        //Remove this loop and apply to only one time to get
maximum speed

        for (int j = 0; j<Nt; j++) {

            t_signal2[j][0]=t_signal2[j][0]/double(Nt);

            //outFFT<<t_signal2[j][0]<<'\t';

        }



        //outFFT<<endl;
```

```
//outFFT<<p_Y[1][i]<<'\t'<<p_y_buff[i][0]<<'\t'<<t_signal[0][0]<<endl;

                                        p_Y[1][i] = t_signal2[0][0];




                                }

                        }*/




        //=============================================================

==================




        //=============================================================

==================




        //=============================================================

==================

                        //THE ABOVE SECTION IS FOR FILTERING UNCOMMENT TO

INCLUDE FREQENCY DOMAIN FILTERING
```

```
        //=================================================================
==================

        //=================================================================
==================

        //=================================================================
==================

                p_Y[1][N-1] = p_Y[1][N-2];  //the voltage at the last node is better
approximated by the voltage at the second to last node than by ground

                //for (int i = 0; i<N; i++)
                //      p_Y[1][i]=p_Y[1][i]-p_Y[1][N-1];  //Remove error introduced by
discarding rounding error in imaginary part of FT (NOTE: This will screw up any results after
pulse gets to the end of the line)
```

```
                if (k%print_frac == 0){

        outMain<<p_t_arr[k]<<"\t"<<p_Vs[k]<<"\t"<<p_Y[1][loc10]<<"\t"<<p_Y[1][loc20]<<"
\t"<<p_Y[1][loc30]<<"\t"<<p_Y[1][loc40]<<"\t"<<p_Y[1][loc50]<<"\t"<<p_Y[1][loc60]<<"\t"
<<p_Y[1][loc70]<<"\t"<<p_Y[1][loc80]<<"\t"<<p_Y[1][loc90]<<"\t"<<p_Y[1][N-4]<<"\n";

                        /*if
(p_Y[1][loc10]>excessive_gain*p_Vs[k]||p_Y[1][loc20]>excessive_gain*p_Vs[k]||p_Y[1][loc30
]>excessive_gain*p_Vs[k]||p_Y[1][loc40]>excessive_gain*p_Vs[k]||p_Y[1][loc50]>excessive_g
ain*p_Vs[k]||p_Y[1][loc60]>excessive_gain*p_Vs[k]||p_Y[1][loc70]>excessive_gain*p_Vs[k]||
p_Y[1][loc80]>excessive_gain*p_Vs[k]||p_Y[1][loc90]>excessive_gain*p_Vs[k]||p_Y[1][N-
4]>excessive_gain*p_Vs[k]) {

                        outMain<<"Excessive Gain"<<endl;

                        exit(0);

                        }*/

                }


        }


        delete (p_Y[0]-1);
```

```
delete (p_Y[1]-1);

delete p_Y;



delete (p_Ytemp[0]-1);

delete (p_Ytemp[1]-1);

delete p_Ytemp;



fftw_destroy_plan(fft_V_forward);

fftw_destroy_plan(fft_V_backward);

fftw_free(filter);

fftw_free(signal);

fftw_free(signal_fft);



fftw_destroy_plan(fft_t_forward);

fftw_destroy_plan(fft_t_backward);

fftw_free(t_filter);

fftw_free(t_signal);
```

```
fftw_free(t_fft);

fftw_free(t_signal2);

fftw_free(t_fft2);



delete ak0;

delete ak1;

delete ak2;

delete ak3;



delete p_t_arr;



delete p_dydt;



delete p_Vs;



delete C_electrical_dist;

delete wave_vect;
```

```
            outMain.close();


            return;
        }



        void feval(int n, double t, double** y, double* dydt)
        {
            /*
            //Differential equations following derivation using model consisting of
inductance, series resistance, shunt resistance, and capacitance with a spreading resistor
            double term01 = (y[1][n-1]-2*y[1][n]+y[1][n+1])/(Ldx*Cdx_curr);
            double term02 = Rsdx*y[1][n]/(Rpdx*(Ldx*Cdx_curr));
            double term03 = dCdV_curr*y[0][n]*y[0][n]/Cdx_curr;
            double term04 = Rsdx*y[0][n]/Ldx;
            double term05 = y[0][n]/(Cdx_curr*Rpdx);
            dydt[0] = term01-term02-term03-term04-term05;
```

```
dydt[1] = y[0][n];



return;*/



//Differential equations following derivation using model consisting of inductance, series resistance, shunt resistance, and capacitance with a spreading resistor

double term001 = 1/(Ldx*Cdx_curr*(1+Rcdx/Rpdx));

double term002 = y[1][n-1]-2*y[1][n]+y[1][n+1];

double term003 = Ldx*((Rcdx/Rpdx-1)*dCdV_curr*y[0][n]*y[0][n]-y[0][n]/Rpdx);

double term004 = Rsdx/Rpdx*y[1][n]+Rsdx*Rcdx/Rpdx*Cdx_curr*y[0][n]+Rcdx*Cdx_curr*y[0][n];

dydt[0] = term001*(term002+term003+term004);

dydt[1] = y[0][n];



return;

/*
```

```
//Differential equations following

//Tsuboi and Toyama "Computer experiments on solitons in a nonlinear transmission line I. Formation of stable soliton" Physical Review A, vol. 44, pg 2686, 15 August 1991

double tst01 = 1/Ldx;

double tst02 = y[1][n-1]-2*y[1][n]+y[1][n+1];

double tst03 = Ldx*dCdV_curr*(y[0][n]*y[0][n]);

double tst04 = (Rpdx)*(Cdx_prev*y[0][n-1]-2*Cdx_curr*y[0][n]*Cdx_curr*y[0][n+1]);

double tst05 = Rsdx*Cdx_curr*y[0][n];

dydt[0] = (1/Ldx)*(y[1][n-1]-2*y[1][n]+y[1][n+1]-Ldx*dCdV_curr*(y[0][n]*y[0][n])+(Rpdx)*(Cdx_prev*y[0][n-1]-2*Cdx_curr*y[0][n]*Cdx_curr*y[0][n+1])-Rsdx*Cdx_curr*y[0][n]);

dydt[1] = y[0][n];


return;


//Differential equations following
```

```
//R H Freeman and A E Karbowiak "An Investigation of Nonlinear Transmission Lines and Shock Waves" J. Phys. D: Appl. Phys., Vol 10, 1977 pg53

//and

//F A Benson, J D Last and V I Zharikov "An Analysis of Lumped-Parameter Nonlinear Transmission Lines" IEEE International Convention Record 14 (7) 327-339



//equations including resistance (no conductance)

dydt[0] = (y[1][n-1]-2*y[1][n]+y[1][n+1])/(Ldx*Cdx_curr)-dCdV_curr*((y[0][n]*y[0][n])/Cdx_curr)-(Rsdx/Ldx)*y[0][n]-(1/(Rpdx*Cdx_curr))*y[0][n]-(Rsdx/(Rpdx*Ldx*Cdx_curr))*y[1][n];

dydt[1] = y[0][n];



//original equations

dydt[0] = (y[1][n-1]-2*y[1][n]+y[1][n+1])/(Ldx*Cdx(y[1][n]));//-dCdV_curr*((y[0][n]*y[0][n])/Cdx_curr);

dydt[1] = y[0][n];



return;

*/
```

```
}

void RK4stp(int n, int N, double t, double** yode, double* ak0, double* ak1, double*
ak2, double* ak3, double h, double* dydt, double** ytemp)

{

int j = 0;

if (yode[1][n-1] == 0 && yode[1][n] == 0 && yode[1][n+1] == 0 && yode[0][n]
== 0) {

yode[1][n] = 0;

} else {

feval(n,t,yode,dydt);

for (j = 0; j<N; j++)

{

ak0[j] = h*dydt[j];

ytemp[j][n] = yode[j][n]+0.5*ak0[j];
```

```
        ytemp[j][n-1] = yode[j][n-1];

        ytemp[j][n+1] = yode[j][n+1];

}


feval(n, t+0.5*h, ytemp, dydt);


for (j = 0; j<N; j++)

{

        ak1[j]=h*dydt[j];

        ytemp[j][n] = yode[j][n]+0.5*ak1[j];

        ytemp[j][n-1] = yode[j][n-1];

        ytemp[j][n+1] = yode[j][n+1];

}


feval(n,t+0.5*h,ytemp,dydt);


for (j = 0; j<N; j++)
```

```
        {
            ak2[j] = h*dydt[j];
            ytemp[j][n] = yode[j][n]+ak2[j];
            ytemp[j][n-1] = yode[j][n-1];
            ytemp[j][n+1] = yode[j][n+1];
        }

        feval(n,t+h,ytemp,dydt);

        for (j = 0; j<N; j++)
        {
            ak3[j] = h*dydt[j];
            yode[j][n] = yode[j][n]+(ak0[j]+2*ak1[j]+2*ak2[j]+ak3[j])/6;
        }

}
```

```
        return;
}

double Cdx(double V)
{

        return C_base;  //use for constant value when testing

        double sigma = 0.44019;
        double x0 = 1.1651;
        double factor = 3.2055;

        /*      //The below declarations and the return statement are for a discrete line and should be removed for general testing.
        double a1=.2558;
        double a2=.06541;
        double a3=.01172;
        double a4=.0008678;
```

```
		double C_V0=244e-12;

		double V0 = 1;



		return C_V0*(1-a1*(V-V0)+a2*(V-V0)*(V-V0)-a3*(V-V0)*(V-V0)*(V-
V0)+a4*(V-V0)*(V-V0)*(V-V0)*(V-V0));

		*/

		if (V<0)

			return C_base;//(1/(sigma*sqrt(2*3.1415926))+x0)*C_base;



		//return C_base*(1-C_nl*V);



		double tmp =
(1/(sigma*2.5066282532517660904495944488382)*pow(2.718281828,-
V*V/(2*sigma*sigma))+x0)*C_base/(1/(sigma*2.5066282532517660904495944488382)*pow(
2.718281828,-0/(2*sigma*sigma))+x0);

		return tmp;



	}
```

```
double dCdV(double V)

{


        //return 0;  //use for constant value when testing


        double val1;

        double val2;

        double dV = 1e-10;


        val1 = Cdx(V);

        val2 = Cdx(V+dV);


        return (val2-val1)/dV;//*/


}
```